Dynamics and Drivers of Multi-Scale Storm-Time Ionospheric Density Structures

by

Zihan Wang

A dissertation submitted in partial fulfillment
of the requirements for the degree of
Doctor of Philosophy
(Climate and Space Sciences and Engineering)
in The University of Michigan
2021

Doctoral Committee:

Associate Professor Shasha Zou, Chair
Professor Kenneth Powell
Professor Tuija Pulkkinen
Professor Aaron Ridley

Zihan Wang

wzihan@umich.edu

ORCID ID: 0000-0001-6601-2520

For my father Ke Wang, my mother Min Han, and my wife Zixian Wang, who always stand behind me with unconditional support

ACKNOWLEDGEMENTS

I would like to thank Professor Shasha Zou, my advisor, for her continuing support, guidance, and encouragement over the last five years. Many thanks to people in our department Jiaen Ren, Thomas Coppeans, Lei Liu, Ercha Aa, Han Jin, Doga Ozturk and Zhenguang Huang, for their discussion and collaboration. Especially, I would like to thank Jiaen for helping plot wonderful GPS TEC plots and many other helpful and useful discussions, and also Doga and Zhenguang for introducing me how to use SWMF. Thanks to Professor Tuija Pulkkinen, Professor Aaron Ridley, and Professor Kenneth Powell for their service on my committee.

Many thanks to Simon Shepherd, Mike Ruohoniemi and Bharat Kunduri for providing and processing the SuperDARN radar data used in Chapter 3 of this dissertation, Jun Liang for their help with the ASI data that used in Chapter 3 and Jesper Gjerloev for his help with the SuperMAG data used in Chapter 3. In addition, I would like to thank all of my co-authors for their collaboration.

TABLE OF CONTENTS

LIST OF FIGURES

Figure

LIST OF ABBREVIATIONS

2LCW two-loop current wedge

AMPERE Active Magnetosphere and Planetary Electrodynamics Response Experiment

ASI All Sky Imager

BCBF Birkeland Current Boundary Flows

BATSRUS Block-Adaptive-Tree-Solar Wind-Roe-Upwind-Scheme

CIRs Corotational Interaction Regions

CMEs Coronal Mass Ejections

Dst Disturbance storm time

ECT Energetic Particle, Composition and Thermal Plasma Suite

EDP electron density profile

EFW Electric Field and Waves Instrument

EIA Equatorial ionization anomaly

EMFISIS Electric and Magnetic Field Instrument Suite and Integrated Science

FACs field-aligned currents

FISM Flare Irradiance Spectral Model

FOV field of view

FTE Flux Transfer Event

GITM Global Ionosphere Thermosphere Model

GOES Geostationary Operational Environmental Satellite

GNSS Global Navigation Satellite System

GPS Global Positioning System

GSM Geocentric Solar Magnetospheric

GUVI Global Ultraviolet Imager

HOPE Helium Oxygen Proton Electron

ICMEs Interplanetary Coronal Mass Ejections

IMF Interplanetary Magnetic Field

IRI International Reference Ionosphere

ISR Incoherent Scattering Radar

LOS line-of-sight

LS-SAPS large-scale SAPS

MagEIS Magnetic Electron Ion Spectrometer

MHD magnetohydrodynamics

MIT Mangetosphere Ionosphere Thermosphere

MS-SAPS+ meso-scale enhancement of SAPS

OCB open-closed field line boundary

RCM Rice Convection model

REPT Relativistic Electron Proton Telescope

SAPS Sub-Auroral Polarization Streams

SCW substorm current wedge

SEDs Storm-Enhanced Densities

SEM Space Environment Monitor

SSC Sudden Storm Commencement

SuperDARN Super Dual Auroral Radar Network

SWMF Space Weather Modeling Framework

SYM-H symmetric disturbances for H component

TEC Total Electron Content

TID Traveling Ionospheric Disturbance

TIMED Thermosphere Ionosphere Mesosphere Energetics and Dynamics

TOI Tongue of Ionization

VAP Van Allen Probes

VTEC Vertical Total Electron Content

ABSTRACT

Large disturbances in the solar wind, such as Coronal Mass Ejections (CMEs), can trigger the most significant geomagnetic activities near the Earth, i.e., storms. In the ionosphere, various electron density structures can form during storms, which are usually accompanied by abrupt electron density gradients that can significantly impact the propagation of radio signals going through or reflected by the ionosphere. The spatial scales of these storm-time electron density structures span from thousands of km to several km or less.

Formation and dynamic evolution of these ionospheric density structures are manifests of the complex Mangetosphere Ionosphere Thermosphere (MIT) coupling processes during storms. Using a combination of multi-instrument observations and numerical simulations, we performed a comprehensive study investigating various aspects of these dynamics and their drivers. The findings of this study contribute to our systematic understanding of the storm-time MIT coupling processes and could assist future missions targeting these density structures.

In this research, we studied the formation processes of two density structures that often occur at mid and high latitudes during storms: Storm-Enhanced Densities (SEDs) and polar cap patches. SEDs are electron density enhancements at mid-latitudes and are often suggested as the main plasma sources for the patches in the polar cap region when they extend to high latitudes. Several mechanisms have been proposed in the past to explain the segmentation of SEDs into patches. Using state-of-the-art simulation tools, we proposed a new segmentation mechanism associated with boundary flows between the Region-1 and Region-2 field-aligned cur-

rents (FACs) when the partial ring current drifts towards the dayside. No sudden external interplanetary magnetic field variations or transient reconnection are required in this mechanism.

Besides the boundary flows, other fast convection flow structures and their temporal variations, such as Sub-Auroral Polarization Streams (SAPS), have also been suggested to be important for ionosphere density structuring processes. Using a comprehensive ground- and space-based instrument suite, we performed a detailed analysis of the formation and temporal evolution of SAPS during a moderate storm. We found that the SAPS electric field formed before a substorm onset, and was accompanied by a local magnetic field dip and a dispersionless ion injection from the flank side. In the conjugate ionosphere, the SAPS developed near the equatorward boundary of the Harang reversal. The observed complex signatures in the coupled magnetosphere and ionosphere can be explained by a two-loop current wedge generated by the enhanced plasma pressure gradient and the diamagnetic effect of the structured ring current following the particle injection.

One recently discovered aspect of the storm-time ionospheric responses is the hemispheric asymmetry. We performed a detailed case study of the drivers of the hemispheric asymmetry in electron density observed during the storm recovery phase. The asymmetries were observed simultaneously in the dawn and afternoon sectors and had opposite polarities. They were suggested to be driven by a combination of the hemispheric asymmetries in the thermospheric composition, vertical drifts, and Traveling Ionospheric Disturbance (TID) activity.

CHAPTER I

Introduction

1.1 Dungey Convection Cycle

The global scale magnetospheric and ionospheric convection is mainly driven by magnetic reconnection. *Dungey* (1961) proposed the theoretical framework of the plasma circulation in the magnetosphere during southward Interplanetary Magnetic Field (IMF), driving by both dayside and nightside reconnections. Magnetic reconnection can be facilitated when magnetic fields with opposite polarities are transported toward each other. At the point where they meet, the field lines reconnect and form two new field lines, which are then expelled perpendicularly away from the reconnection site. In this process, the magnetic energy is converted into the plasma kinetic energy and heating.

1.1.1 Magnetospheric Convection

As shown in Fig 1.1, when the IMF is southward (1'), which is opposite to the dayside geomagnetic field line (1), reconnection occurs on the dayside magnetopause. The newly-generated open field lines have one end connected to the Earth and the other connected to the solar wind (2 and 2'). Then, the solar wind pulls the open field lines anti-sunward (4 and 4') to the nightside. At the magnetotail, the two open field lines (6 and 6') reconnect again and generate two new field lines: one closed field

line (7) and one IMF line (7'). The IMF line is ejected anti-sunward, and the newly closed field line is transported towards the Earth and eventually back to dayside (9) (*Kivelson et al.*, 1995).

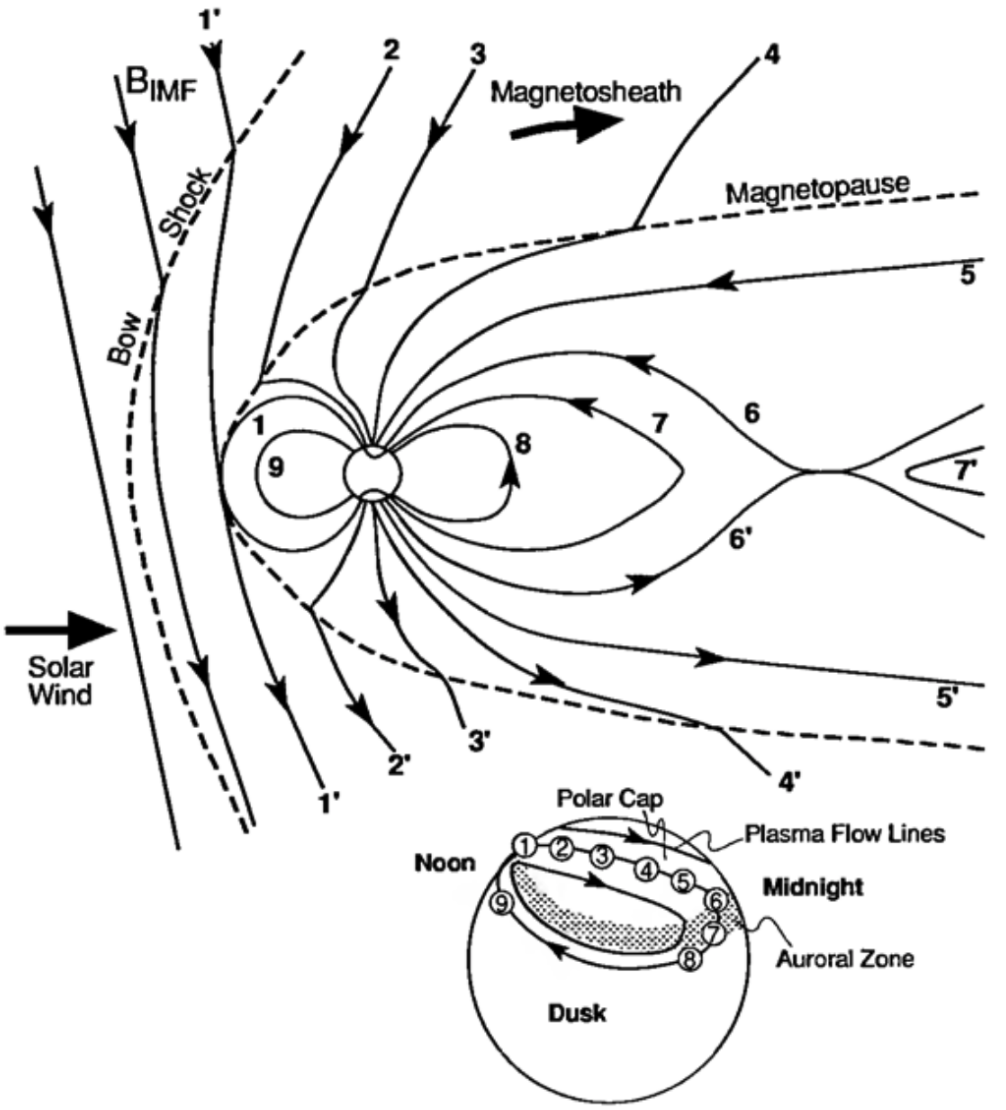

Figure 1.1: Dungey cycle: Flow of plasma within the magnetosphere. The number represents the succession of field lines. From *Kivelson et al.* (1995) Fig 9.11.

1.1.2 High-Latitude Convection Pattern

In the reference frame of the solar wind, due to the infinite conductivity, the electric field is zero. In the inertia reference frame, according to the Lorentz transform, there is an electric field $\mathbf{E} = -\mathbf{V_{plasma}} \times \mathbf{B}$, where V is the solar wind plasma velocity and B is the vector interplanetary magnetic field. When the IMF is southward, there will be a dawn-to-dusk electric field in the solar wind and magnetosphere (*Baumjohann and Treumann*, 1997).

When the magnetic field line in Fig 1.1 completes the Dungey cycle in the magnetosphere, its footprint also finishes a closed trajectory in the ionosphere. When the field line moves anti-sunward with the solar wind, its footprint moves anti-sunward in the polar cap ionosphere. Due to the infinite field-aligned conductivity, there is no potential drop along the field line, i.e., the magnetic field line is equipotential. Thus, the dawn-dusk electric field maps to the polar cap region. When the field line travels back to the dayside at lower latitudes, its footprint moves back to the dayside as well. On the dusk side, the electric field is poleward in the return flow region, while on the dawn side, it switches to equatorward. In the framework of the Dungey cycle, a two-cell convection pattern forms in the high latitude ionosphere, as shown in Fig 1.2, when the magnetic field line completes the full cycle in the magnetosphere.

The direction of flows near the cusp region is sensitive to the direction of the IMF. *Ruohoniemi and Greenwald* (1998) showed that the convection flow switched suddenly (2 min) from sunward to antisunward with the velocity magnitude change reaching as large as 1500 m/s in about 6 minutes, responding to a sudden IMF southward turning. In addition to the IMF B_z, the IMF B_y is also important for the convection flows at high-latitudes (*Cowley et al.*, 1991). As shown in Figure 1.3, when the IMF $B_z < 0$ and $B_y > 0$, in the northern hemisphere, the dayside cusp should be displaced towards the post afternoon sector, and the convection flows near the cusp move toward the dawn side. When the IMF $B_z < 0$ and $B_y < 0$, in the

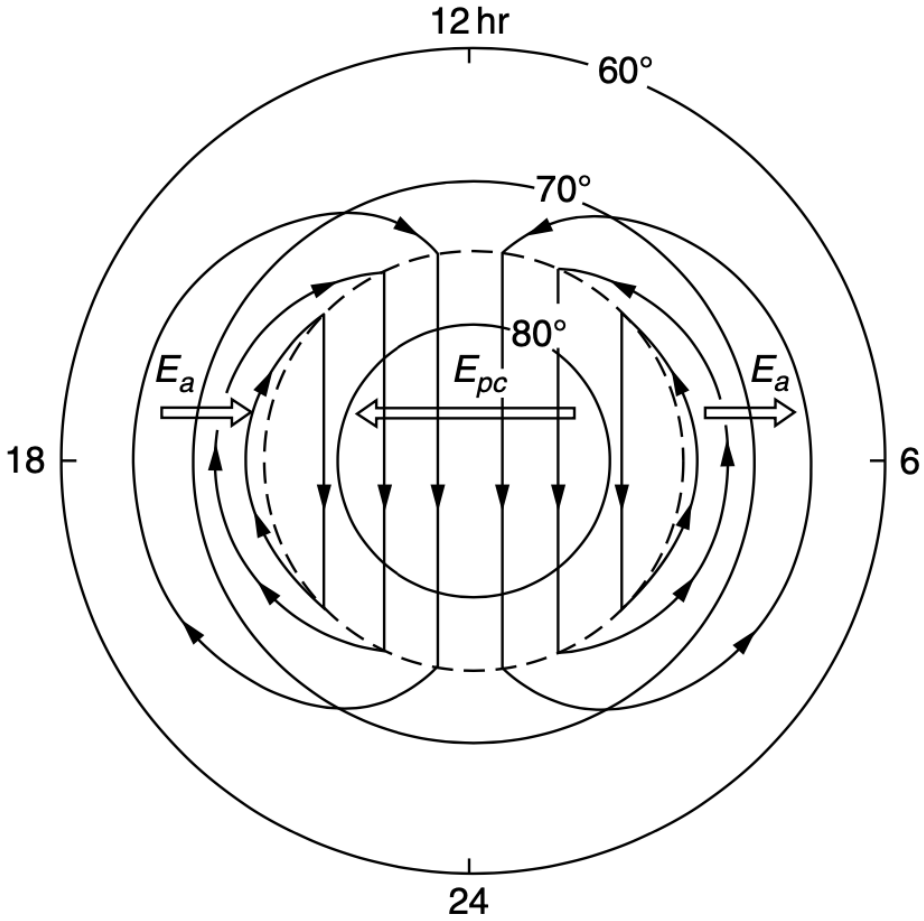

Figure 1.2: Representation of ionospheric electric fields in the northern hemisphere polar cap and auroral zone, as well as the plasma flow due to those fields. From *Kelley* (2009) Fig 8.3a.

northern hemisphere, the dayside cusp should be displaced toward the dawn side, and the convection flows near the cusp move toward the dusk side. In the southern hemisphere, the responses are in the opposite sense.

Weimer (2005) provided an empirical model of the high-latitude electric potentials as a function of the solar wind parameters. Figure 1.4 describes the dependence of the high-latitude potentials on the IMF clock angle. When IMF $B_z < 0$ and $B_y > 0$, in the northern hemisphere, the dusk cell is larger. When IMF $B_z < 0$ and $B_y < 0$, in the northern hemisphere, the dawn cell is larger. In the southern hemisphere, the

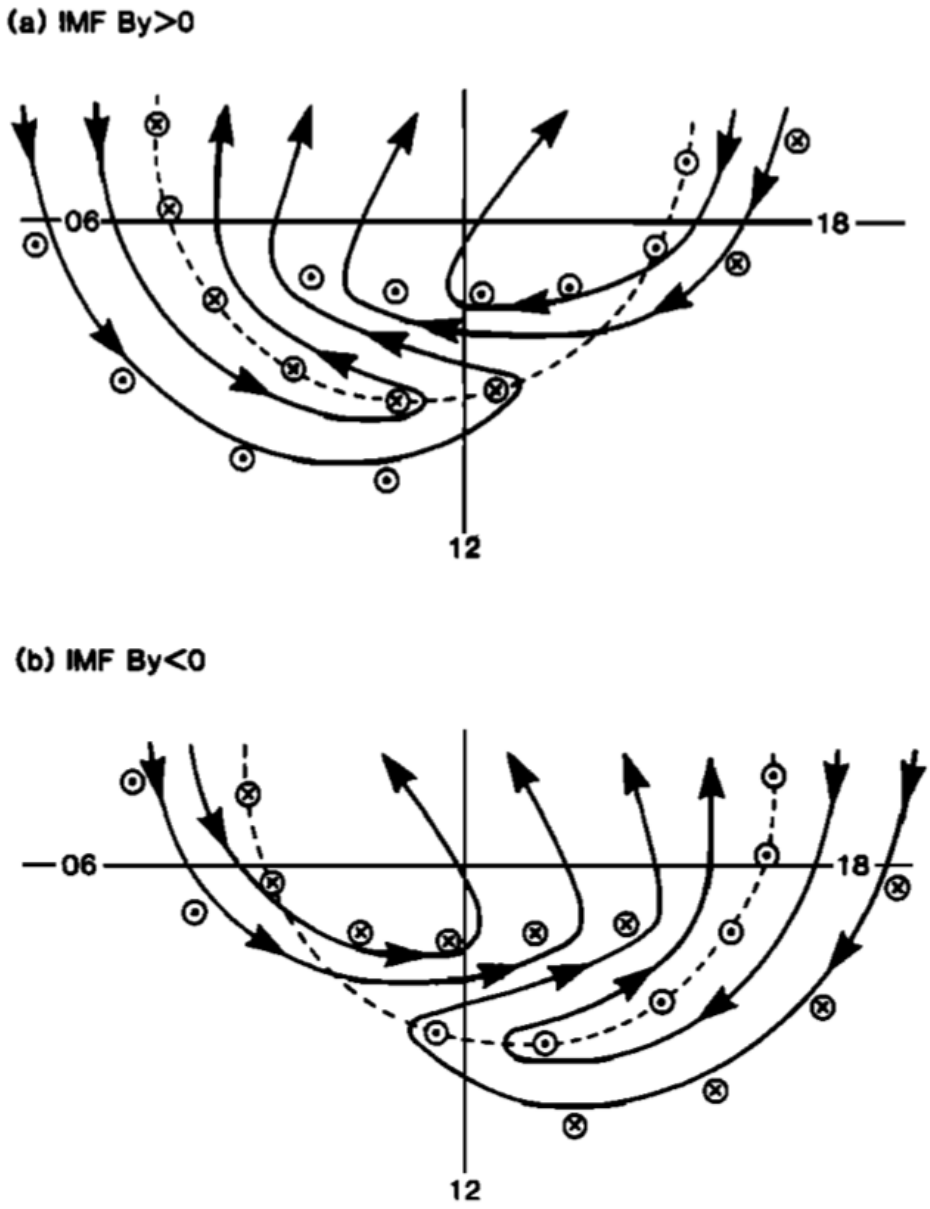

Figure 1.3: Sketch showing IMF By-dependent effect on the streamlines (solid curves) and on the open-close field line boundary(dashed curve) in the northern hemisphere. From *Cowley et al.* (1991) Fig 3.

responses are in the opposite sense.

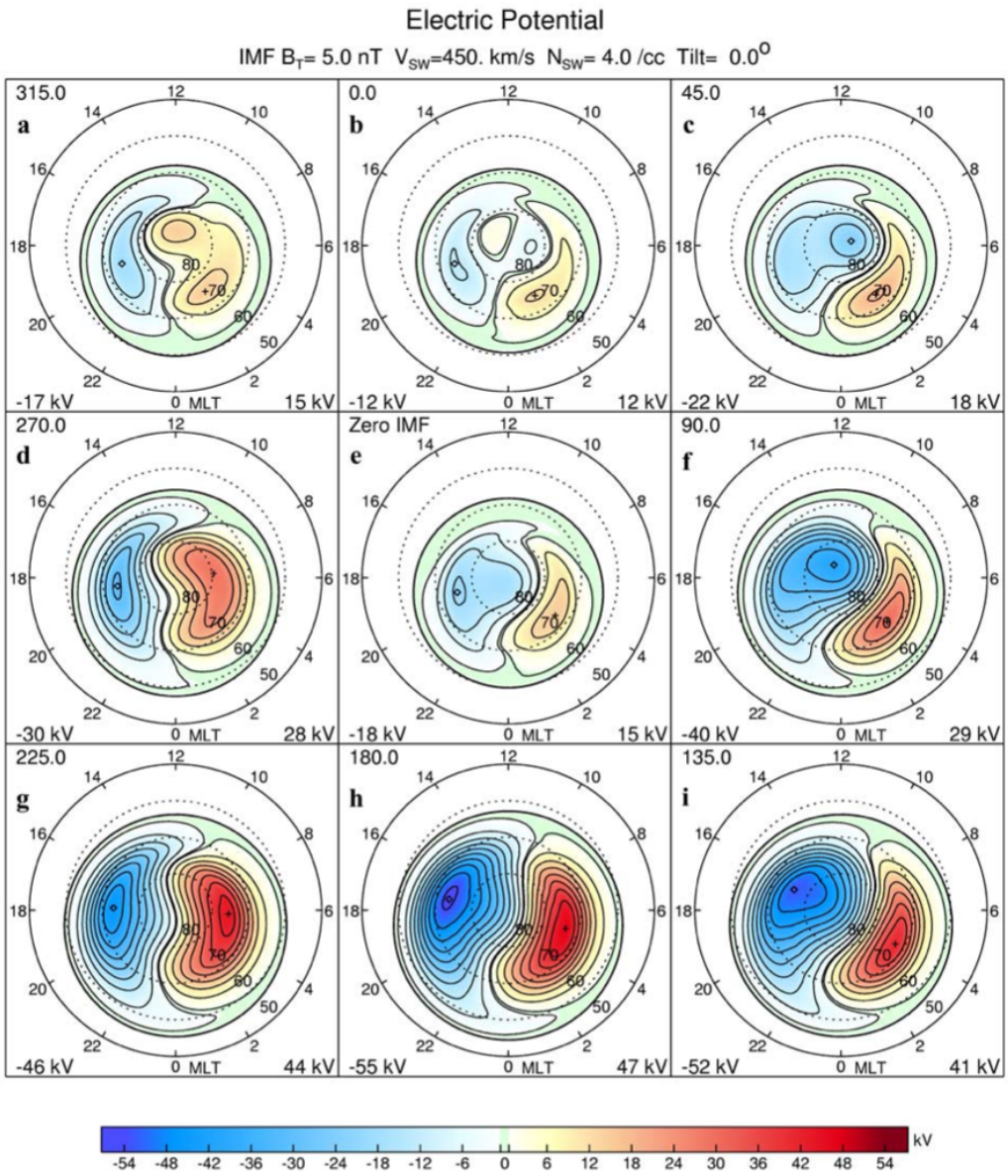

Figure 1.4: (a–i) Polar cap electric potentials in the Northern Hemisphere, mapped as a function of AACGM latitude and MLT. Figures a–d and f–i show the patterns for eight different clock angle orientations of the IMF vector in the GSM Y-Z plane; the angle in degrees is indicated in the top left corner of each map. The IMF has a fixed magnitude of 5 nT, the solar wind velocity is 450 km/s, the solar wind number density is 4 cm^{-3}, and the dipole tilt angle is 0°. Figure e shows the potential for zero IMF, with the same solar wind conditions. Minimum and maximum potential values are printed in the bottom left and right corners of each map, with locations indicated by the diamonds and pluses. From *Weimer* (2005) Fig 2.

1.2 Geomagnetic Storms

Geomagnetic storms are periods when the near-Earth space environment is strongly disturbed by the solar wind and IMF. During this period, a sufficiently intense interplanetary convection electric field leads, through a substantial energization in the magnetosphere-ionosphere system, to an intensified ring current (*Gonzalez et al.*, 1994). The ring current causes the horizontal geomagnetic field on the Earth's surface to decrease. The Disturbance storm time (Dst) index, defined by the hourly average of the global horizontal field variation from four low-latitude ground magnetometer stations, is used to infer the strength of the ring current and describe the amplitude of the storm (e.g. *Russell et al.*, 1974). The symmetric disturbances for H component (SYM-H) index is a high-temporal-resolution (1 min) alternative of the Dst (e.g. *Wanliss and Showalter*, 2006). The magnitude of a geomagnetic storm can be classified based on the minimum of Dst or SYM-H value: moderate (-100 nT $<$ Dst $<$ -50 nT), intense (-250 nT $<$ Dst $<$ -100 nT), or super (-250 nT $<$ Dst) (*Gonzalez et al.*, 1994; *Echer et al.*, 2008). Geomagnetic storms are mainly driven by large-scale interplanetary transients (hours to days), including the Coronal Mass Ejections (CMEs) or Corotational Interaction Regions (CIRs), and particularly by the southward IMF contained in those transients (*Gonzalez et al.*, 1994).

As shown in Fig 1.5, geomagnetic storms mainly consist of two phases: the main phase and the recovery phase (*Baumjohann and Treumann*, 1997). When a large amount of the solar wind energy enters the magnetosphere, the ring current strengthens, and the Dst/SYM-H decreases, which is defined as the main phase (*Baumjohann and Treumann*, 1997). The main phase usually lasts for a few hours (*Yokoyama and Kamide*, 1997). When the solar wind energy stops entering the magnetosphere, the ring current gradually decays, and the Dst/SYM-H recovers back to the quiet-time value, which is defined as the recovery phase (*Baumjohann and Treumann*, 1997). The recovery phase typically lasts for one to two days (*Yokoyama and Kamide*, 1997). If

a shock is accompanied with the interplanetary transients, the storm can begin with a sudden increase in the horizontal component and is referred to as Sudden Storm Commencement (SSC). The shock compresses the dayside magnetopause and pushes the Chapman–Ferraro current closer to the Earth, which then leads to the sudden increase of the Dst/SYM-H (*Joselyn and Tsurutani*, 1990).

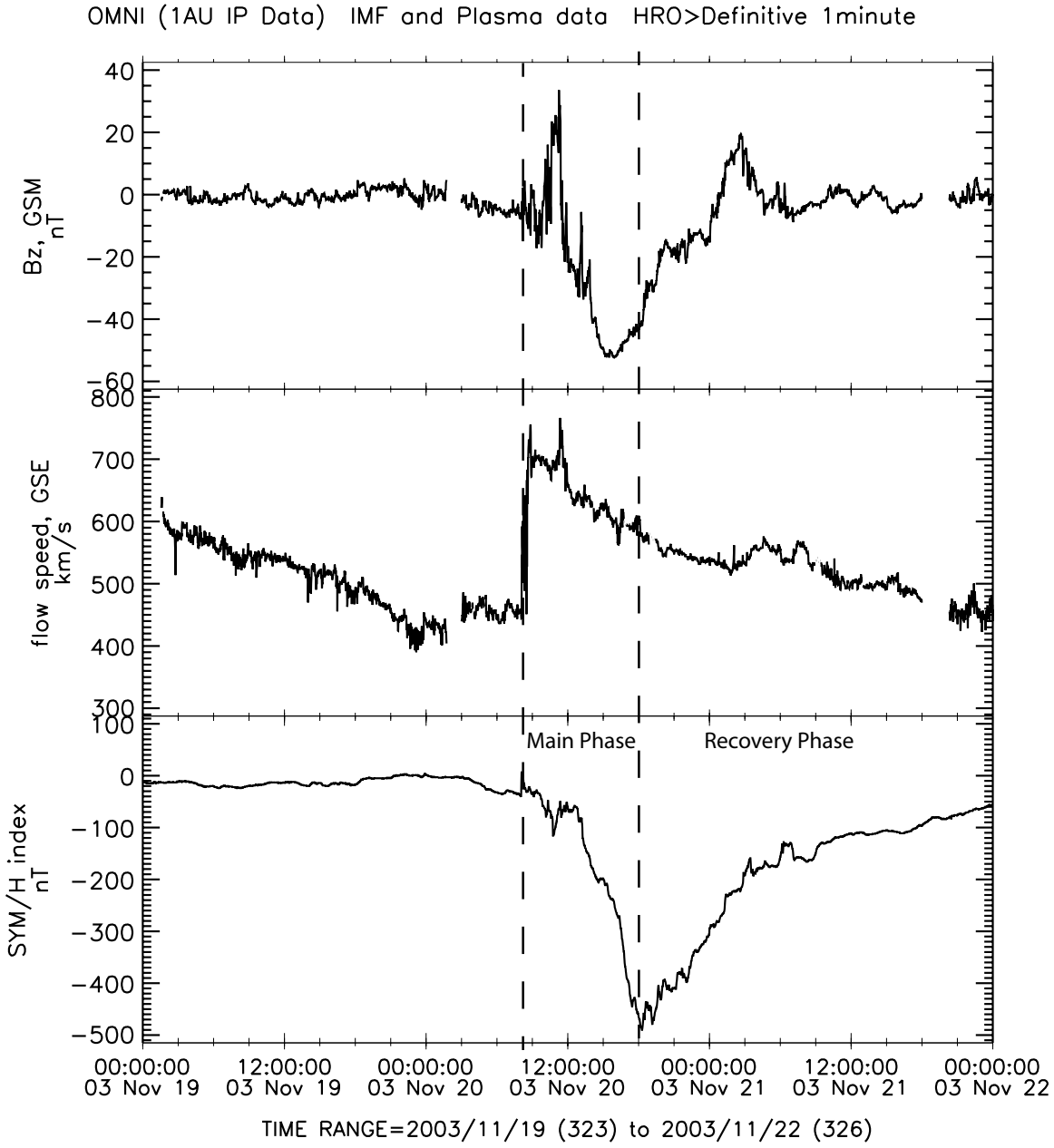

Figure 1.5: IMF B_z in GSM coordinate, solar wind flow velocity and SYM-H index during the 2003 Halloween Storm.

1.3 Ring Current and Partial Ring Current

During storm times, the ring current is the main contributor to the magnetic field depression on the Earth's surface. During active times, energetic particles (10-200 keV) follow energy-dependent drifts, i.e., gradient and curvature drifts in the inner magnetosphere. Ions drift westward and electrons drift eastward around the Earth. Thus, a westward current develops near the equatorial plane and is referred to as the ring current (*Baumjohann and Treumann*, 1997). From the Biot-Savart's law, the westward ring current can generate a magnetic disturbance opposite to the rotation axis of the Earth. The magnitude of the magnetic perturbation is often characterized by the Dst/SYM-H index and is proportional to the total kinetic energy of the drifting particles.

When the IMF turns southward, the Dungey cycle is triggered. More particles are transported into the inner magnetosphere through large-scale convection and meso-scale injections, and thus can enhance the ring current. The buildup of the ring current is the major magnetospheric manifestation of the magnetic storm. Particles enter the inner magnetosphere from the nightside and form a pressure peak on the nightside, driving an asymmetric ring current. This asymmetric ring current is referred to as the partial ring current. The azimuthal pressure gradient within the partial ring current is important for the generation of the Region-2 field-aligned currents (FACs).

Fig 1.6 shows the drift paths of cold magnetospheric particles, hot ions, and electrons. The boundary separating the open and closed paths of energetic particles are called the Alfvén layer. Inside the Alfvén layer, particles have closed drift paths. Outside the Alfvén layer, they are on open drift paths and can reach and get lost through the magnetopause. The location of the Alfven layer is determined by the dawn-to-dusk electric fields and the energies of the particles. During storm time, the dawn-to-dusk electric fields in the equatorial magnetosphere increase, and the Alfven

layer shrinks. Particles previously on closed drift paths now can be on open drift paths and get lost through the magnetopause, which can weaken the ring current on the dayside. In addition, wave-particle interactions can also modulate the particle fluxes on the dayside and nightside plasma sheet.

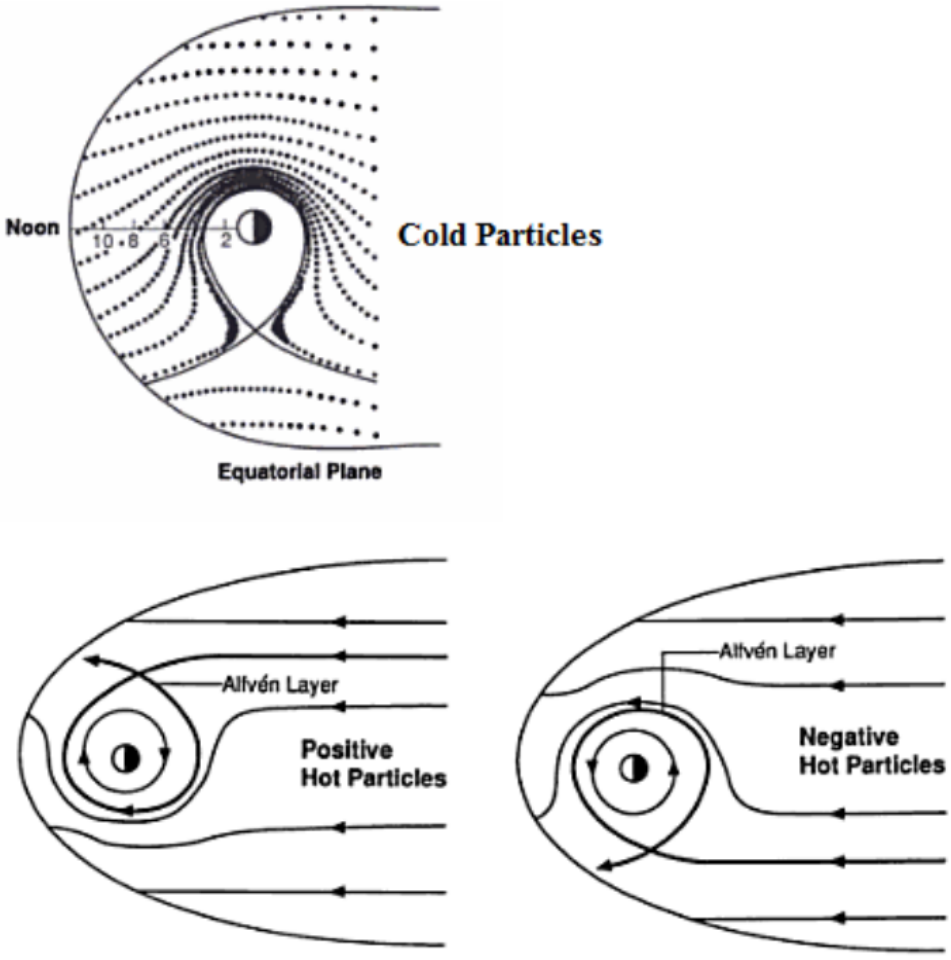

Figure 1.6: Drift paths of cold magnetospheric particles (top) and hot ions and electrons (bottom). From *Kivelson et al.* (1995) Fig 12.25 and 12.26.

1.4 Mangetosphere Ionosphere Thermosphere (MIT) Coupling during the Storm Time

The solar wind, magnetosphere, ionosphere and thermosphere are strongly coupled. Complex interactions within the MIT system makes it difficult to predict the responses to disturbances in the solar wind. In this section, a brief introduction of various coupling processes and interactions in the MIT system is given.

1.4.1 Magnetosphere-Ionosphere Interaction

Magnetosphere acts neither as a pure current nor as a pure voltage generator (*Ridley et al.*, 2004). The magnetosphere-ionosphere system is fully coupled along the magnetic field lines. There are various mass, momentum, and energy exchanges between them, making them highly linked, such that they cannot be treated independently.

1.4.1.1 Field-Aligned Currents

FACs play an important role in conveying stress and electric field between the magnetosphere and the ionosphere. In the high-latitude region, statistically there are two pairs of FACs, named Region-1 and Region-2 FACs. As shown in Fig 1.7, the Region 1 FACs map to higher latitudes with upward current on the dusk side and downward current on the dawn side. On the contrary, the Region 2 FACs map to lower latitudes and flow downward at dusk and upward at dawn.

Hasegawa and Sato (1979) provided a framework of the formation of the FACs in the magnetosphere. With the assumption of isotropic pressure in the magnetosphere, FACs can be expressed as:

$$J_{\parallel} = B \int [\frac{\rho}{B} \frac{d}{dt}(\frac{\Omega}{B}) + \frac{2}{B^2}\mathbf{J}_{\perp} \cdot \nabla B + \frac{1}{\rho B}\mathbf{J_{in}} \cdot \nabla \rho] dl_{\parallel}, \tag{1.1}$$

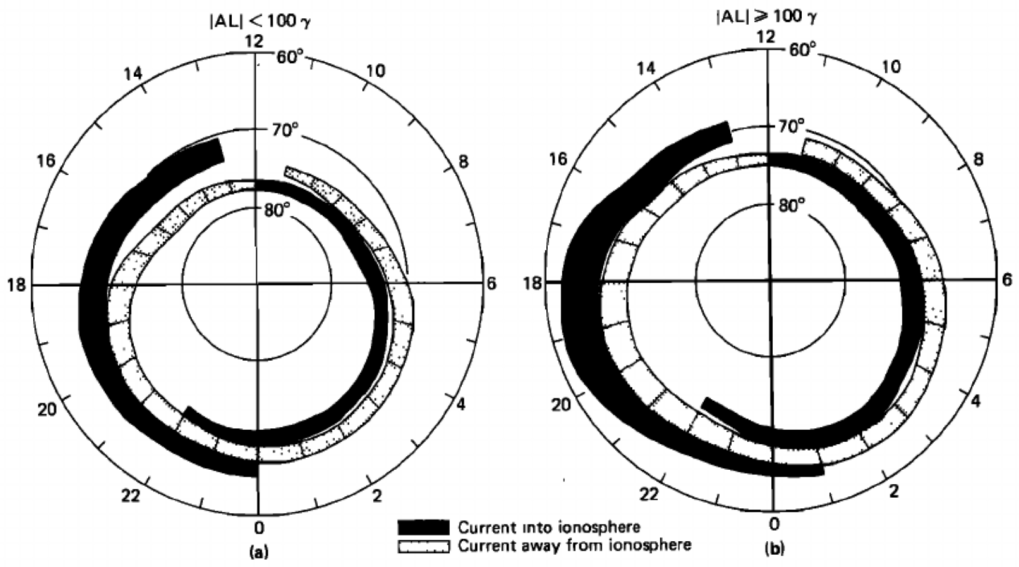

Figure 1.7: A summary of the distribution and flow directions of large-scale field-aligned currents determined from (a) data obtained from 439 passes of Triad during weakly disturbed conditions ($|AL| < 100$ nT) and (b) data obtained from 366 Triad passes during active periods ($|AL| > 100$ nT). From *Iijima and Potemra* (1978) Fig 13.

where B is the magnetic field in the magnetosphere, ρ is the plasma mass density, Ω is the vorticity, $\mathbf{J}_\perp$ is the current perpendicular to the magnetic field line, $\mathbf{J_{in}}$ is the inertia current, defined as $\mathbf{J_{in}} = -\frac{\rho}{B^2}\frac{d\mathbf{v}}{dt} \times \mathbf{B}$. The integration is from the magnetospheric equator to the ionosphere.

In this expression, the first term shows the effect of dynamic change of vorticity of flows and magnetic flux density, the second term shows the effect of the spatial variation of the magnetic field in the direction of the perpendicular current $\mathbf{J_{perp}}$, and the third term shows the effect of ion acceleration in the direction perpendicular to B and $\nabla\rho$.

In the magnetotail, flow bursts can generate a pair of small-scale FACs. The flow bursts from the nightside reconnection site can carry magnetic flux tubes to the near-earth region (*Birn and Hesse*, 2013). As shown in Fig 1.8, in the near-Earth region where the magnetic field is more dipole-like, the flow can brake or be diverted around the Earth. During this time, the first and third terms in Equation 1.1 become

important and generate Region-1 sense FACs. On the earthward side of the Region-1 sense FACs, there are opposite vorticities and Region-2 sense FACs. However, the amplitude of the Region-2 sense FACs are smaller than that of the Region-1 sense FACs.

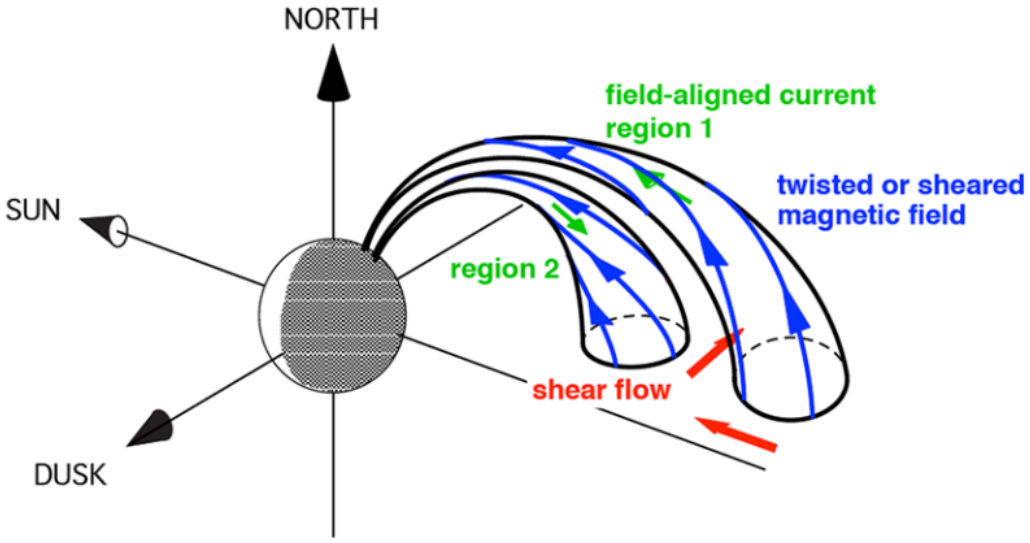

Figure 1.8: Build-up of a current system resulting from the shear outside and inside the diverted flow. From *Birn and Hesse* (2013) Fig 1.

The large-scale Region 1 currents in Figure 1.7 are suggested to be generated by the field-aligned vorticity at the flankside of the magnetosphere through a viscous interaction and are strengthened by the twist of the open magnetic field lines in the tail region during southward IMF (*Ogino*, 1986). In the inner magnetosphere, the inertia term in the MHD momentum equation is relatively small, the generation of FACs can be expressed in a simpler way (*Vasyliunas*, 1970):

$$J_{\parallel} = \frac{B_m}{2B_e}[(\nabla V) \times (\nabla P)] \cdot \hat{b}, \tag{1.2}$$

where B_e is the magnetic field in the magnetospheric equator, B_m is the magnetic field in the ionopshere, P is the plasma thermal pressure, V is the magnetic flux tube

volume, $\int \frac{dl}{B}$ and $\hat{b}$ is the direction of the magnetic field. The integration is along the entire magnetic field line. $J_{\parallel}$ is field aligned current density per unit area in the ionosphere and positive when flowing into the ionosphere. The FACs in Equation 1.2 is equivalent to the the second term in Equation 1.1. The plasma pressure associated with the partial ring current peaks near the midnight. The largest contributions to the FACs generation are from the azimuthal pressure gradient in the partial ring current and the radial magnetic flux tube gradient, the product of which gives downward FACs in the pre-midnight sector and upward FACs in the post-midnight sector (*Wolf et al.*, 2007). In other words, the westward partial ring current closes through the Region-2 FACs (*Wolf et al.*, 2007).

1.4.1.2 Conductance

Due to the continuity of currents, the FACs flow in and out of the ionosphere and close through horizontal currents within the ionosphere. The detailed closure of the FACs in the ionosphere depends on the conductivity and can be described as *Ridley et al.* (2004):

$$J_R(R_I) = [\nabla_{\perp} \cdot (\Sigma \cdot \nabla\Psi)]_{R=R_I}, \tag{1.3}$$

$$\Sigma = \begin{Bmatrix} \Sigma_P & \Sigma_H & 0 \\ -\Sigma_H & \Sigma_P & 0 \\ 0 & 0 & \Sigma_{\parallel} \end{Bmatrix}, \tag{1.4}$$

where Σ is the ionospheric height-integrated conductance tensor, and Ψ is the electric potential. The distribution of electric fields and currents in the ionosphere is mainly determined by the conductivity or its height-integrated version, conductance. It is the temporal and spatial variations of the ionospheric electrodynamic pattern that make it more than just a screen of the magnetospheric processes. The conductivity

in the same direction as the electric field is termed Pedersen conductivity, while that in the orthogonal direction is called Hall conductivity. The conductivity is given by (*Brekke and Moen*, 1993):

$$\sigma_P(z) = \frac{eNe(z)}{B(z)}[\frac{\nu_{en}\Omega_e}{\nu_{en}^2+\Omega_e^2} + \sum_i C_i \frac{\nu_{in}\Omega_i}{\nu_{in}^2+\Omega_i^2}], \tag{1.5}$$

$$\sigma_H(z) = \frac{eNe(z)}{B(z)}[\frac{\Omega_e^2}{\nu_{en}^2+\Omega_e^2} - \sum_i C_i \frac{\Omega_i^2}{\nu_{in}^2+\Omega_i^2}], \tag{1.6}$$

where $Ne(z)$ is the electron density, Ω represents the gyro frequency, ν is the collision frequency, i represents the major ion species (e.g. O^+, O_2^+, NO^+) and C_i represents their number abundance of different ions. ν_{en} represents the collision frequency between electrons and neutrals, and ν_{in} represents the collision frequency between different ions and neutrals (e.g. N_2, O_2, O). Physically, above around 175 km, the ions and electrons are colissionless and follow $E \times B$ drift. Below this, the ions collide with the neutrals and end up moving at an angle with respect to the electric field. On the other hand, electrons in the ionosphere above 70 km always follow $E \times B$ drift. The separation of the electrons and ions sets up a current in the E region that has two components: the Pedersen current is mainly due to the ion motion and the Hall current is due to both the ion and electron motions. A typical conductivity profile at a mid-latitude region is shown in Fig 1.9 (*Kelley*, 2009). The peak of the Hall conductivity is usually around 110 km, while the peak of the Pedersen conductivity is usually around 130 km. In addition, the magnitude of the Hall conductivity is usually larger than that of the Pedersen (*Baumjohann and Treumann*, 1997).

1.4.2 Ionosphere-Thermosphere Interaction

The domains of the ionosphere and the neutral thermosphere largely overlap. The frequent collisions between them lead to strong and complex coupling between the

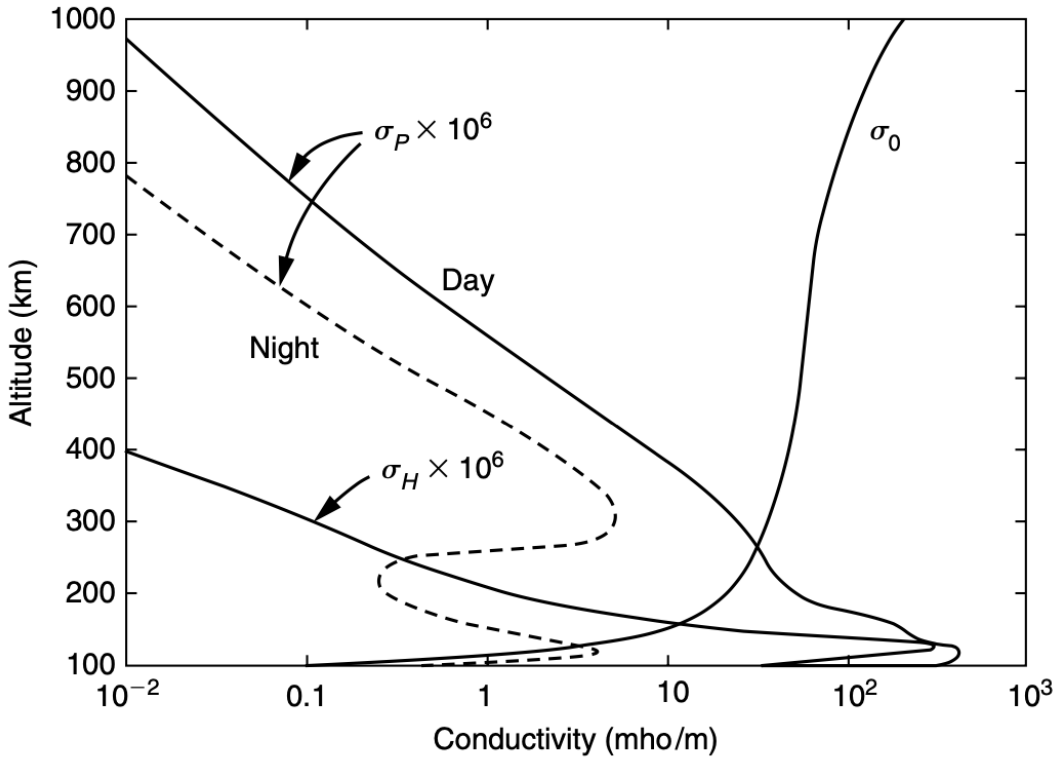

Figure 1.9: A typical conductivity profile at a midlatitude region: The solid line is the daytime value and the dashed line is the nighttime value. From *Kelley* (2009) Fig 2.6.

charged and neutral species. Depending on their relative bulk speed, temperatures, and densities, the plasma convection flows can exchange momentum and energy with the neutrals. Meanwhile, the change of the temperature and the density of neutrals can further influence the plasma density and thus affect the rate of momentum and energy transfer between the ionosphere and the magnetosphere. There are both positive and negative feedback mechanisms in the ionosphere-thermosphere system, as described below.

1.4.2.1 Mass continuity Equation

With the incompressible plasma assumption at high latitudes, the mass continuity equation of the ionospheric plasma is

$$\frac{\partial n}{\partial t} + \mathbf{u} \cdot \nabla n = P - L, \tag{1.7}$$

where n is the plasma density, $\mathbf{u}$ is the plasma velocity, P is the production rate, and L is the loss rate. The second term on the left represents the effect of advection due to the plasma drift and the density gradient. The plasma drift can primarily be affected by three sources: electric field, neutral wind, and ambipolar diffusion along the magnetic field lines.

The low energy plasma in the ionosphere follows the $E \times B$ drift and moves along the equipotential lines of the two-cell convection pattern. Since the Earth's magnetic field is nearly vertical in the polar region, the $E \times B$ convection flows are largely in the horizontal direction. However, away from the magnetic poles, the inclination angle of the Earth's magnetic fields decreases, and the field line deviates from purely vertical. In this case, the $E \times B$ drift will have a small but non-negligible vertical component (*Heelis et al.*, 2009; *Zou et al.*, 2014). This small vertical component turns out to be important in determining the ionosphere density morphology during the storm time (*Heelis et al.*, 2009; *Zou et al.*, 2014). In addition, at midlatitudes, neutral winds can push plasma move along the magnetic field lines through collisions (*Schunk and Nagy*, 2009). During storm times, strong equatorward winds on the nightside can push plasma upward and equatorward. Ambipolar diffusion due to vertical temperature or density gradients also transports plasma along the magnetic field lines (*Schunk and Nagy*, 2009).

The vertical drifts can move the ionosphere plasma to lower or higher altitudes, while the horizontal drifts can transport plasma across latitudes and longitudes. Both of them can affect the lifetimes of the F-region plasma density and create various density structures and gradients, which can be dramatically enhanced during storm times.

1.4.2.2 Chemical Processes

As shown in Equation 1.7, the plasma density change is also coupled to the neutrals through the production and loss rates. The production of ionospheric plasma can be due to two main sources: photoionization on the dayside and particle precipitation. Either a photon or precipitating electron/ion can provide the energy to ionize the neutrals and form ionospheric plasma (*Schunk and Nagy*, 2009). Three major photoionization processes are (*Schunk and Nagy*, 2009):

$$O + h\nu \rightarrow O^+ + e^-, \tag{1.8}$$

$$O_2 + h\nu \rightarrow O_2^+ + e^-, \tag{1.9}$$

$$N_2 + h\nu \rightarrow N_2^+ + e^-, \tag{1.10}$$

Process 1.10 is more important in the E-region, while process 1.8 is more important in the F-region. According to 1.8, when the atomic oxygen density increases in the sunlit region through some processes, such as lifting of atomic oxygen, the F-region production rate P increases.

When the atomic ions and electrons collide with each other, they may recombine into neutrals through the radiative recombination process. In the F region, the recombination rate between O^+ and e^- is on the order of $10^{-12} cm^3 s^{-1}$, which is a slow process. However, there is an alternative loss mechanism in the F region through a two-step dissociative recombination process. The first step is the charge exchange between O^+ and molecular species:

$$N_2 + O^+ \rightarrow NO^+ + N, \tag{1.11}$$

$$O_2 + O^+ \rightarrow O_2^+ + O. \tag{1.12}$$

The second step is the recombination between the molecular ions and electrons:

$$NO^+ + e^- \rightarrow N + O, \tag{1.13}$$

$$O_2^+ + e^- \rightarrow O + O. \tag{1.14}$$

The dissociative recombination rate is in the order of $10^{-7} cm^3 s^{-1}$, which is much faster than that of the radiative recombination (*Schunk and Nagy*, 2009). This shows that the loss rate of O^+ is primarily controlled by the molecular density. When the density of the molecular species increases, the loss process then accelerates. Combining the fact that the F-region production rate being driven by the oxygen density and the loss rate being driven by the molecular species density, the thermospheric composition changes can affect the density of the ionospheric plasma (e.g. *Kil et al.*, 2011).

When the plasma vertical drifts transport the F-region plasma to higher altitudes, where the density of the molecular neutrals is lower, the charge exchange rates are lower, such that the plasma life time increases. If there is continued production, the Total Electron Content (TEC) can increase (*Heelis et al.*, 2009; *Zou et al.*, 2014). Conversely, if there are downward drifts, the TEC will decrease. Here, TEC represents the total number of electrons integrated between two points, along a tube of one meter squared cross section, i.e., the electron column integrated number density. NmF2 and hmF2 are another two important parameters to characterize the ionosphere. NmF2 represents the F2-layer peak electron density, and hmF2 represents the altitude of the peak.

1.4.2.3 Ion Neutral Collision

During the storm time, the two-cell convection pattern forms in the ionosphere, and the plasma convection velocity can become much larger than that of the neutrals.

When the ions collide with the neutrals, the ions can give momentum to the neutrals. Thus, the neutrals are accelerated in the direction of the convection flow. This is called the ion-drag acceleration. At the same time of the collision, some ion mechanical energies are converted to the frictional heating of both ions and the neutrals, since the heating rate is proportional to the velocity difference squared. The changes of the thermospheric and ionospheric temperatures in turn influence the chemical processes in the ionosphere-thermosphere system, due to the charge exchange rate and recombination rate being related to the ion and electron temperatures, respectively.

1.5 Storm-Time Ionospheric Density Structures

During storm times, different kinds of electron density structures form in the ionosphere, which are usually accompanied by large electron density gradients and thus can influence the propagation of radio signals (*Wernik et al.*, 2003). These structures are the major space weather concerns in the upper atmosphere that can disrupt navigation and communication signals during geomagnetic disturbances. These storm-time electron density structures vary in spatial scale, from thousands of km to several km or less. Below is a list of storm-time electron density structures that have been investigated in this study.

1.5.1 Ionospheric Storm

Ionospheric storms refer to large-scale changes in the ionospheric electron density during geomagnetic storms. Due to the ionosphere's strong electromagnetic coupling to the solar wind-magnetosphere and the collisional coupling to the thermosphere, the responses of the ionosphere are quite complex during storms. In the mid-latitude region, the electron density can either increase or decrease during the storm. The duration when the ionosphere density is larger than the quiet-time value is referred to as a positive storm, while the duration when the density is smaller than the quiet-

time value is referred to as a negative storm. Fig 1.10 show the TEC observed at Sagamore Hill during the storm of 14 May 1969. The positive phase occurred soon after the storm initiated and was short-lived, i.e., several hours, while the negative phase lasted for several days.

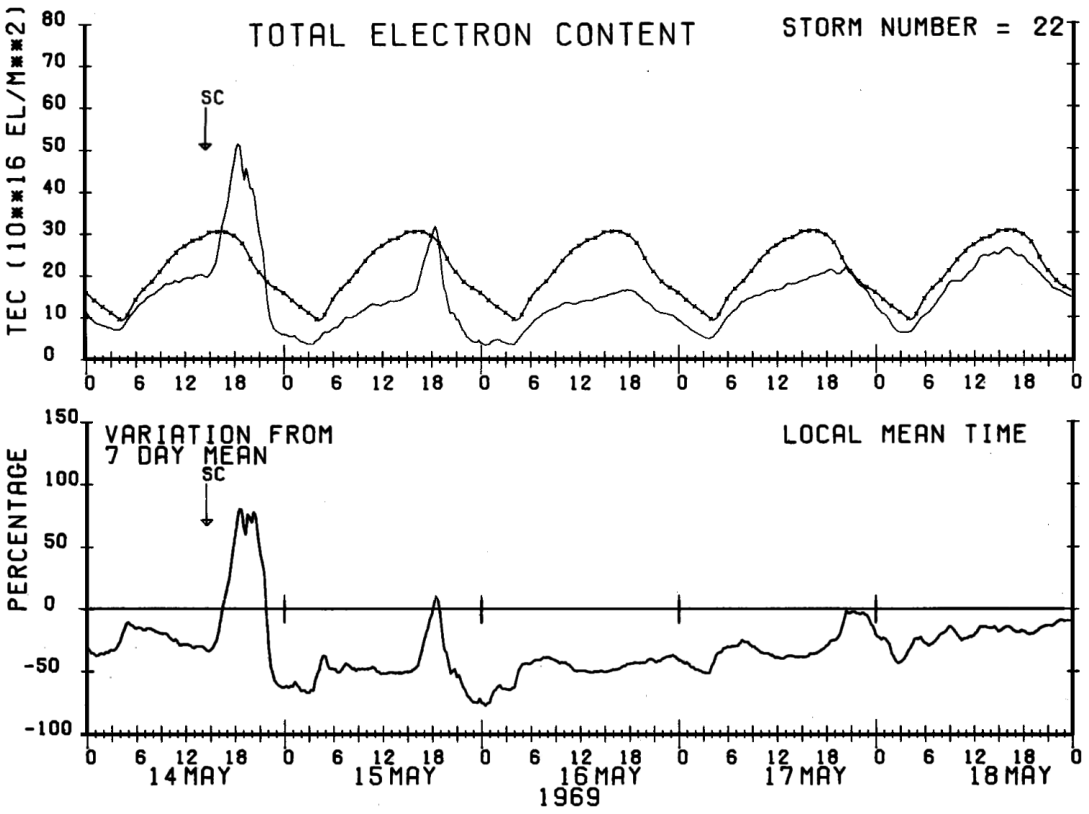

Figure 1.10: TEC pattern observed at Sagamore Hill during the storm of 14 May 1969 using the ISR at nearby Millstone Hill. From *Mendillo* (2006) Fig 3.

Several drivers have been shown to influence the electron density at mid-latitudes directly or indirectly, e.g. Joule heating, particle precipitation, penetration electric fields, disturbance dynamo electric fields, neutral winds, as well as thermosphere composition (*Prölss*, 1995; *Mendillo*, 2006, and references therein). The interplay between these drivers produces different responses and leads to a strong spatial and temporal dependence of the ionosphere density/TEC response.

The ionospheric responses during storms exhibit strong latitudinal dependence. At high latitudes, structured external electric fields and particle precipitation from the

solar wind and magnetosphere mainly control the ionospheric variability. Most times, the ionosphere can respond to these driving forces almost immediately. At low- and mid-latitudes, the response of the ionosphere to external forcing can also be complex. The penetration electric field can quickly reach low latitudes right after the southward turning of the IMF (*Huang and Foster*, 2007; *Kelley et al.*, 2003). Later, with the development of the partial ring current in the nightside equatorial magnetosphere, the Region 2 FACs grow and gradually shield the low-latitude ionosphere from the penetration electric field (*Wolf et al.*, 2007). The Region 2 FACs connect the partial ring current to the ionospheric closure currents, and are downward into the ionosphere on the dusk side and upward out of the ionosphere on the dawn side. At the same time, as the penetration electric fields exist, the neutral winds can also change the electric fields at mid and low latitudes. Heating at high latitudes reduces or even reverses the pressure gradient from the low to high latitudes, altering the wind structures and creating what is called the disturbance winds. Because the winds interact with the ions through collisions, a disturbance dynamo electric field is set up (*Lu et al.*, 2012; *Maruyama et al.*, 2005). The combination of the penetration/shielding and disturbance dynamo electric fields affects the electrodynamics in the low- and mid-latitude regions. The shielding time scale and the traveling time of the equatorward thermospheric disturbance winds are important for understanding the low and mid-latitude ionospheric responses during the storm time.

Besides the latitudinal dependence, the ionospheric responses during storms are also dependent on local times. *Prölss* (1995, and references therein) showed that the positive storms prefer to develop on the day side, while the negative storms prefer the early morning sector. With the assumptions that the positive ionospheric storms are caused by equatorward meridional winds and the negative ionospheric storms by neutral composition change, *Prölss* (1993) explained the local time asymmetry by invoking the fact that the meridional disturbance winds are easier to travel to lower

latitudes on the night side. In addition, the high-latitude energy depositions are not symmetric in local time but is displaced toward the dark hemisphere (*Prölss*, 1980). *Maruyama et al.* (2005) showed that the contributions of the disturbance dynamo electric field and the penetration electric field are comparable on the night side, while the latter is more important on the day side. *Mannucci et al.* (2009) also showed that the TEC peaks near the equator can develop at different local times during different storms and further studies with more data are required to understand the local time differences between the neighboring days. Recently, *Zhou et al.* (2016) found that the TEC at low and mid latitudes increased in the morning sector while decreased in the afternoon sector during the recovery phase of the 2015 St. Patrick's Day storm. This surprising observation is attributed to a combination of stronger vertical plasma drift and meridional wind in the morning sector. *Xiong et al.* (2019) focused on the different responses of Asian and American sectors on Sep 9-11, 2017 during the late recovery phase. When the American (Asian) sector was on the day side during 19-20 UT (7-8 UT) on Sep 11, the ionosphere experienced a negative (positive) storm. They suggested that the diurnal and semidiurnal tidal components contribute to these opposite responses.

1.5.2 Storm-Enhanced Densities (SEDs)

In recent years, due to thousands of ground-based Global Navigation Satellite System (GNSS) receivers, we are able to monitor the 2D ionosphere TEC changes continuously, and thus our understanding of the ionospheric storm positive and negative phases has increased significantly. SEDs are electron density enhancements (positive phase) that often occur in the mid-latitude region from postnoon to dusk sector during storm times. Figure 1.11 shows the 2-D GPS TEC map during the main phase of the 24–25 October 2011 storm. There was a TEC increase on the dayside near the equatorward boundary of the convection cell, which is termed SED.

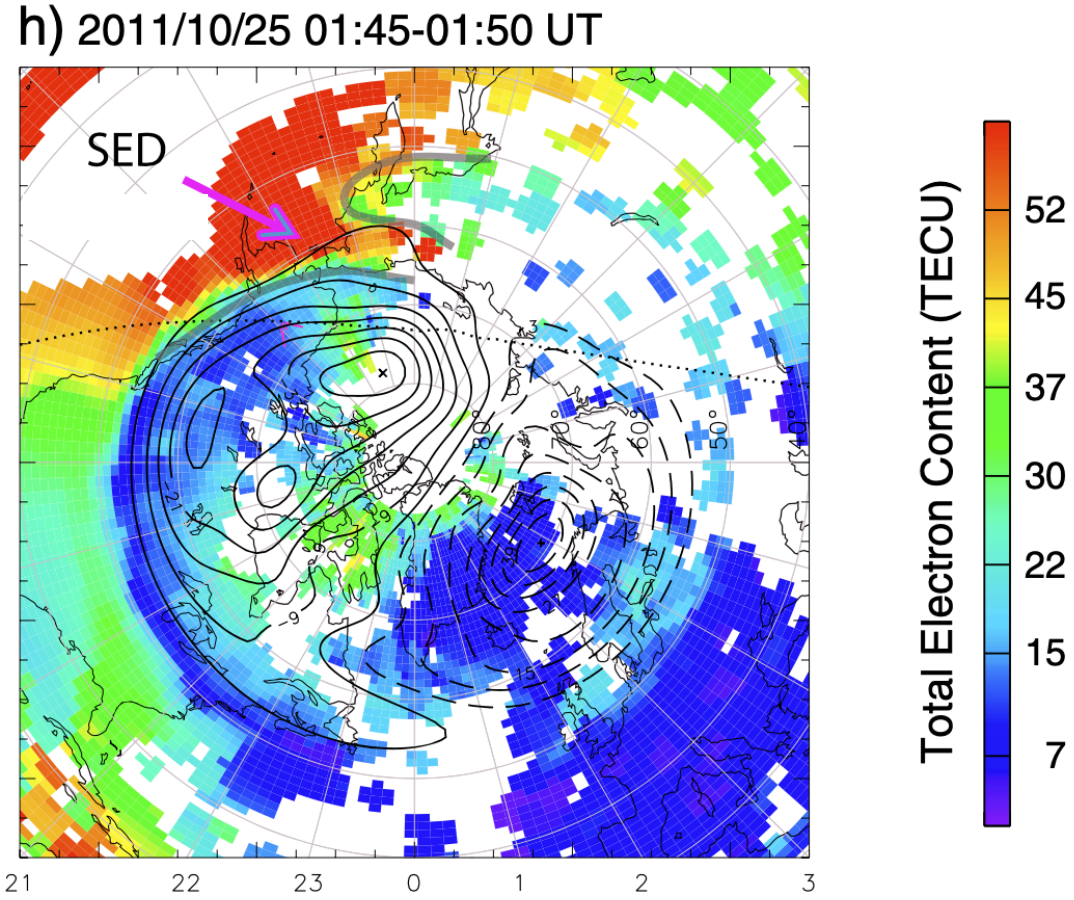

Figure 1.11: 2-D GPS TEC map during the main phase of the 24–25 October storm. Ionospheric equipotential contours derived from the SuperDARN radar observations are also shown. In each panel, magnetic noon/midnight is at the top/bottom, and dusk/dawn is toward the left/right. PFISR beams are also plotted as magenta segments. From *Zou et al.* (2013) Fig 2.

There are several formation mechanisms of SEDs. *Mannucci et al.* (2009) proposed that SEDs are generated by the plasma previously lifted from the equator and descending along the magnetic field line in the mid-latitude region due to the super fountain effect. The super fountain effect is evidenced by the fact the Equatorial ionization anomaly (EIA) can reach 25° to 40° geographic latitude during super storms (Dst<-250 nT). However, during moderate and intense storms, the SEDs are clearly separated from the EIA. To account for this observation, studies proposed that the enhanced density/TEC is generated by the local imbalance between production and

loss, and the imbalance is due to plasma vertical lifting (*Heelis et al.*, 2009; *Lu et al.*, 2012; *Zou et al.*, 2013). Both equatorward neutral winds and eastward electric fields can lift the plasma to higher altitudes and give rise to SEDs. At the same time, the longer life time allows that plasma can be transported for significant periods of time, so they can trace the ion convection pattern and be carried into the high latitude region and even the polar cap, forming SED plume/Tongue of Ionization (TOI) and polar cap patches. Thus, SEDs are recognized as an important plasma source for the high-latitude ionosphere.

1.5.3 Polar Cap Patches

Polar cap patches are F-region plasma structures in the polar cap, where the density is much higher than the background level (often a factor of two increase). They are closely related to SED plume/TOI, but during the formation of SED plume/TOI, the density is segmented to form discrete structures, instead of a continuous stream. Fig 1.12 show the electron density observed by Resolute Bay ISR-Canada. Each density peak represents one polar cap patch.

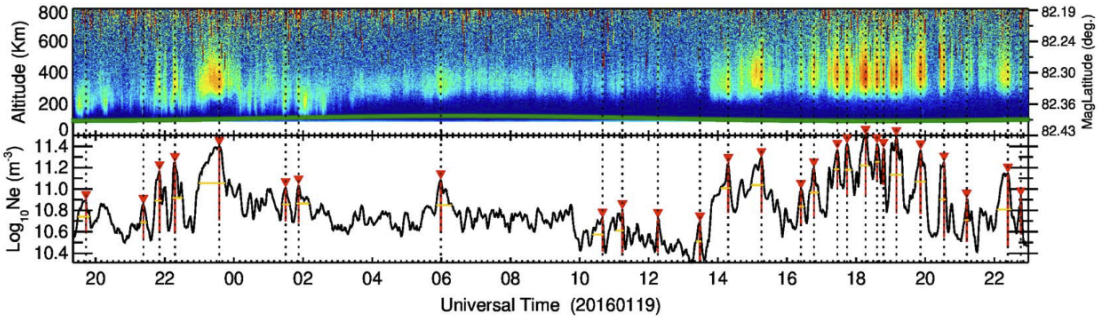

Figure 1.12: An example of a series of patches observed by Resolute Bay ISR-Canada on 19 January 2016. The first panel shows the electron density obtained directly from power with no range integration and no correction for measured temperature. In the second panel, black curve shows average electron density from 250 to 400 km with a 3-point median filter applied. The density peaks that fulfill the criteria mentioned in the text are marked by red triangles. Within each peak, the vertical red line and horizontal yellow line indicate its prominence and half-prominence width, respectively. From *Ren et al.* (2018) Fig 1.

Various formation mechanisms of the patch segmentation have been proposed, and it is still controversial which mechanisms are the dominant under which conditions. However, it is typically believed that the formation of a patch needs a reservoir of high-density plasma and a segmentation mechanism. There are two sources of the high-density plasma: The first source is the plasma density increase in the cusp due to soft precipitation in the F region (*Walker et al.*, 1999; *Rodger et al.*, 1994; *Goodwin et al.*, 2015). The second source is the vertically lifted dense plasma from the sunlit region (*Anderson et al.*, 1988), as described above. SEDs are considered to be an important plasma source for patches. However, Since the cusp and the throat region are overlapping, it is often difficult to distinguish between plasma from cusp precipitation and SEDs. *Ren et al.* (2018) showed that the altitude profiles of patch density and temperature resemble those of SEDs. The patch density is usually higher than the sector median above 200 km and lower than that below 200 km, i.e., a signature of plasma lifting, and the average patch electron temperature is lower than that of the surrounding region, which is a strong evidence that at least some patches originate from SEDs instead of particle precipitation.

The dense plasma of SEDs can be transported into the high-latitude region to form SED plume or TOI (*Foster*, 1984). To isolate the plume into patches, a segmentation mechanism is needed. It is generally believed that the segmentation is closely related with IMF variations. Patches can be segmented due to the temporal changes in both IMF B_z (*Anderson et al.*, 1988) and B_y (*Sojka et al.*, 1993; *Milan et al.*, 2002). Patches can also be generated by the Flux Transfer Event (FTE) near the cusp region (*Lockwood and Carlson*, 1992; *Carlson et al.*, 2004, 2006). FTE can lead to meso-scale (about 100 km) fast flow channels near the cusp (*Pinnock et al.*, 1993; *Oksavik et al.*, 2006) which could bring dense plasma into the polar cap region (*Rodger et al.*, 1994; *Lockwood and Carlson*, 1992; *Zhang et al.*, 2011). *Moen et al.* (2006) further showed that the pulsed return flow due to transient reconnection can chop the plume into

patches in the subauroral region. Another possibility is exactly opposite: fast flow jets due to transient reconnection produce high-temperature and low-density plasma through enhanced frictional heating and erode the pre-existing plume into patches (*Ogawa et al.*, 2001; *Valladares et al.*, 1994, 1996). *Zhang et al.* (2016) showed that Sub-Auroral Polarization Streams (SAPS) can transport low-density plasma from the night side to cut the SEDs into patch during a substorm. All of the above studies emphasize the important role of structured ionospheric convection flows either due to varying external conditions or internal dynamics.

1.5.4 Sub-Auroral Polarization Streams (SAPS)

SAPS are another structured flows that have the potential to segment the SEDs into patches. In this work, SAPS include both subauroral ion drifts (SAID) and polarization jets. SAPS refer to high-speed westward convection flows ($>$ 100 m/s) in the sub-auroral ionosphere spanning 3 to 5 degrees in latitude and extending from the afternoon to the early morning sector (*Foster et al.*, 2002; *Kunduri et al.*, 2017). In the equatorial magnetosphere, SAPS correspond to large electric fields pointing radially outward from the center of the Earth, and are usually observed between the ion and electron plasma sheet inner boundaries and near the plasmapause (e.g. *Califf et al.*, 2016; *Kim et al.*, 2010; *Nishimura et al.*, 2008). An example of SAPS is given in Fig 1.13. SAPS was located equatorward of the auroral oval and was accompanied with a decrease of the electron density, which is called the mid-latitude trough.

SAPS plays an important role in the transport and loss of plasma in the subauroral region, e.g. SAPS is proposed to carry low-density plasma from the dusk side to the dayside, generating the trough. In addition, because of the large flow velocities in SAPS, SAPS can drive enhanced frictional heating through collisions with neutrals and increase the charge exchange rate, which enhances the mid-latitude trough. In addition, its counterpart in the magnetosphere can also erode the plasmasphere and

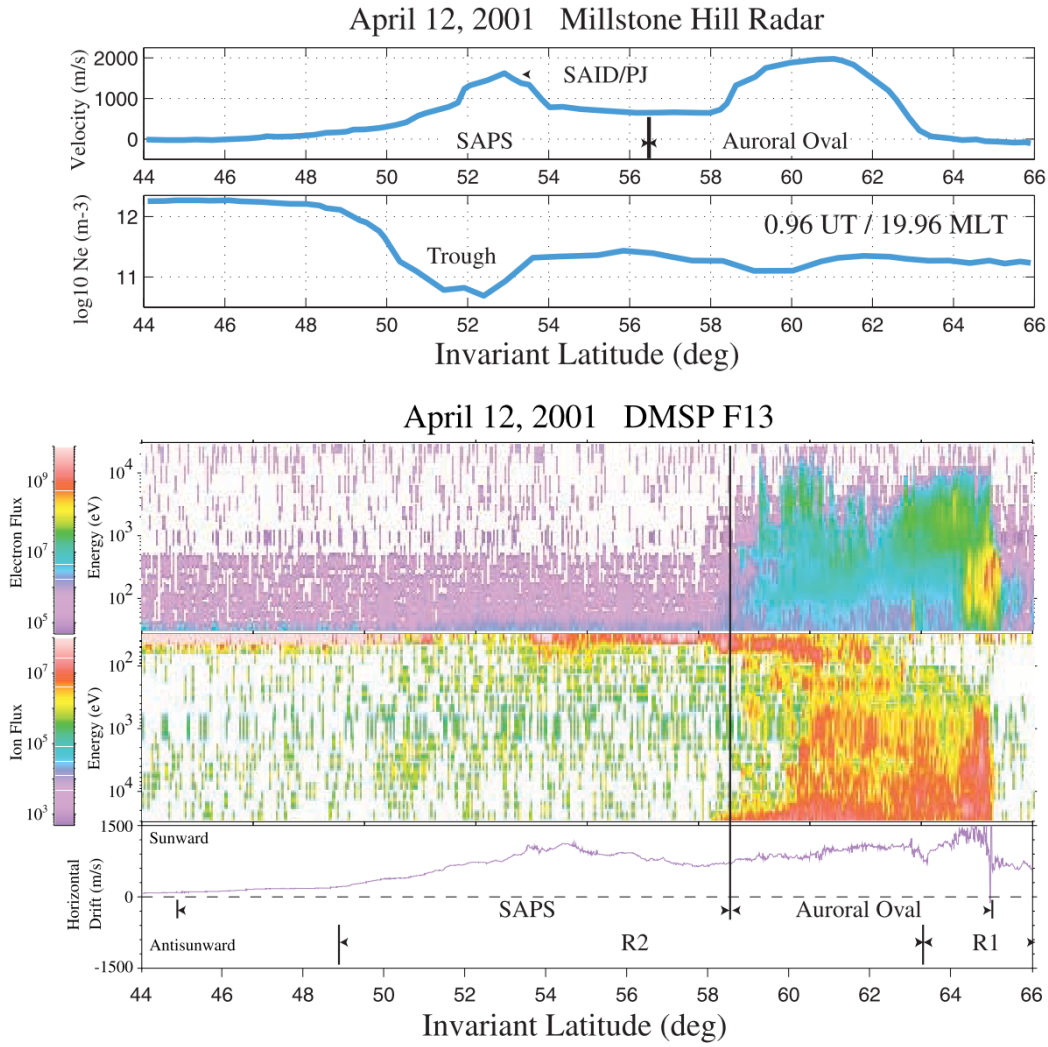

Figure 1.13: Millstone Hill Incoherent Scattering Radar (ISR) and simultaneous DMSP pass across the SAPS at 2000 MLT. The SAPS appears as a region of strong westward ion velocity, equatorward of the auroral two-cell convection and coincident with a deep ionospheric trough. Adapted from *Foster et al.* (2002) Fig 1.

create a steep plasmapause.

The formation mechanism of SAPS is a very active topic in the community, and there are a few different mechanisms proposed. The current generator theory works as follows (*Anderson et al.*, 1993; *Southwood and Wolf*, 1978): When the convection increases in the equatorial magnetosphere, a partial ring current can build up on the night side with large azimuthal pressure gradient. The azimuthal pressure gradient together with the gradient of the magnetic field flux tube volume in the radial direction

can generate the Region-2 FACs. On the dusk side, the Region-2 FACs flow into the ionosphere, and close through the poleward Pedersen currents and the Region-1 FACs at higher latitudes. When the Region-2 downward FACs are located earthward of the electron plasma sheet inner boundary, where the particle precipitation induced conductance is low, a large poleward electric field, i.e., SAPS, in the current closure region is needed to maintain the current continuity. Later, *De Keyser* (1999) proposed that the combined effect of finite gyroradius induced thermo-electric field and the background convection electric field at the front of the substorm particle injection, when it reaches the plasmapause, can account for the SAPS formation. In addition, *Mishin and Puhl-Quinn* (2007) pointed out that the short circuiting of the particle injection into the plasmasphere can explain the SAPS formation. According to their theory, when the injected particles enter the plasmapause, energetic electrons stop, but ions can move further inward, which form a charge separation layer. This charge separation gives rise to the SAPS electric field.

Besides the dynamics in the magnetosphere, the large convection flow speed and associated enhanced frictional heating in the ionosphere may increase the conversion rate of atomic O^+ to molecular NO^+ and increase the dissociative recombination rate. In addition, enhanced frictional heating leads to the elevated ion temperature and ion scale height, and thus enhances the vertical transport (*Heelis et al.*, 1993). As a result of the enhanced frictional heating, the density and conductivity can further decrease, creating a positive feedback effect on the SAPS electric fields (*Banks and Yasuhara*, 1978; *Schunk et al.*, 1976).

All of the above mentioned SAPS formation mechanisms suggest that SAPS should occur during the enhanced earthward transport of plasma sheet plasma during geomagnetic active times. Therefore, the SAPS occurrence and characteristics during geomagnetic storms and substorms have been studied extensively using observations. *He et al.* (2017a) showed that SAPS occur within 0-1.5 h after the southward turning

of IMF during intense storms. In general, it was found that SAPS move to lower magnetic latitudes and cover larger geomagnetic longitude ranges as Kp increases or Dst decreases (*Foster et al.*, 2002; *Huang and Foster*, 2007). The peak SAPS flow speed enhances and the electron density within the SAPS reduces when Dst decreases (*Erickson et al.*, 2011). Recently, *Kunduri et al.* (2017) showed that the occurrence rate of SAPS can reach over 80% during geomagentic storms ($Dst < -50nT$). In addition, *Wang et al.* (2008) also showed that larger cross polar cap potentials are related with larger speed of SAPS, and *Anderson* (2004) showed that the subauroal potential drop across SAPS is positively correlated with the absolute value of Dst. During storm time, a couple of event studies showed that SAPS can last for more than 10 hours (*Burke et al.*, 2000; *Califf et al.*, 2016). This is further confirmed by *Lejosne and Mozer* (2017) using two years of Van Allen Probes data. In their results, the average lifetime of SAPS is 9 hours, which is comparable to the duration of the storm main phase.

The relationship between SAPS formation and substorms have been investigated, and it has been shown that SAPS can last from 30 min to 3 hours during a substorm (*Anderson et al.*, 1991; *Makarevich et al.*, 2009; *Puhl-Quinn et al.*, 2007). The coupled global BATSRUS MHD model and kinetic ring current model results further indicated that SAPS can last for 2-3 hours (*Buzulukova et al.*, 2010; *Yu et al.*, 2015). Although the duration of SAPS and substorms is roughly comparable, we still do not understand the detailed relationship between substorm onsets and SAPS. Observationally, SAPS have been shown to occur at different phases of a substorm in different cases. Many studies reported that SAPS can form in the expansion and recovery phase, lagging the substorm onset by 6-30 min (*Anderson et al.*, 1993, 2001; *Karlsson et al.*, 1998; *Makarevich et al.*, 2011; *Mishin*, 2016; *Puhl-Quinn et al.*, 2007; *Wang and Lühr*, 2011). *Anderson et al.* (1993) further explained this delay: after the onset, ion and electron plasma sheet boundaries need about 10 min to separate and provide the low

conductivity region. However, a much quicker response of SAPS to the onset was later reported, from 30 sec after onset (*Nishimura et al.*, 2008) to 2 min (*Zou et al.*, 2009a,b). *Zou et al.* (2012) reported that SAPS can start to form even in the growth phase after the convection starts to increase, as part of the nightside Harang reversal. This is consistent with the current generator theory that SAPS should be able to form following the enhanced convection.

1.5.5 Birkeland Current Boundary Flows (BCBF)

BCBF are latitudinally narrow ion velocity jets similar to the SAPS. Thus, BCBF also have the potential to segment the SEDs into patches. The main difference is where and when they tend to occur, as shown in Figure 1.14. BCBF are sandwiched by the Region 1 and Region 2 FACs, while SAPS appear near the equatorward boundary of the Region 2 FACs and in the subauroral region. Some FACs morphologies previously associated with SAPS can also applied to BCBF (*Archer and Knudsen*, 2018). *Archer et al.* (2017) show that under quiet conditions ion velocity jets exceeding 1 km/s and spanning less than 100 km meridionally are observed in over half of quiet-time auroral crossings and appear to be a persistent property of quiet time current closure.

1.5.6 Interhemispheric Asymmetry

During storm times, the northern and southern hemispheres can experience opposite ionospheric storms, e.g., the positive storm in the northern hemisphere and the negative storm in the southern hemisphere. In general, due to the seasonal thermosphere composition variation, the negative storms are stronger in the summer hemisphere (*Prölss*, 1995), while stronger positive storms prefer the winter hemisphere (*Goncharenko et al.*, 2007). *Duncan* (1969) pointed out that the effect of a storm is to enhance the photochemical mechanism that is dominant for that season.

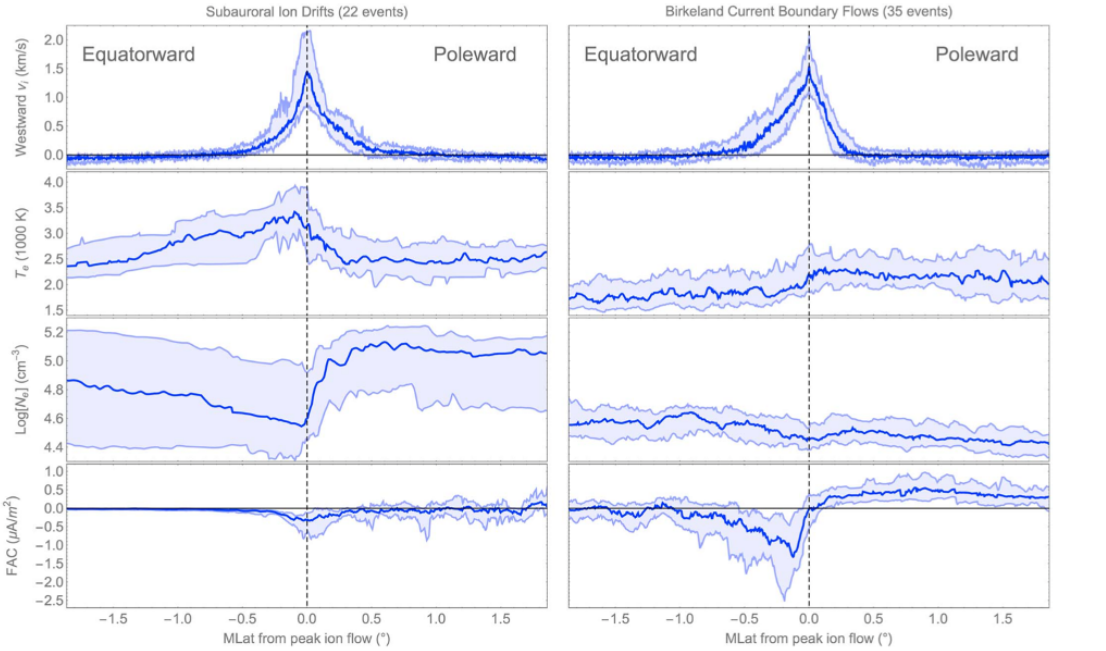

Figure 1.14: Superposed epoch plot plasma parameters measured by Swarm A surrounding (left column) SAID and (right column) BCBF plotted as a function of distance from maximum westward ion flow. The first through third quartiles for each parameter are shaded in light blue; median values are shown in dark blue. Rows from top to bottom: (1) Horizontal cross-track ion velocity estimated from TII L0 16 Hz first moments assuming 100% NO+ ion composition. (2) Electron temperature measured by Langmuir probe. (3) Plasma density measured by Langmuir probe. (4) FAC estimated from Swarm vector magnetometer measurements assuming passing normal through infinite current sheets. Adapted from *Archer and Knudsen* (2018) Fig 2.

Interestingly, it is found recently that the hemispheric asymmetry can develop opposite trends at different ionospheric layers. *Astafyeva et al.* (2015a) showed that the enhancements of TEC and F2 peak density are more prominent in the winter hemisphere, while the topside ionosphere measurements show increase in the summer hemisphere and no change or even decrease in the winter hemisphere.

However, not all storms follow the general seasonal trend. *Astafyeva et al.* (2020) presented a puzzling case where opposite hemispheric asymmetries occurred during different phases of the Aug 25, 2018 storm. During the storm main phase, a strong positive ionospheric TEC storm was observed in the northern (summer) hemisphere,

while no storm-time deviation occurred in the southern (winter) hemisphere. The preference of the TEC positive storm for the summer hemisphere is opposite to what earlier studies found for other storms (*Goncharenko et al.*, 2007). *Astafyeva et al.* (2020) explained this puzzling asymmetry by invoking a combination of weak seasonal thermospheric winds and weak photoionization in the southern hemisphere. However, during the recovery phase of this storm, the northern (summer) hemisphere experienced a strong negative storm, while no obvious negative storm signatures observed in the southern hemisphere (winter). This recovery phase asymmetry was similar to other storms and thus most likely driven by the background seasonal effect in combination with the storm-time changes in the thermospheric composition.

Astafyeva et al. (2015b) first showed the opposite hemispheric asymmetry of the ionospheric responses in different longitudes (local times) during the main phase and early recovery phases of 2015 St. Patrick's Day storm. Fig 1.15 shows the variations of VTEC measured by the ground-based GPS receivers in American, European-African, and Asian sectors during the 17–18 March 2015 storm. In the European-African sector, from 08 to 24 UT on March 17 (8-24 LT), stronger positive storm signatures were observed in the northern hemisphere. Meanwhile, in the American sector, from 21 UT on March 17 to 05 UT on March 18 (17-01 LT), southern hemisphere experienced positive storm and the northern hemisphere experienced a negative storm. The authors suggested that the asymmetry in the American sector can be explained by the composition changes supported by observations from the TIMED GUVI, while the asymmetry in the European-African sector is more complicated. Besides the composition effect, other factors, including the asymmetry in the geomagnetic field and the amplitude and direction of the IMF B_y, may lead to the observed TEC asymmetry in the European-African sector. Later, *Yue et al.* (2016) also showed that in TIEGCM simulations, the Apex geomagnetic fields can generate a stronger asymmetry in the neutral wind and composition than the dipole field.

1.6 Motivation of the Dissertation

As described above, significant progress has been made in our understanding of the MIT responses during storms. However, there are still many open questions. Below is a list of open questions that we explored using a combination of comprehensive observations and state-of-the-art numerical simulations in the following chapters:

- Earlier studies suggest that segmentation of the SED plumes into polar cap patches either needs transient reconnection on the dayside or fluctuations in the solar wind and IMF. However, there are polar cap patch events generated during steady conditions lack of either of them. Thus, a new segmentation mechanism is needed to be able to account for patch events in this category. In Chap II (*Wang et al.*, 2019b), we propose such a new mechanism by invoking the boundary flows and utilizing the state-of-the-art numerical simulation technique. The new theory is able to explain the segmentation during steady solar wind and IMF conditions, allowing improved agreement between the simulation outputs and the observations.

- Most studies found that SAPS can extend over a large spatial scale in the longitudinal direction, covering several hours of MLT (e.g. *Clausen et al.*, 2012; *He et al.*, 2018), and very few studies (*Oksavik et al.*, 2006) focus on meso- to small-scale SAPS variations. Recent studies have shown that small- and meso-scale FACs (e.g. *Lühr et al.*, 2015; *McGranaghan et al.*, 2017) and meso-scale flow channels, which are typically associated with streamers and SAPS (*Gallardo-Lacourt et al.*, 2014, 2017), are both important components of the high-latitude ionospheric plasma dynamics. Considering the close relationship between SAPS and FACs, it is thus intriguing to study small- or meso-scale SAPS variation and the corresponding formation mechanism. In Chap III (*Wang et al.*, 2019a), with a combination of observations in the space and on the ground, the for-

mation mechanism of the meso-scale SAPS and the associated electromagnetic signatures are studied.

- Hemispheric asymmetries of ionospheric storms have been studied for years. However, with the much larger coverage of GNSS receivers on the ground, there is a renewed interest in studying the asymmetries. Interestingly, in some events, the asymmetries of TEC at different local times/longitudes have opposite polarities. Details of the development of the hemispheric asymmetries are still not well understood, especially those asymmetries opposite to the background seasonal effect and the conventional understanding. In Chap IV (*Wang et al.*, 2021), using a combination of observations in the space and on the ground, several potential drivers of the asymmetries are studied. It is found that the asymmetries of the plasma vertical drift, thermospheric composition change, and TID activity all contribute to the TEC asymmetries.

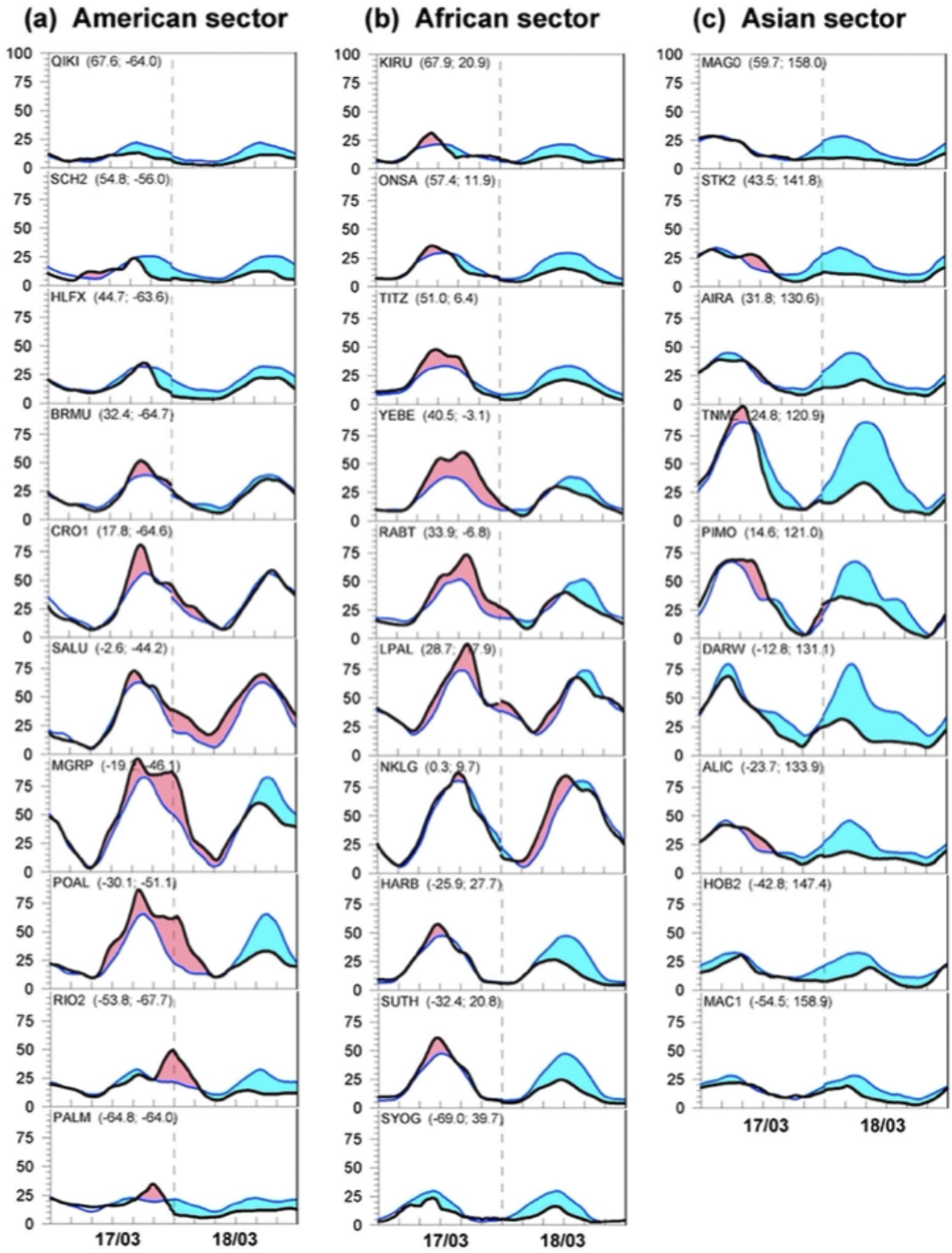

Figure 1.15: Variations of VTEC measured by the ground-based GPS receivers in (a) American, (b) European-African, and (c) Asian sectors during the 17–18 March 2015 storm (black curves). Names and coordinates of the receivers are shown in each panel. As a quiet time reference, we plot a median for 7 days before the storm (blue curves). Positive and negative deviations from the 7 day median value are filled by light red and light blue, respectively. The SSC of 04:45 UT time is shown by the vertical dashed lines; the thin gray vertical lines correspond to 00 UT of 18 March 2015. Adapted from *Astafyeva et al.* (2015b) Fig 3.

CHAPTER II

Segmentation of Storm Enhanced Density by Boundary Flows Associated with Westward Drifting Partial Ring current

2.1 Introduction

In this chapter, an interesting case of polar cap patches during the geomagnetic storm on Sep 7, 2017 was found. In this case, IMF B_y and B_z were stable and there were no fast flows associated with transient reconnection on the dayside magnetopause observed by SuperDARN. Thus, the formation of polar cap patches cannot be explained by the traditional theory. Instead, we proposed a new segmentation mechanism associated with boundary flows between region 1 and region 2 FACs. Global Ionosphere Thermosphere Model (GITM) was used to simulate and study the segmentation of SED plume into a polar cap patch. GITM was driven by the high-resolution coupled Block-Adaptive-Tree-Solar Wind-Roe-Upwind-Scheme (BATSRUS) and Rice Convection model (RCM) within the SWMF (*Tóth et al.*, 2005; *Tóth et al.*, 2012). Our results are not only consistent with observations, but also for the first time show that a strong boundary flow can form between the Region 1 and Region 2 FACs when the shielding developed and partial ring currents drift westward. This boundary flow can reduce the electron density and segment SED plume into a patch.

2.2 Model Description and Setup

2.2.1 BATSRUS

BATSRUS (*Powell et al.*, 1999) is a computational tool for describing environments using compressible MHD. The scheme is based on the same elements that make up many modern compressible gas dynamics codes: a high-resolution upwinding based on an approximate Riemann solver for MHD and limited reconstruction; an optimally smoothing multi-stage time-stepping scheme; and solution-adaptive refinement and coarsening. In addition, a method for increasing the accuracy of the scheme by subtracting off an embedded steady magnetic field is added. BATSRUS can be used to simulate the global magnetospheric responses with solar wind measurements of density, velocity, temperature and IMF components as inputs (e.g. *Buzulukova et al.*, 2010).

2.2.2 RCM

RCM (*Toffoletto et al.*, 2003) is a model of the inner and middle magnetosphere, including the ring current, plasma sheet and their coupling to the ionosphere. The RCM uses a bounce-averaged kinetic model and assumes an isotropic distribution function to solve for the collisionless Vlasov equation for the particles in this region.

2.2.3 Coupled BATSRUS and RCM

BATSRUS cannot provide adequate description of the inner magnetosphere (*De Zeeuw et al.*, 2004). The movement of particles with energy from 1 to 200 keV is not captured in the model, leading to a weaker pressure and region 2 FACs in BATSRUS. Thus, there is a need to couple RCM with BATSRUS to provide a more realistic description of the inner magnetosphere. The coupling process between BATSRUS and RCM is shown in Fig 2.1. BATSRUS provides plasma density, velocity, magneitc

field, pressure and ionospheric potential to RCM, and RCM feeds back its pressure to BATSRUS.

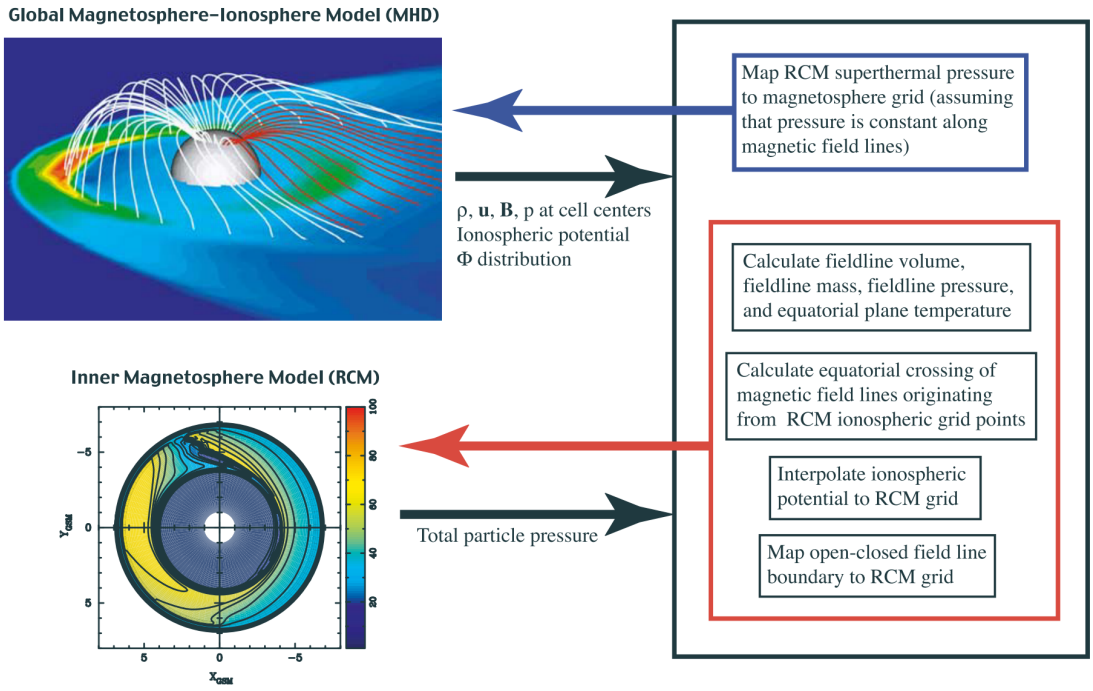

Figure 2.1: Exchange of information between BATSRUS and RCM models. Adapted from *De Zeeuw et al.* (2004) Fig 1.

2.2.4 GITM

GITM is a three-dimensional spherical grid that models the Earth's global ionosphere and thermosphere system self-consistently (*Ridley et al.*, 2006). In this study, the spatial resolution of GITM was set to 1 degree in latitude and 2 degree in longitude with 50 vertical levels (from $\sim$ 100 to $\sim$ 700 km). GITM allows different models of high-latitude electric fields, auroral particle precipitation, and solar radiation as inputs. In this study, the Flare Irradiance Spectral Model (FISM) (*Chamberlin et al.*, 2007) was used to provide solar irradiance input for the whole simulation. FISM is an empirical model of the solar irradiance spectrum covering from 0.1 to 190 nm with 0.1 nm wavelength resolution and 1-minute temporal resolution. Using the high-

resolution FISM model, the solar flare's impact on the ionosphere and thermosphere can be captured. This model is based on the data provided by the Solar Extreme ultraviolet Experiment (SEE) on the Thermosphere Ionosphere Mesosphere Energetics and Dynamics (TIMED) satellite (*Woods et al.*, 2005) and the Solar Stellar Irradiance Comparison Experiment (SOLSTICE) on the Upper Atmospheric Research Satellite (UARS).

2.2.5 Model Setup

At first, GITM was run for two quiet days (Sep 4-5) to achieve steady state. During this stage, the Fuller-Rowell and Evans empirical model (*Fuller-Rowell and Rees*, 1987) and Weimer empirical electric field model (*Weimer*, 2005) were used as the precipitation and electric field input, respectively. The Fuller-Rowell and Evans model is driven by Hemispheric Power (HP), which is found to be linearly related with $AL^{\frac{1}{2}}$ in *Østgaard et al.* (2002) empirical model. We used the observed AL index from the Kyoto WDC to calculate the hemispheric power. The Weimer model was driven by the observed solar wind data from OMNIWeb. Starting from Sep 6 00 UT, the high-latitude driver was switched to the electric field and precipitation from the 2-way coupled BATSRUS and RCM models, as part of the University of Michigan SWMF (*De Zeeuw et al.*, 2004; *Tóth et al.*, 2012). The coupled model was driven by the real solar wind data from OMNIWeb. High resolution grid ($1/8R_E$) in the inner magnetosphere, magnetopause and current sheet was implemented to better capture dynamic FACs and precipitation structures.

2.3 Dataset: TEC

TEC is the total number of electrons present along a path between a radio transmitter and receiver. The value of TEC depends on the path. The Vertical Total Electron Content (VTEC) is determined by integration of the electron density on a

route perpendicular to the ground. TEC can be derived from dual-frequency Global Navigation Satellite System (GNSS) measurements. In this work, we used the VTEC data with 5 min resolution that are available from the Massachusetts Institute of Technology Haystack Observatory Madrigal database *Rideout and Coster* (2006). The spatial resolution of the VTEC is 1° in latitude and 1° in longitude.

2.4 Observations

2.4.1 Solar Wind Conditions

An intense double-dip geomagnetic storm occurred on Sep 7-8, 2017 and has received much attention (*Aa et al.*, 2018, 2019; *Habarulema et al.*, 2020; *Imtiaz et al.*, 2020; *Jimoh et al.*, 2019; *Jin et al.*, 2018; *Lei et al.*, 2018; *Mosna et al.*, 2020; *Shen et al.*, 2018; *Wang et al.*, 2019a; *Xiong et al.*, 2019; *Zhang et al.*, 2019). The SYM-H index reached -142 nT during the first dip and then ∼-100 nT during the second dip. The double-dip storm was driven by multiple Interplanetary Coronal Mass Ejections (ICMEs) passing the Earth successively (*Shen et al.*, 2018). As shown in Figure 2.2, the IMF B_z turned southward at $\sim$ 2040 UT on Sep 7 due to the arrival of the first ICME, leading to the initial decrease of SYM-H. At $\sim$ 2330 UT, a shock-ICMEs complex structure arrived with the shock enhanced IMF B_z reaching ~ -30 nT. A sudden storm commencement signaled by the sudden SYM-H increase was also initiated by this shock. After that, the SYM-H continued to decrease due to the large southward IMF and reached the first minimum at $\sim$ 0100 UT. Then, the storm began to recover until the arrival of another ICME at $\sim$ 1105 UT on Sep 8, which led to the second main phase. In this study, we focus on the development and structuring of SEDs during the first main phase. In Figure 2.2f, the dashed line represents the simulated Dst index. Although there is a $\sim$ 20 nT negative bias, the temporal variation of the simulated Dst is consistent with the SYM-H index.

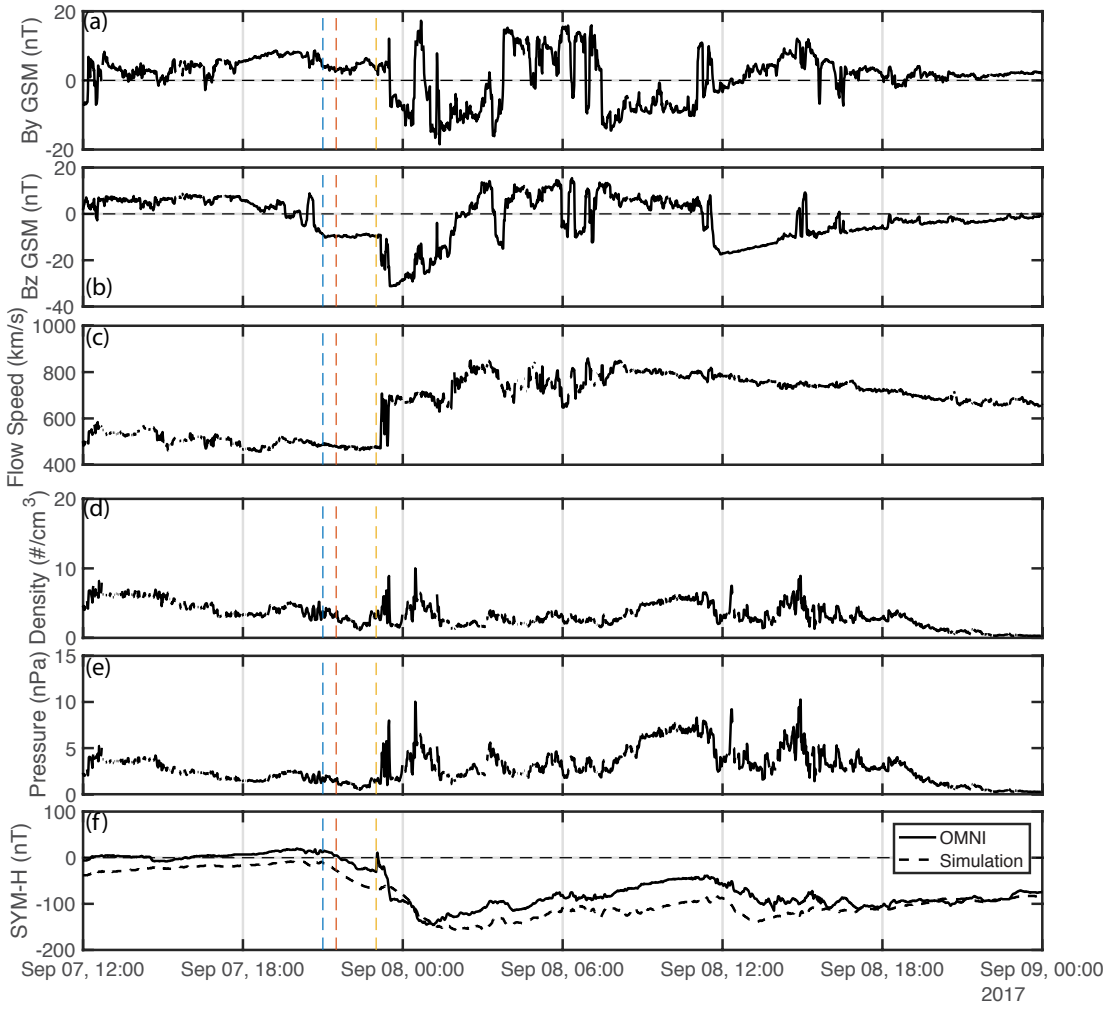

Figure 2.2: Solar wind data and geomagnetic index from 12 UT Sep 7 to 0 UT Sep 9, 2017. (a) IMF B_y component in the GSM coordinates, (b) IMF B_z component in the GSM coordinates, (c) solar wind speed, (d) proton number density, (e) solar wind dynamic pressure, and (f) the SYM-H index (solid line) and simulated Dst index (dash line). The color-coded vertical dashed lines indicate timing of the three snapshots in Figure 2.

2.4.2 VTEC Observations

The first row of Fig 2.3 shows the GPS VTEC in geomagnetic coordinates. It is shown that the SED and the plume began to develop after the southward turning of IMF, and the segmentation of the plume occurred at 2300 UT.

2.5 Simulation Results

The SED formation and patch segmentation processes are shown in the bottom three rows of Figure 2.3, with the color-coded vertical dashed lines in Figure 2.2 indicating the timing of the three snapshots (2100 UT, 2130 UT and 2300 UT). The bottom three rows in Figure 2.3 show the dynamical evolution of the ionosphere and inner magnetosphere from SWMF after the first southward turning. The second row shows the GITM electron density at 349.4 km with color contours and electric equipotential line contours every 10^4 V in the geomagnetic coordinates centered at the Magnetic North Pole. The third row shows the SWMF FACs with color contours and the same electric equipotential contours every 10^4 V in geomagnetic coordinates. The green dashed line represents the open-closed field line boundary (OCB). The bottom row shows the plasma pressure in the XY plane at Z=0 in GSM coordinates. Based on the comparison between the first and second row in Figure 2.3, it is shown that the simulation results successfully captured the development of the SED and the SED plume after 2100 UT, and the segmentation of the plume at 2300 UT.

As shown in Figure 2.2, the IMF B_z turned southward at 2040 UT on Sep 7, reaching -10 nT at 2100 UT, and stayed steadily southward for about 2.5 hours until the shock arrival at 2330 UT. Due to this southward turning, a two-cell convection pattern started to form, and the convection electric field penetrated to mid-latitudes. The convection also tilted towards the dawn side, which is likely due to the long lasting positive IMF B_y (*Weimer*, 2005). In the equatorial plane of the inner magnetosphere,

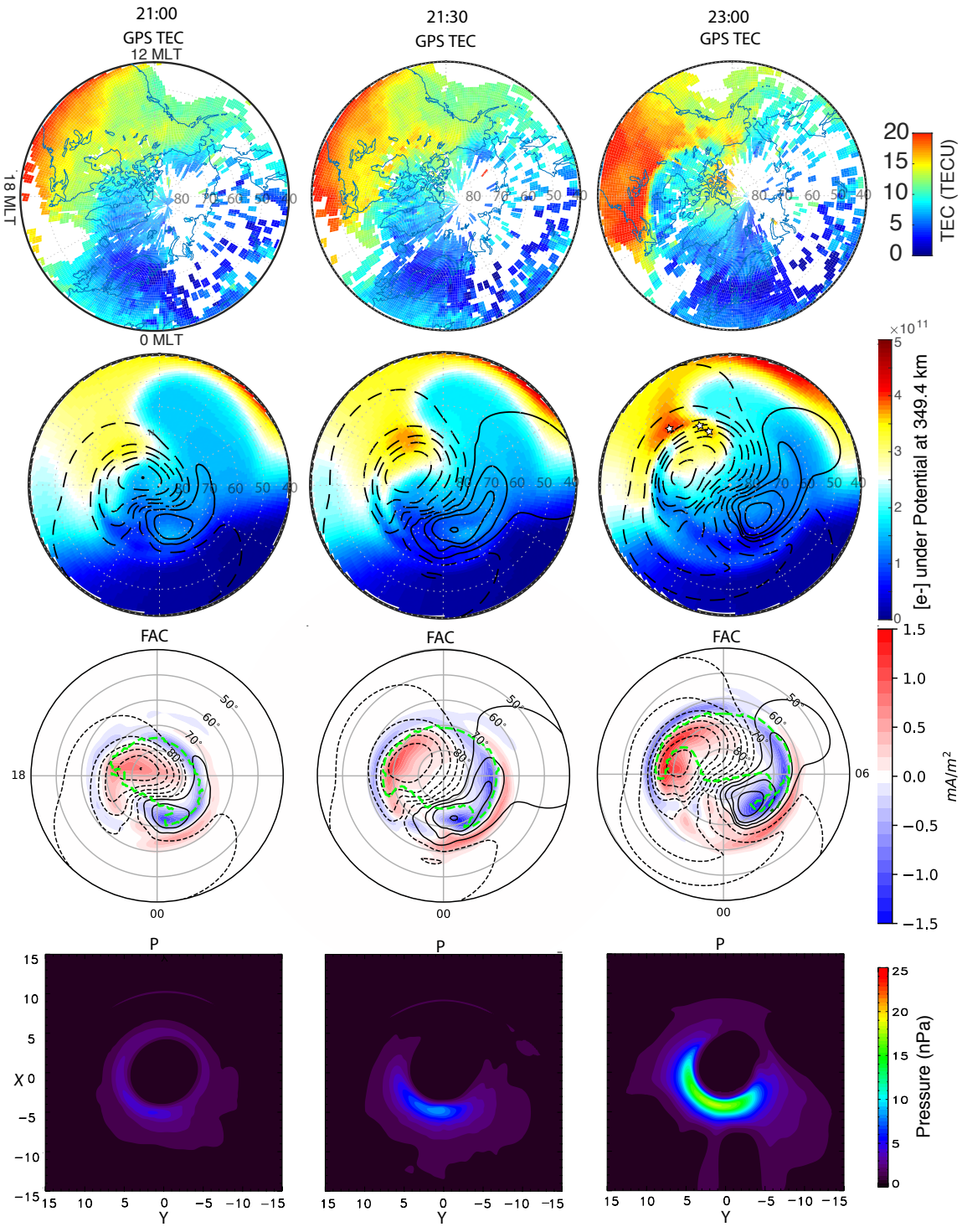

Figure 2.3: Continued on the following page.

a weak, nearly symmetric ring current can be seen at 21 UT. Both the Region 1 and Region 2 FACs existed. However, the Region 2 FACs were weaker than the

Figure 2.3: First row: Polar view of VTEC in the geomagnetic coordinates. Second row: Polar view of modeled electron density (color contours) at 349.4 km under electric equipotential (contour lines) in the geomagnetic coordinates. The **SED!** base, boundary flow and polar cap patch are marked with stars at 23 UT. Third row: Polar view of the modeled FACs (color contours) under electric equipotential (contour lines) in the geomagnetic coordinates. The green dashed line represents the open-closed field line boundary. Fourth row: the modeled plasma thermal pressure in the z=0 plane in the GSM coordinates.

Region 1 FACs, because of weak partial ring current. The penetration electric field was able to reach the plasma in the sunlit mid-latitude region. Both the two-cell convection pattern and OCB expanded to lower latitude. More plasma in the mid-latitude followed the convection to higher latitude. Because the magnetic field is not vertical in the subauroral and auroral region, the convection flow had an upward component and transported plasma to higher altitude, where the charge exchange and recombination rate is lower (*Heelis et al.*, 2009; *Zou et al.*, 2013, 2014). Lifting and horizontal advection led to the transport of the high-density plasma.

At 2130 UT, more plasma was transported from the plasma sheet to the inner magnetosphere due to the steady southward IMF, and the partial ring current developed on the night side. Because of the increase of the convection electric field, the plasma in the dayside ring current was not in a closed drift path anymore and drifted sunward to the magnetopause, which led to the disappearance of ring current on the day side. Together with continued buildup of ring current on the night side, the partial ring current formed with larger azimuthal pressure gradient and stronger Region 2 FACs according to the Vasyliunas equation (*Vasyliunas*, 1970). This led to stronger Region 2 FACs which flowed up from the dawnside ionosphere and down into the duskside. The partial ring current charged up positive on the duskside and negative in the dawnside to support the Region 2 FACs (*Wolf et al.*, 2007). This charge separation generated a dawnward electric field, which was opposite to the convection electric field. This is referred to as the shielding phenomenon. During this

period, the shielding effect began to grow. In general, the electron density in the mid-latitude SED base region can continue to grow as long as the convection electric field is not completely shielded, resulting a local maximum of electron density (see the electron density at 2130 UT in Figure 2.3). The high-density plasma then drifted further northward and into the polar cap region.

A detailed breakdown of the formation mechanism for SEDs is shown in Fig 2.4. As shown previously, electric field, neutral wind and diffusion can all contribute vertical drift. At 1800 UT, the IMF was northward, and there were weak electric fields in the high latitude region. At the same time, on the dayside, the poleward winds due to the sunlit pushed plasma downward. Thus, SEDs cannot form at this time. When the IMF turned southward at 2100 UT, the two-cell convection pattern formed. On the dayside, there was a strong eastward electric field and then upward $E \times B$ drift. Although there was still downward drift due to the neutral wind, the effect of the convection was much stronger. Thus, the SEDs began to develop after the southward turning of IMF. At 2130 UT, the convection increased, and the SEDs continued developing, leading to the electron density peak (SEDs) captured by both GPS VTEC and simulation. Although neutral wind is also suggested to contribute to the formation of SEDs, the enhancement of the convection pattern is more important in this case. Neutral wind may play an more important role in the late main phase and recovery phase when the thermosphere expands and generates strong equatorward winds. Note that in this case, the diffusion did not rely much on the IMF direction and its effect was weaker than that of the neutral wind and electric field.

At 2300 UT, the IMF B_z had been steadily southward for two hours. A strong partial ring current built up due to the persistent and strong transport from the plasma sheet to the inner magnetosphere. The peak pressure reached $\sim$20 nPa and the pressure gradient generated much stronger Region 2 FACs. Due to the shielding effect, the electric potential was gradually confined to the poleward part of the Region 2

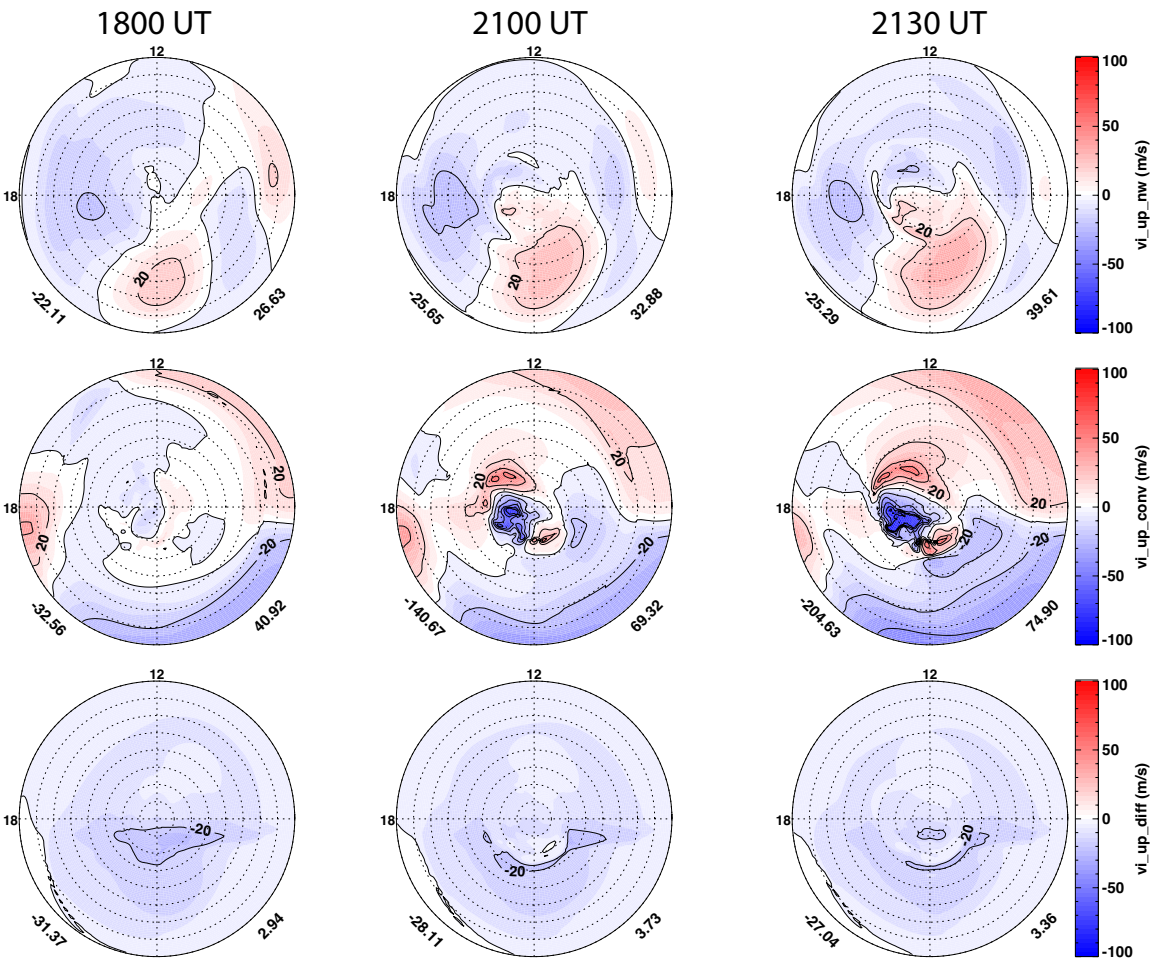

Figure 2.4: The three rows represent the contributions to the vertical drift from neutral wind, electric field and diffusion respectively.

FACs, and the penetrating electric field equatorward of the Region-2 FACs weakened. The direct impact of this electric field pattern change was the formation of intense plasma flows at the boundary between the Region-1 and Region-2 FACs at around 15 MLT, commonly referred to as the Birkeland Current Boundary Flows (BCBF) (*Archer et al.*, 2017; *Archer and Knudsen*, 2018). Associated with the boundary flows were increased electric field/velocity gradients on both sides. The BCBF flow seemingly transported the low-density plasma from the nightside to the dayside and also gradually eroded the high-density SED plume. As a result, a patch is segmented from the SED base. It is subsequently transported across the OCB and into the polar

cap.

2.6 Discussions

Segmentations were previously found to be related to the temporal change of IMF B_y and B_z (e.g. *Sojka et al.*, 1993; *Anderson et al.*, 1988; *Milan et al.*, 2002) or transient reconnection (*Lockwood and Carlson*, 1992; *Carlson et al.*, 2004, 2006), i.e. driven by dayside processes in the coupling between the IMF and the magnetosphere. In this case, between 2100 UT and 2300 UT, both IMF B_y and B_z were quite steady, ruling out the possibility of temporal changes of the IMF. Here we suggest that the segmentation is driven by processes internal to the magnetosphere, i.e., the boundary flows in the afternoon sector driven by westward drift partial ring current.

To gain further insight into the magnetospheric origin of the convection flows cutting the patch, a 3-D view of the simulated magnetospheric configuration at 2300 UT when the SED plume was segmented is shown in Figure 2.5. Color contours of plasma thermal pressure are shown in the cut plane XY at Z=-1 RE. Colors on the sphere at 3 RE are contours of the FACs (positive values mean upward FACs). Three white lines represent the sample field lines at the center of the SED base (GLAT=50.5, GLON=247), center of the boundary flows (GLAT=58.5, GLON=235), and patch (GLAT=63.5, GLON=231). The center of the SED base was where the electron density at 350 km reached the local maximum, the center of the boundary flow was where the electron density reached the local minimum, and similarly the center of patch was where the density reached local maximum. The footprints of these magnetic field lines are marked as black stars in Figure 2.3. The polar cap patch was on open magnetic field lines and connected to the solar wind, showing that its poleward movement was due to the magnetospheric convection driven by the southward IMF. The SED base was mapped to the inner edge of the partial ring current, where the under-shielded electric field was responsible for the SEDs lifting

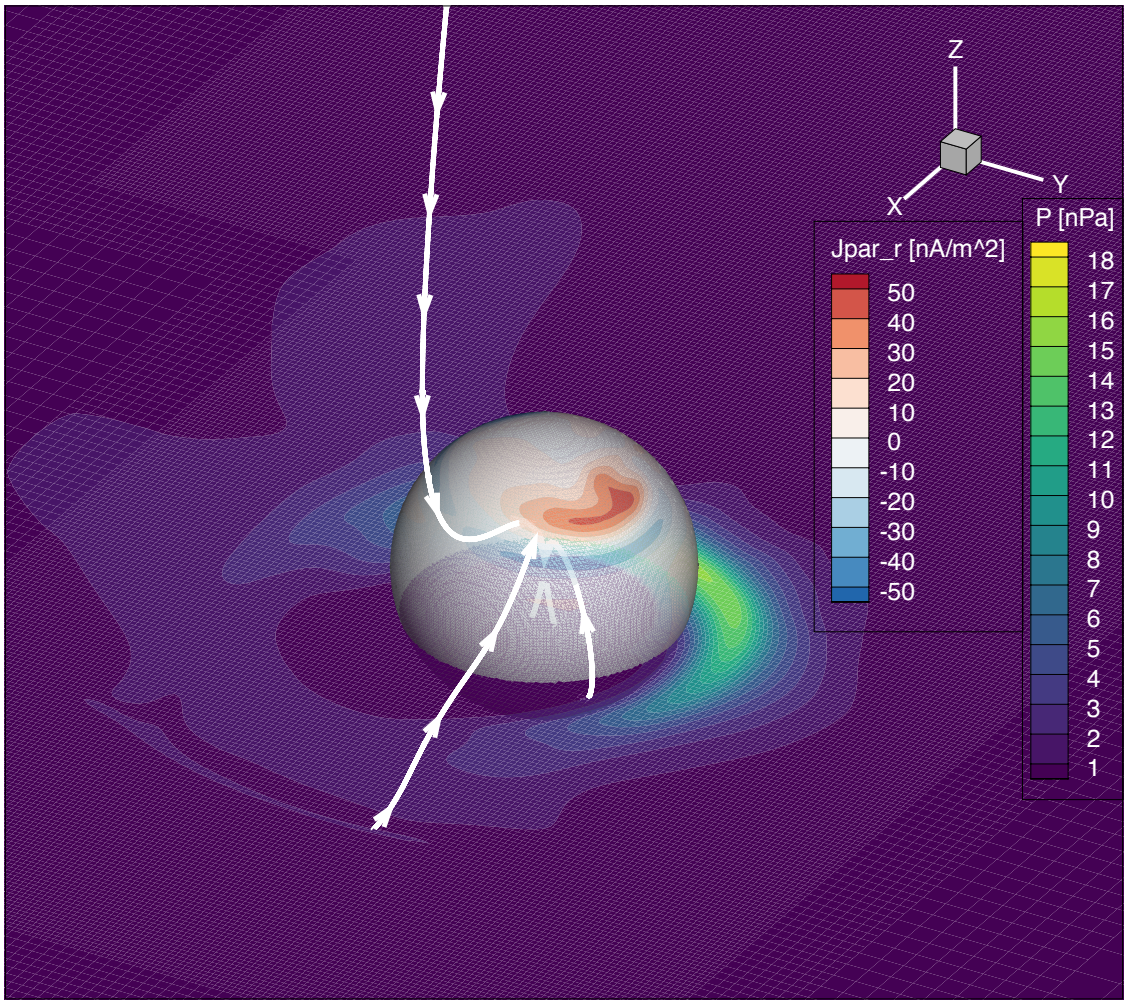

Figure 2.5: Continued on the following page.

and VTEC growth. This also explains why the SED base stopped providing plasma to the auroral region after the shielding further developed. The boundary flow region

Figure 2.5: A 3-D view of the simulated magnetosphere extracted from the time step when the SED plume was segmented at 23 UT. Shown in the cut plane XY at Z= -1 RE are color contours of the plasma thermal pressure. Color contours on the sphere with a radius of 3 RE indicate the field-aligned current density (positive values mean upward field-aligned currents). Three white lines represent the sample magnetic field lines at the SED base (the lowest lat.), boundary flow (the middle lat.) and patch (the highest lat.) around this time. The foot prints of these magnetic field lines are shown as stars in Figure 2.3

was mapped to the outer boundary of the partial ring current (poleward boundary of Region 2 FACs in the ionosphere). This proves that the segmentation was due to the boundary flows located between the Region 1 and Region 2 FACs.

We further investigated how the boundary flows segmented the SED plume into a patch. The plasma parcel at the center of the boundary flow at 2300 UT was traced backward in time to 2130 UT to identify its source region. The center of the boundary flow was located at MLAT=63.0, MLT=13.8 and marked with a white star in Figure 2.6c. It also co-located with the minimum of the electron density. The altitude profile of the electron density at 2300 UT is represented by the blue curve in Figure 2.6d. When the plasma parcel was traced back in time, it was found that the source region was located at MLAT=58.3, MLT=15.6 at 2130 UT and also marked with a star in Figure 2.6a. This proved that the plasma parcel was not from the nightside, excluding the possibility that the boundary flow carried low-density plasma from the nightside and segmented the SED plume. The plasma parcel experienced two development phases,i.e., a growing phase and a decaying phase. The growing phase started at 2130 UT and continued to 2225 UT. The corresponding altitude profiles of the electron density at these two time cadences are represented by the red and black curves in Figure 2.6d, respectively. During the growing phase, the plasma was lifted to higher altitudes, i.e., the hmF2 increased from 270 km to 320 km. The lifting was found to be mainly due to projection of the northward convection flows in the vertical direction. At the end of the growing phase, this plasma parcel was located at

MLAT=60.1, MLT=15.0, indicated by the star near the equatorward boundary of the boundary flow shown in the central panel of Figure 2.6b. The electron density at the hmF2 ($\sim$ 300 km) reached its maximum of $4.09 \times 10^{11} m^{-3}$ at 2225 UT. The decaying phase started at 2225 UT, and the electron density in the F-layer below 400 km region kept decreasing. The temporal evolution of the horizontal ion drift, electron density and ion temperature in the plasma parcel at around 350 km are shown in Figure 2.6e-g, respectively. The horizontal flow was mainly westward and increased during the whole period due to the constant southward IMF, continuously growing particle ring current and the associated Region-2 current system. The electron density reached the maximum at 2225 UT. After 2225 UT, the convection flow continued to increase, and the ion temperature also increased due to stronger frictional heating between the ions and neutrals, which resulted in an electron density decrease.

The loss mechanism is further quantified. When the plasma parcel moved from the source region to the boundary flow region, at 300 km (around hmF2) the velocity difference between ion and neutral increased from $\sim$100 m/s to $\sim$600 m/s, the ion temperature increased from $\sim$1400 K to $\sim$1700 K, and the neutral temperature remained at $\sim$1400 K. Based on the temperature-dependent dissociative recombination equations in *St.-Maurice and Torr* (1978), the charge exchange rate between O^+ and N_2 increased from $5.73 \times 10^{-13} cm^3 s^{-1}$ to $9.91 \times 10^{-13} cm^3 s^{-1}$, when the ion temperature increased from $\sim$1400 K to $\sim$1700 K. The N_2 density was $\sim 1.5 \times 10^{14} m^{-3}$ and O^+ density was $\sim 3 \times 10^{11} m^{-3}$ in the model output. The production rate of NO^+ thus increased to $1.88 \times 10^7 m^{-3} s^{-1}$. The total NO^+ conversion during the decaying phase ($\sim$ 35 min) was $4 \times 10^{10} m^{-3}$. Because the recombination between NO^+ and e^- is rapid, the electron density loss should also be $4 \times 10^{10} m^{-3}$, which matches the amount of electron lost between 2225 UT and 2300 UT in the model output. This simple calculation confirms that the enhanced chemical reaction within the enhanced boundary flows led to the electron density decrease and the segmentation of the SED

plume into a patch.

There are several proposed patch segmentation mechanisms with convincing evidence reported in previous literature, which highlights the complicated nature of the high-latitude ionospheric electrodynamics. In this numerical simulation, the partial ring current formed has a single pressure peak, and thus the associated FACs and flow pattern are relatively simple. However, the ring current can have fine structures (*Buzulukova et al.*, 2010; *Wei et al.*, 2019), and the associated FACs and flow pattern can be more complicated, which can potentially lead to more structures in the segmented patch. A local maximum of the convection flow and a local density minimum at 2235 UT in Figure 2.6e-g further confirms this idea.

SAPS is a similar phenomenon to the BCBF. SAPS is a strong westward flow at the equatorward edge of the auroral oval in the duskside, while BCBF is the flow between the region 2 and region 1 FACs due to the current closure in the ionosphere. *Zhang et al.* (2016) showed that SAPS carried low-density plasma into the dayside and segmented the SED plume. Based on the simulation results, it is suggested that SAPS also has the potential to segment the SED plume into a polar cap patch through frictional heating. However, it is hard to quantitatively differentiate the two mechanisms based on observations. Numerical simulation is needed to check the details about how SAPS segments the SED plume. On the other hand, SAPS is notoriously hard to simulate. As shown in *Lin et al.* (2019), a more concise precipitation and ring current model is needed to simulate SAPS accurately.

2.7 Summary and Conclusions

A new segmentation mechanism of SED plume into polar cap patches is proposed through numerical model study. A simulation of the ionospheric response to the geomagnetic storm on Sep 7, 2017 has been carried out using the GITM driven by the two-way coupled BATSRUS and RCM within SWMF. The simulation results are

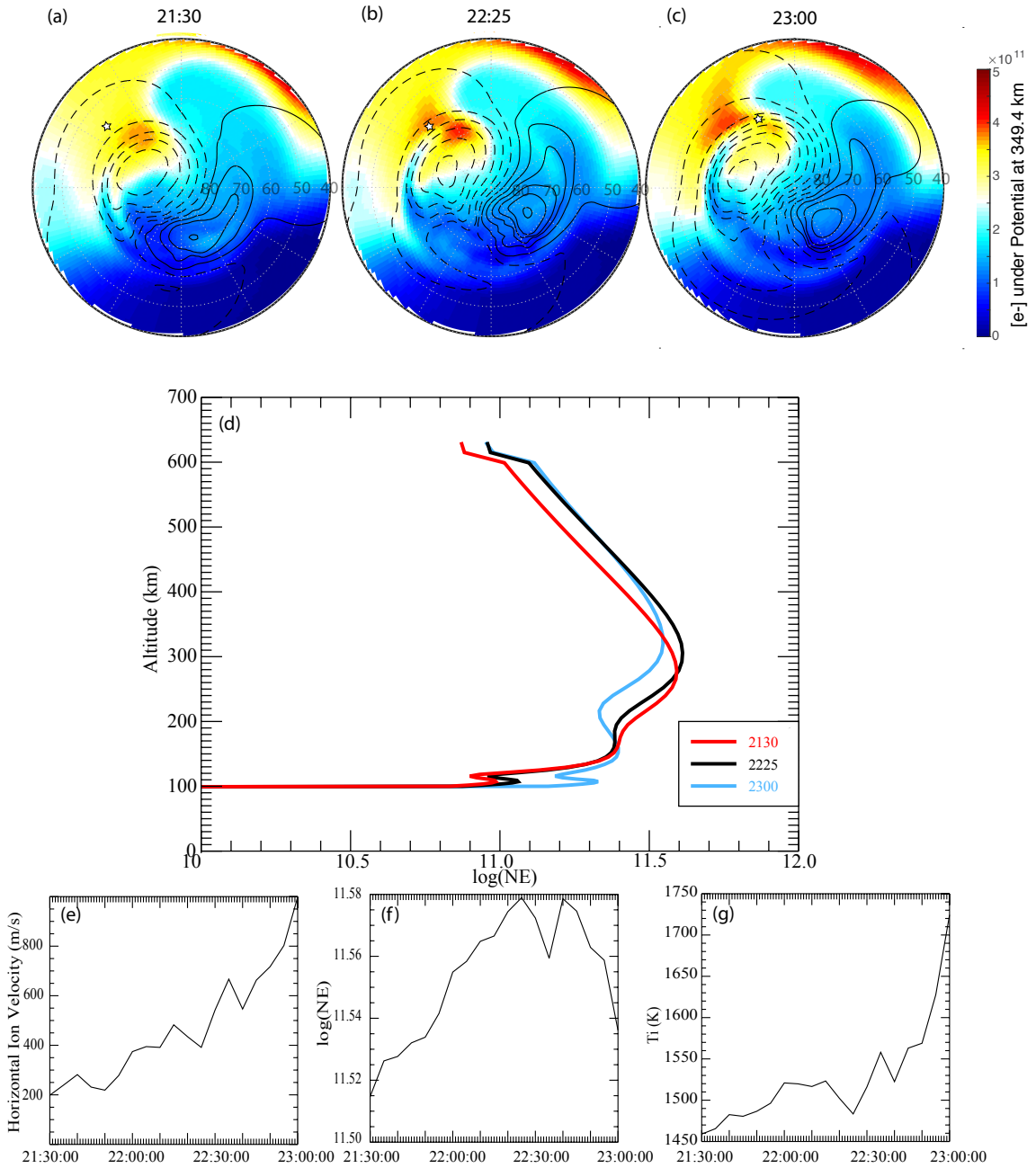

Figure 2.6: Continued on the following page.

validated by comparison to GPS VTEC observations and SYM-H index.

During storm time, dense plasma from the mid-latitude ionosphere is transported

Figure 2.6: One simulation plasma parcel is traced backward in time. The locations of the plasma parcel and altitude profiles of the electron density at three different time cadences are shown. (a)-(c) Polar view of the F-region electron density and the locations of the traced plasma parcel are marked with stars at 2130, 2225 and 2300 UT, respectively. The format of polar view plots of the electron density is the same as the second row in Figure 2. (d) The red curve indicates the initial density profile at 2130 UT, the black curve indicates the density profile at the end of the growing phase, i.e., 2225 UT, and the blue curve indicates the density profile at the end of the decaying phase, i.e., 2300 UT. (e)-(g) The temporal evolution of the horizontal ion drift, electron density and ion temperature in the plasma parcel at around 300 km.

by the expanded two-cell convection pattern into the high-latitude region to form the SED plume. The SEDs are mainly generated by the enhanced convection pattern in the high latitude region through lifting. Meanwhile, plasma from the plasma sheet is transported into the inner magnetosphere by strong earthward convection and forms a strong partial ring current centered on the nightside. The partial ring current closes through the Region 2 FACs and gradually shields the subauroral region from the high-latitude penetrating electric fields. As the partial ring current grows the shielding effect strengthens, causing the boundary flows between the Region 1 and Region 2 FACs to increase. This leads to enhanced ion temperature and chemical recombination rate, and thus reduced electron density. When the center of the partial ring current drifts westward due to the gradient and curvature drifts, these large boundary flows also move westward from the night side to the day side. When they encounter the SED plume, the plume is segmented into a patch, which later move further into the polar cap. During this process, no IMF variations or transient reconnection are required. The segmentation mechanism is entirely due to magnetospheric internal processes.

CHAPTER III

Mesoscale Enhancement of Subauroral Polarization Stream Associated With an Injection: Multi-instrument Observations

3.1 Introduction

As shown previously, SAPS has the potential to segment the SED plume into a polar cap patch. Thus, it is intriguing to study how SAPS develops, especially the meso-scale SAPS with a shorter life-time, which can be regarded as transient fast flows. In addition, there is a long-lasting debate about during which phase of substorms SAPS occurs. In this chapter, we managed to answer the above questions with a detailed analysis of a SAPS event using multi-instrument observations from VAP, SuperDARN, Geostationary Operational Environmental Satellite (GOES) and SuperMAG. A meso-scale enhancement of SAPS (MS-SAPS+) extending less than 500 km east-west was observed before a substorm onset. An energetic particle injection and a local magnetic field dip in the equatorial magnetosphere were observed simultaneously with the SAPS electric field. The MS-SAPS+ occurred near the nightside Harang reversal, and all the phenomena observed by the above-mentioned instruments can be explained by a non-substorm particle injection and the associated localized pressure enhancement in the equatorial magnetosphere.

3.2 Dataset

This study utilized various observation platform, from the magnetosphere to the ground. Below is a brief introduction of all kinds of measurements.

3.2.1 SuperDARN

SuperDARN is a net work of high-frequency radar which can measure the plasma flow in the mid and high latitude regions. It is an important tool to understand the convection and plasma transport in the upper atmosphere. Currently, there are 38 radars operated both in northern and southern hemisphere. Fig 3.1 shows the coverage of the SuperDARN. These radars can steer their look direction. Each direction is called a beam. Usually, each beam is around 3° wide and each radar has around 16 beams. The field of view (FOV) is around 50° wide. In each beam, there are 75 or 100 range gates and each gate is 45 km long. Each radar can cover an area of 5 to 9 million square km. The time cadence is usually 2 min.

SuperDARN radars can record the signal backscattered from irregularities in the ionosphere which are aligned with the background magnetic field. Further analysis of the backscattered signal yields the backscattered power (signal-to-noise ratio), the line-of-sight (LOS) component of the density irregularity drift velocity and the spectral width of the irregularities (*Clausen et al.*, 2012). Based on a single SuperDARN radar, only LOS velocity is available, i.e. we can only learn how fast the flow drifts towards or away from the radar. With the increasing coverage of the SuperDARN, more regions are in the FOV of two or more Radars. In this case, the 2D drift velocity can be determined. Further more, The drift velocities measured from SuperDARN Radars can be combined into a global map of ionospheric plasma convection using the technique described by *Ruohoniemi and Greenwald* (1998) and *Shepherd and Ruohoniemi* (2000).

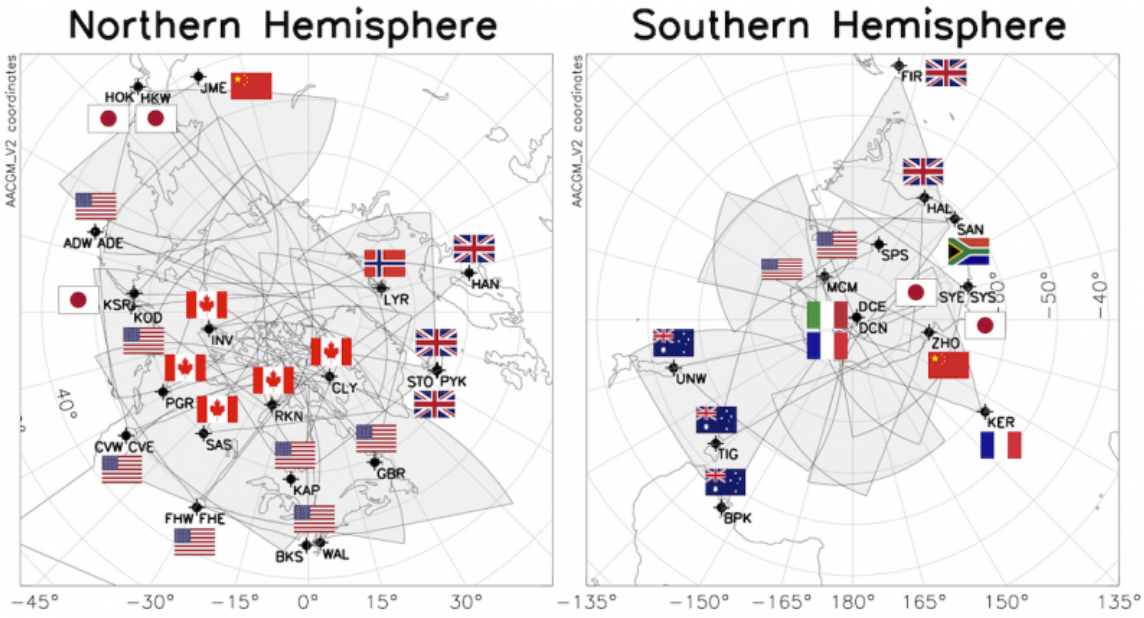

Figure 3.1: A map of the coverage of SuperDARN.

3.2.2 VAP

VAP comprises two identical spacecraft in a highly elliptical, low inclination orbits ($1.1 \times 5.8 R_E, 10°$) in the inner and middle magnetosphere. The orbits are slightly different so that one spacecraft laps the other spacecraft about every 2.5 months, allowing separation of spatial from temporal effects over spatial scales ranging from 0.1 to 5 R_E (*Mauk et al.*, 2014). The instruments onboard VAP can measure the particle (electrons, ions, ion composition), fields (E and B), and wave distributions (dE and dB) and help improve the understanding of how radiation belt particles are generated and lost. In this Chapter, only selected instruments onboard VAP are used: Particle energy spectrum observed by ECT, DC electric field and electron density observed by Electric Field and Waves Instrument (EFW), and DC magnetic field observed by Electric and Magnetic Field Instrument Suite and Integrated Science (EMFISIS). The ECT suite consists of three highly-coordinated instruments: the Magnetic Electron Ion Spectrometer (MagEIS), the Helium Oxygen Proton Electron (HOPE) sensor, and the Relativistic Electron Proton Telescope (REPT) which measure the particle

flux at different energies.

3.2.3 GOES

GOES is in the geosynchronous orbit and carries on board the Space Environment Monitor (SEM) instrument subsystem. The SEM provides magnetometer, energetic particle, and soft X-ray data continuously. In this study, only energetic particle and magnetometer data are used.

GOES Magnetometer provide magnetic field measurements in three mutually perpendicular components: H_P, H_E and H_N. H_P is perpendicular to the satellite's orbital plane. H_E lies parallel to the satellite-Earth center line and points earthward. H_N is perpendicular to both H_P and H_E, and points eastward. GOES Energetic Particle Sensor provides the energetic particle flux in the ring current and outer radiation belt.

3.2.4 AMPERE

AMPERE (*Anderson et al.*, 2014) measures the dynamics of the Birkeland currents using magnetometer data from the attitude control systems of the Iridium telecommunications satellite network. The magnetic field data returned by AMPERE are fit to a continuous spherical harmonic fit and the curl of this fit is used to derive the radial current density with the AMPERE's law. Due to the spacing of the satellites in each orbital plane, data recomposed of a series of 10 min windows, evaluated every 2 min, and the data are on a grid of resolution 1° latitude and 1 hr of MLT.

3.3 Observations

3.3.1 VAP Observations

The SAPS event targeted by this paper was observed by VAP-A on May 18, 2013, as shown in Figure 3.2. The solar wind and IMF conditions during this event were obtained from the NASA OMNI database and shown in Figure 3.2a. The IMF B_z was continuously southward except a short excursion to northward between 0445UT and 0500 UT. This southward AMPERE led to a moderate geomagnetic storm with the minimum SYM-H reaching -66 nT. This SAPS event occurred during the recovery phase of the storm (the shaded blue area), when the IMF turned back to northward briefly and then southward again.

Figure 3.2b presents the DC electric field observed by the EFW instrument in the modified GSE coordinates (MGSE). The MGSE coordinates are similar to the GSE coordinates. On the duskside, the E_y component in the MGSE coordinates was pointing approximately duskward (*Wygant et al.*, 2014). Since VAP-A was on the duskside, we can recognize E_y approximately as the radial electric field. A clear electric field enhancement pointing radially outward can be seen with its peak exceeding 8 mV/m at L=3.5 and MLT=19.8 at 0457 UT (indicated by the blue dashed line). This SAPS electric field observation lasted for only 2 min. It is difficult to identify whether this is a spatial or temporal effect based on a single satellite observation. It can be either a small spatial scale structure or a short-lived one. Another possibility is that the spacecraft crossed the edge of the SAPS region and only captured a fraction of it. Figure 3.2c shows the magnetic field from the EMFISIS fluxgate magnetometer (*Kletzing et al.*, 2014). A local magnetic dip in the GSM B_x and B_z components was encountered by VAP-A at the same time of the SAPS. The electron density derived from the spacecraft potential is shown in Figure 3.2d. As one can see, SAPS was located slightly earthward of the plasmapause, where the cold electron density

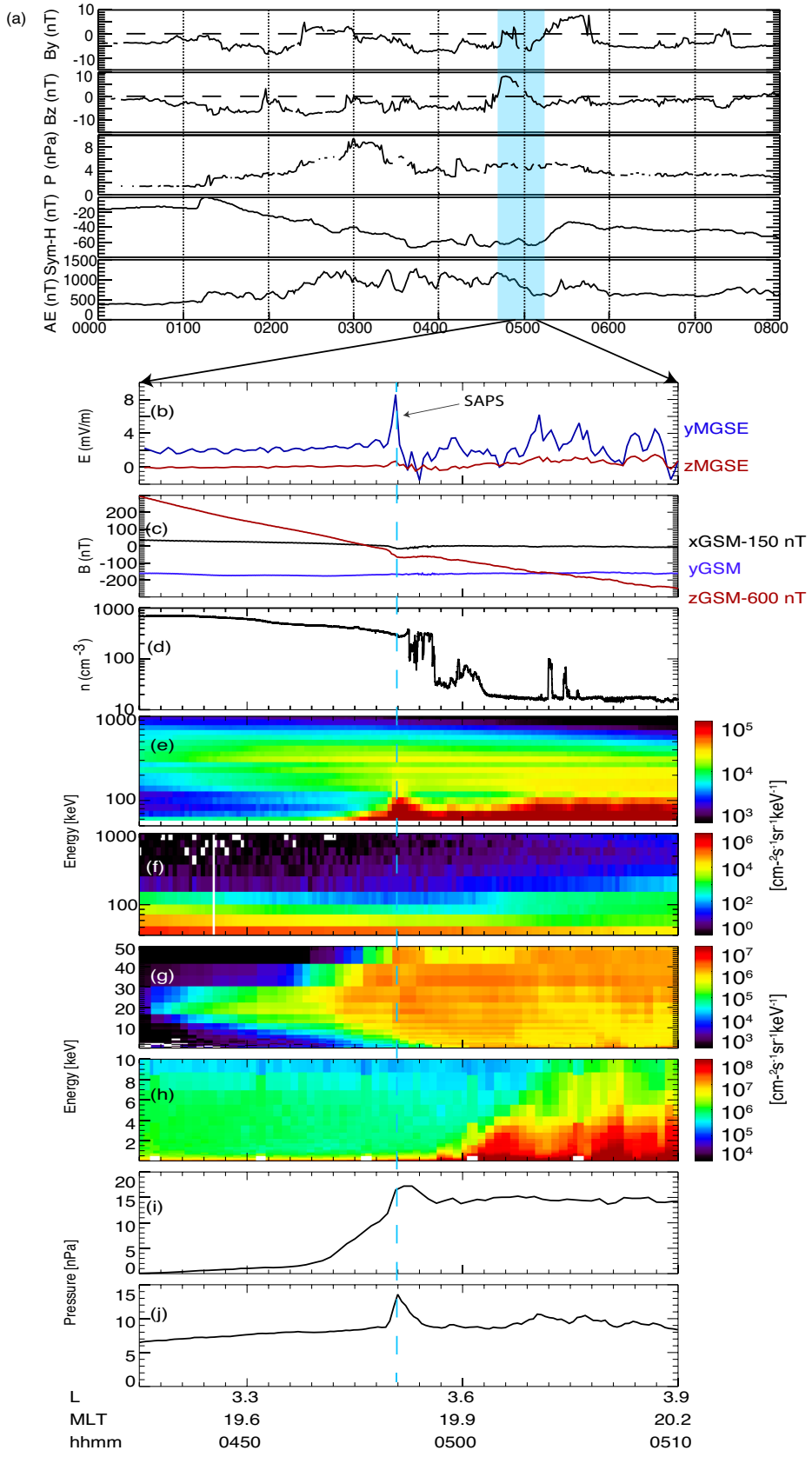

Figure 3.2: Continued on the next page.

Figure 3.2: SAPS event on May 18 2013. (a) Solar wind and geomagnetic data from OMNI. (b) Electric field in the MGSE coordinate from EFW. (c) Magnetic field in GSM coordinate from EMFISIS. (d) Electron density from the spacecraft potential. (e) Differential ion flux from MagEIS with energy between 50 keV and 1 MeV. (f) Differential electron flux from MagEIS with energy between 50 keV and 1 MeV. (g) Differential proton flux from HOPE with energy below 50 keV. (h) Differential electron flux from HOPE with energy below 10 keV. (i) Perpendicular ion pressure from HOPE. (j) Perpendicular ion pressure from MagEIS.

suddenly decreased at 0459 UT.

The high energy (50 keV-1 MeV) spin-averaged ion and electron differential fluxes, shown in Figures 3.2e and 3.2f, respectively, were from the MagEIS instrument (*Blake et al.*, 2014). A clear dispersionless ion injection (50-200 keV) and an electron flux decrease were observed at the same time of SAPS. Note that there were jags between different energy channels in the ion flux. However, the amplitude of the jags was small and well within the measurement uncertainty of MagEIS. Figure 3.2g and 3.2h present the differential flux of proton and electron from 1 eV to 50 keV from HOPE instrument (*Funsten et al.*, 2014). The SAPS electric field was located between the inner boundaries of the ion and electron plasma sheets, which means the SAPS was located in an ionospheric region with low electron precipitation rate. This low electron precipitation rate leads to low conductivity in the ionosphere, and is a preferred condition to facilitate the SAPS development according to the current generator theory. The perpendicular ion pressure in Figure 3.2i and 3.2j were calculated from HOPE and MagEIS, respectively. The pressure from HOPE was calculated using the ion perpendicular temperature and density, while the pressure from MagEIS was calculated using the differential energy flux. Here for simplicity, we assumed that the pitch angle distribution of particles observed by MagEIS was isotropic. *Zhao et al.* (2015) showed that the isotropic assumption would not significantly influence the magnitude of the pressure. In addition, the gradient of pressure rather the absolute value is more important in the FAC generation theory. At this time, the contribution

of electrons to the plasma pressure was much smaller than that of the ions and thus ignored. As one can see, the SAPS electric field was located in the region with a large ion pressure gradient. According to the Vasyliunas equation, this pressure gradient, together with the gradient of flux tube volume, gave rise to the Region-2 downward FACs on the dusk side (*Vasyliunas*, 1970), where the conductivity was low due to low electron precipitation. All of these observations are consistent with the current generator theory. Note that the electron plasma sheet boundary shown in Figure 3.2h is dispersive, which is not expected according to the short circuiting theory (*Mishin*, 2013).

3.3.2 Conjugate SuperDARN Observations

Since observations from one satellite cannot reveal the spatial and temporal variation of the SAPS, it is of vital importance to include the LOS velocity map from SuperDARN in this study. Fortunately, in this event, the footprint of VAP-A was mapped to the west coast of North America, which is well covered by multiple SuperDARN radars. In this study, the LOS velocity observations from the Christmas Valley West (CVW), Christmas Valley East (CVE), Blackstone (BKS) and Wallops Island (WAL) SuperDARN radars between 4 UT and 6 UT were considered. Eight selected snapshots of LOS convection flows are shown in Figures 3.3-3.4. The color represents the direction and magnitude of the LOS velocities with blue representing flows towards the radar and red representing flows away from the radar. Three selected beams, CVW beam 14, CVE beam 0 and 9 are indicated by black dashed lines in the panel of 0448 UT, which will be discussed later. The equatorward boundary of the auroral oval, indicated by the yellow dashed line in Figures 3.3-3.4 is based on the auroral observations centered at 0425 UT from the Special Sensor Ultraviolet Spectrographic Imager (SSUSI) instrument onboard the Defense Meteorological Satellite Program (DMSP) F18. The VAP-A, VAP-B and GOES-15 were mapped to the iono-

sphere based on the Tsyganenko Geomagnetic Field (TS05) model (*Tsyganenko and Sitnov*, 2005) and are shown as purple (VAP-A and B) and green (GOES-15) stars in Figures 3.3-3.4, respectively. Seven ground-based magnetometers close to the west coast are shown as blue crosses. Two orbital planes of the Iridium satellite near the west coast are also indicated as red lines. As one can see, the footprint of VAP-A was located just equatorward of the DMSP SSUSI auroral equatorward boundary, which is consistent with the VAP-A observations shown in Figure 3.2 that the SAPS electric field was earthward of the electron plasma sheet boundary.

As shown in Figure 3.3, at 0420 UT, in the early recovery phase of the storm, a large-scale SAPS (LS-SAPS) had fully developed and extended across the whole North America continent with peak flow speed exceeding 1000 m/s. At 0446 UT, the IMF turned northward and the amplitude of the LS-SAPS decreased to ∼400 m/s. Another feature is that an equatorward flow, highlighted by a black arrow, occurred poleward of the LS-SAPS and near the footprint of GOES-15 with peak flow amplitude of ∼400 m/s. It continued to propagate equatorward at 0448 UT. At 0450 UT, the westward flow near the C13 magnetometer suddenly enhanced to ∼ 600 m/s, while the equatorward flow at higher latitudes disappeared. This SAPS flow enhancement was localized and extended less than 10 degrees in longitude. The eastern part of the LS-SAPS changed little.

In Figure 3.4, at 0456 UT, another equatorward flow developed near a cluster of magnetometers and was highlighted by a black arrow. At 0458 UT, the equatorward flow moved westward to near the footprint of GOES-15 and sustained the enhancement of westward flow. A very rough estimation of the westward movement of the equatorward flow is $2.5°/min$, corresponding an azimuthal velocity of 30 km/s in the GEO orbit. This velocity is comparable with the magnetic drift speed of a 50 keV proton, and is consistent with the energy range of the particle injection observed by VAP-A. At 0500 UT, both the equatorward and westward flows began to decrease

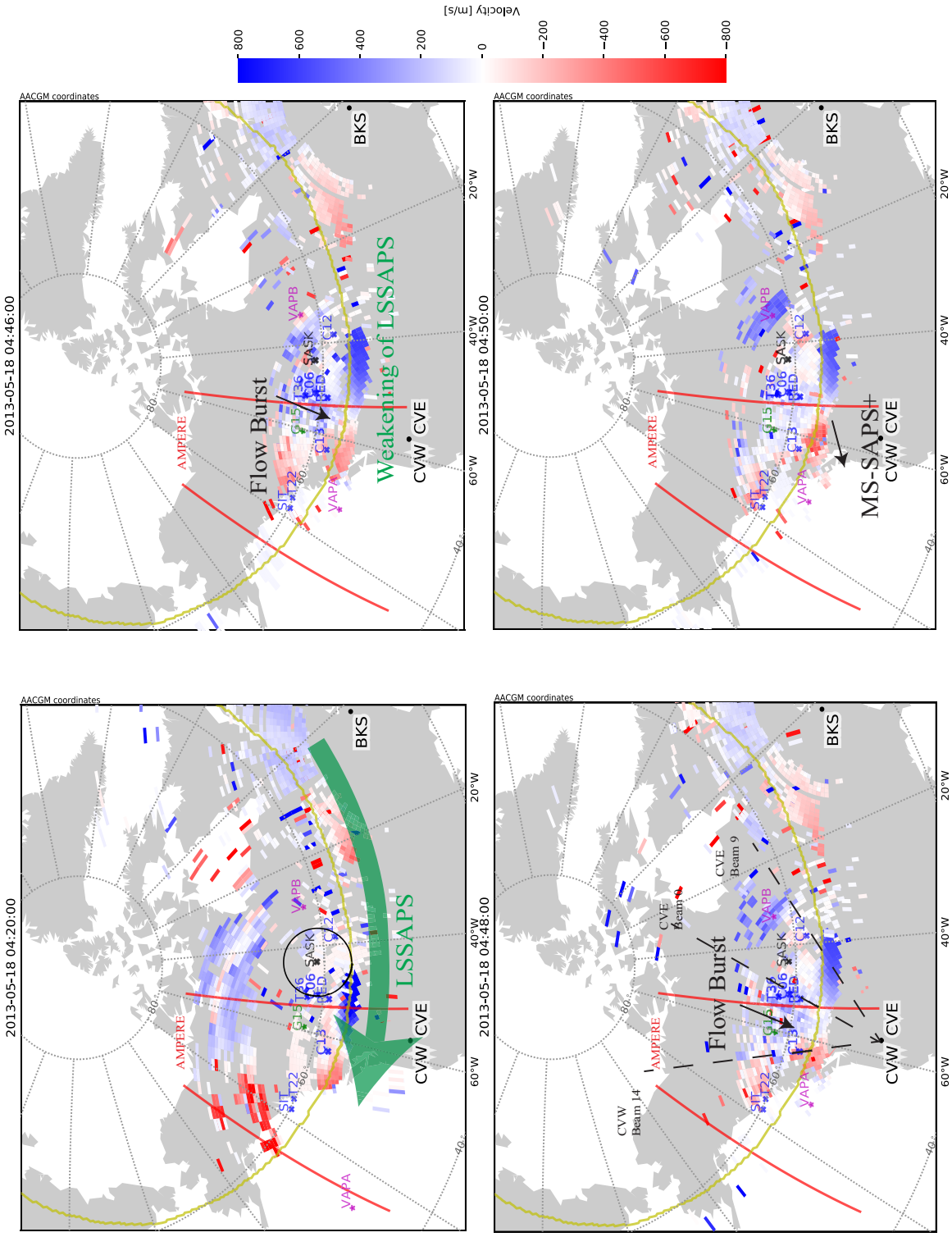

Figure 3.3: Eight selected maps of the SuperDARN LOS velocity in the dusk side with ground-based magnetometers, footprints of VAP and GOES, and orbits of AMPERE. Color represents the velocity relative to the radar. Blue means flows are towards the radar and red means flows are away from the radar.

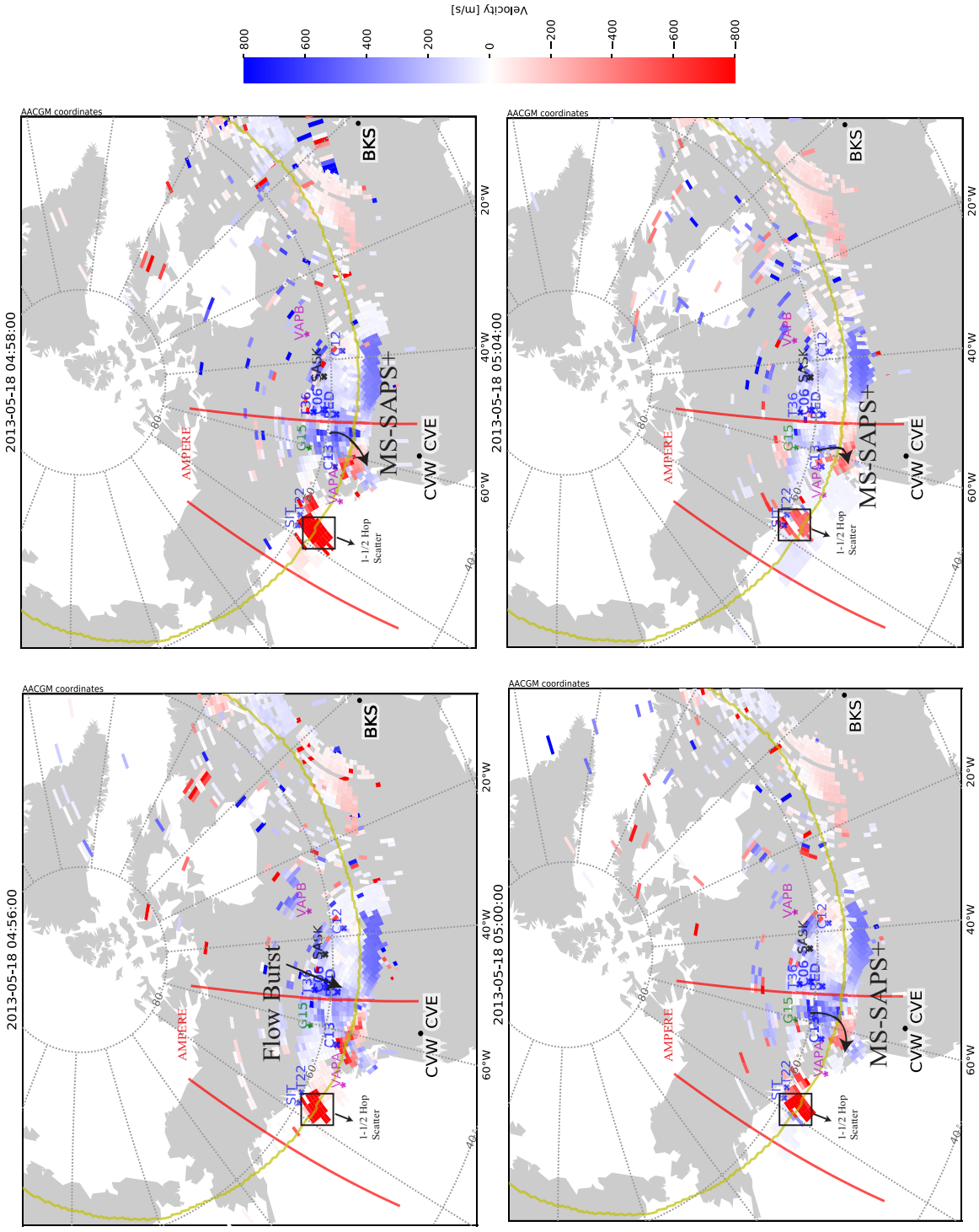

Figure 3.4: Continued Figure 3.3.

and at 0504 UT the flow returned back to the background value. Note that the large westward flow near the magnetometers SIT and T22 were 1-1/2 hop scatter, an artificial signal due to the ground scattering. Combining the VAP-A and SuperDARN observations, it is highly likely that VAP-A passed the western edge of this SAPS enhancement region. Considering the spatial scale of this SAPS enhancement is much smaller than the large-scale background SAPS, which can extend over several hours of MLT, this SAPS enhancement is thus called a MS-SAPS+.

The LOS velocity from CVW beam 14, CVE beam 9 and CVE beam 0 are presented in Figures 3.5 and 3.6. The looking direction of these three beams are indicated by black dashed lines in Figure 3.3. The CVW beam 14 and CVE beam 9 together were used to confirm the localization of this SAPS enhancement. Figure 3.5a shows the LOS velocity measured by the CVW beam 14 as a function of magnetic latitude and universal time, and CVW beam 14 was looking westward. The red color indicates that the flows were moving away from the radar, corresponding to westward flows. As one can see, the westward flow was weak before 0450 UT. There were two sudden enhancements at 0450 and 0455 UT respectively, indicated by green squares, consistent with the two SAPS enhancements following the equatorward flow bursts. Figure 3.5b is in the same format as Figure 3.5a but for CVE beam 9, which is looking eastward. The blue color represents the flow were towards the radar, thus also corresponding to westward flows. The westward flow observed by the CVE beam 9 did not show any enhancement between 0450-0500 UT. Therefore, the comparison between the two beams looking at different sections of the LS-SAPS demonstrated that the enhancement of SAPS was localized. LOS observations from the CVE beam 0 and the keogram from ASI at Saskatoon are shown in Figure 3.6. The keogram is taken at $50°W$. As shown in Figure 3.3, beam 0 is looking approximately poleward. The blue color represents that the flows are moving mainly towards the radar, corresponding to equatorward flows. The field of view of the ASI is also shown in Figure 3.3. One can

see that the CVE Beam 0 was near the western edge of the ASI, and it observed both equatorward flow enhancements at 0446 and 0456 UT, respectively. The timing was consistent with that of the westward enhancements at lower latitude in Figure 3.5a. Although it was cloudy, it can be seen from the keogram that the aurora activity increased simultaneously with the first flow burst. However, no aurora activity was observed within the Saskatoon ASI during the second flow burst. This is very likely because the flow burst was observed by SuperDARN further to the west and thus the corresponding aurora activity is out of the FOV of the ASI.

3.3.3 AMPERE Observations

The orbital plane of AMPERE near 20 MLT is also presented in Figure 3.5a and the black arrows represent the vectors of the magnetic perturbations observed by AMPERE. The vector along the x (y) axis represents the perturbation in the west-east (north-south) direction. The perturbation in the vertical direction is not reflected in Figure 3.5a. It is shown that when the MS-SAPS+ developed, the magnetic perturbations and the downward FACs were both enhanced. The peak of the downward FACs, where the perturbation changed its direction, is denoted by the black circle. Note that the enhancement later at 0510 UT was related to a substorm onset observed by ground-based ASI.

3.3.4 Origin of the Injection

During this event, VAP-B, GOES-13 and GOES-15 were also located in the dusk-midnight sector, which can provide large-scale picture about the particle injection activities. Their orbits from 0415 UT to 0515 UT are shown in Figure 3.7a. Both VAP-A and GOES-15 were at ∼20 MLT, while VAP-B was at ∼22 MLT and GOES-13 was right around midnight. The proton and electron fluxes observed by GOES-15 are shown in Figure 3.7b and 3.7c and the magnetic field in GSM coordinate is

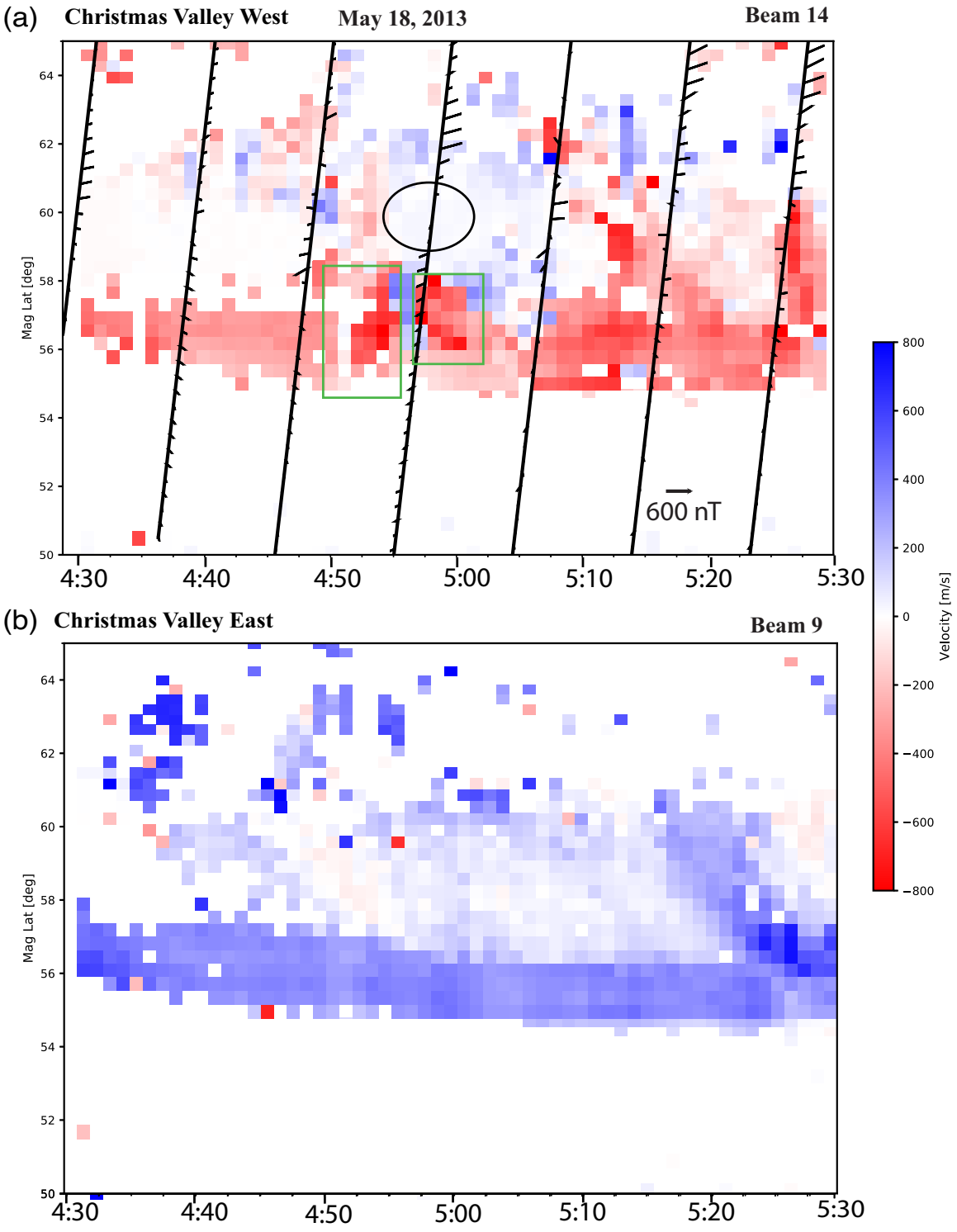

Figure 3.5: (a) Range-time-intensity (velocity) diagram for the CVW beam 14. The red line represents the AMPERE orbital plane in $\sim$ 20 MLT and the black arrow represents the vector of the magnetic perturbations. (b) Range-time-intensity (velocity) diagram for the CVE beam 9.

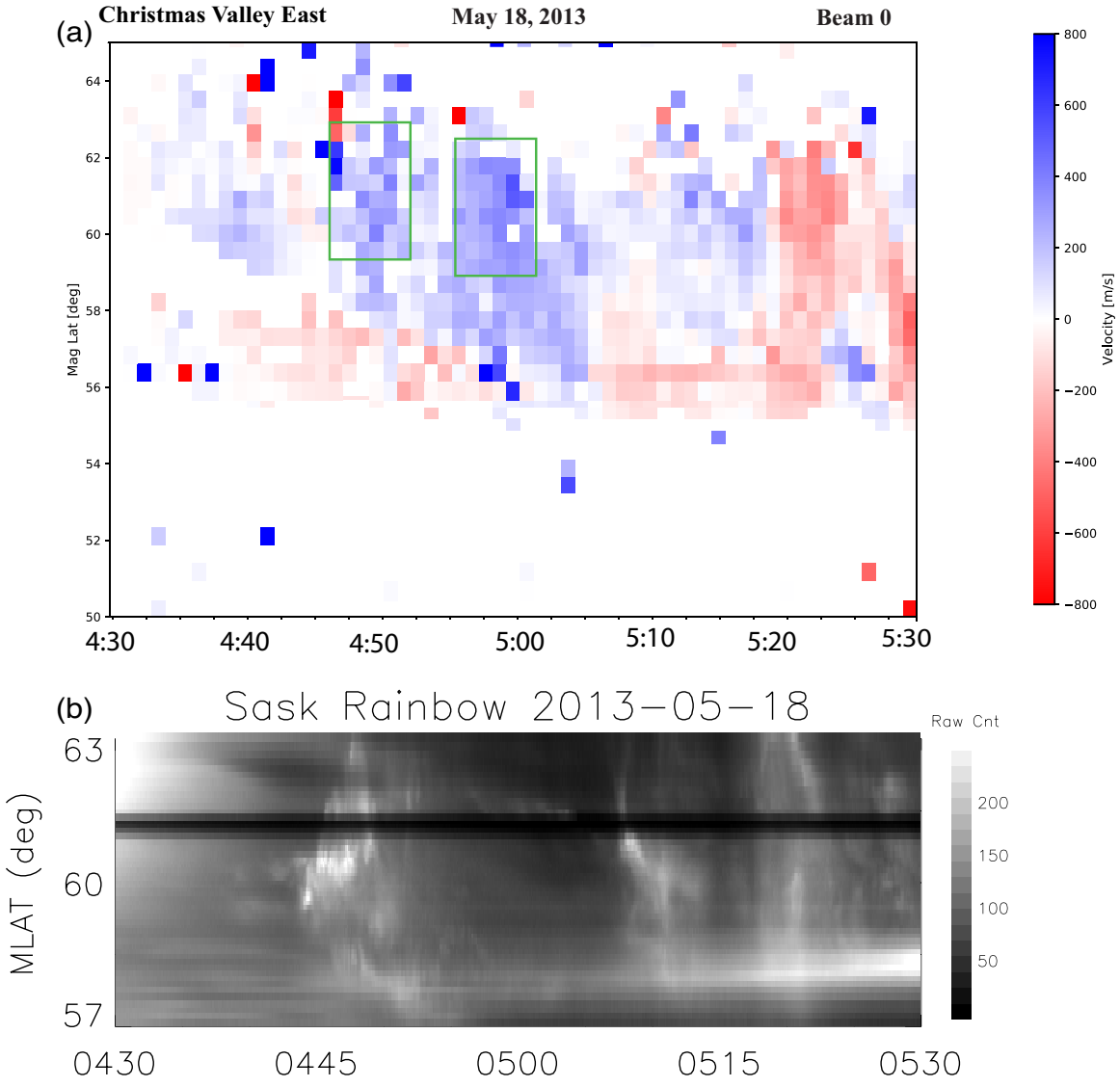

Figure 3.6: (a) Range-time-intensity (velocity) diagram for the CVE beam 0. (b) Keogram fron SASK.

shown in Figure 3.7d. Three injections were observed at 0444 UT, 0450 UT and 0506 UT respectively and are indicated by gray arrows. The timing of the first injection is consistent with the first equatorward flow burst at 0446 UT observed by SuperDARN in Figure 3.3b. Considering the footprint of GOES-15 was very close to the flow channel, both the injection and its manifestation in the ionosphere were thus observed simultaneously. The second injection is likely associated with the SAPS event observed by VAP-A. Considering the conservation of the first adiabatic invariant, the ions of 200 keV energy observed by VAP-A at L= 3.5 should have an initial energy around 30 keV at the geosynchronous orbit. Although this energy is lower than the lowest energy of GOES, i.e., 95 keV, we can use the arrival time of 95 keV ion to roughly estimate the arrival time of 30 keV in the case of dispersionless injection. Both VAP-B and GOES-13 were on the night side during this event, but they did not observe any injections. This suggests that the injection was localized and likely from the dusk side rather than from the night side. The radial injection speed is estimated to be $\sim$47 km/s. The velocity is estimated using the positions of two spacecraft and the time difference between the flux increase observed by these two spacecraft. This calculated injection velocity is reasonable (*Moore et al.*, 1981; *Reeves et al.*, 1996) and suggests that the injections observed by VAP-A and GOES-15 are possibly the same one. The third injection was associated with a substorm onset at 0510 UT observed by ground-based ASI and was after the SAPS event observed by VAP-A.

No magnetic field dipolarization was observed by GOES-15 accompanying the first injection (Figure 3.7d). After the injection was observed by GOES-15, the energetic electrons travelled eastward due to gradient and curvature drift, thus it is not likely to be observed by VAP-A that was westward of GOES-15. The second and the third injections were both accompanied by a magnetic dipolarization. This infers that these injections did not have enough energy to significantly depress the ambient

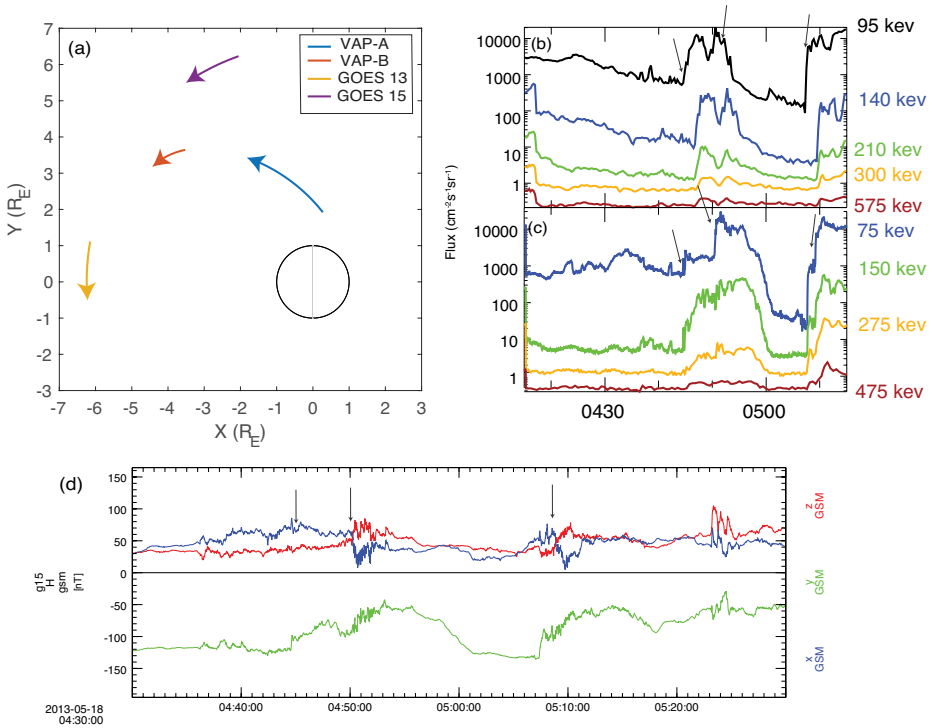

Figure 3.7: (a) VAP and GOES orbits in the xy plane of GSM coordinate. (b) GOES-15 proton flux. (c) GOES-15 electron flux. (d) GOES magnetic field in GSM coordinate.

geomagnetic field at the geosynchronous orbit.

3.3.5 SuperMAG Observations

Seven ground magnetometer data obtained from SuperMAG (*Gjerloev*, 2012) were used to study the magnetic perturbation associated with the SAPS and auroral activities. Daily average was subtracted from the raw data. Their locations relative to the SAPS and auroral boundary are also shown in Figure 3.3. Negative bays were observed by C12, T36, C06, RED at 0450 UT. This time is consistent with the time of the MS-SAPS+ (Figure 3.3). Stations that observed negative bays all located on the east side of the MS-SAPS+. At the same time, positive bays were observed by C13, T22 and SIT, which are close to the MS-SAPS+. Negative (positive) bays are due to enhancement of westward (eastward) auroral currents and thus eastward (westward) convection flows. These observations suggest an overlapping of the westward and eastward currents and flows over a narrow latitudinal region comprises the Harang reversal, which can be nicely explained by the schematic plot shown in Figure 3.9, adapted from Figure 14a in *Zou et al.* (2009b).

In Figure 3.9, the black curved line represents the equipotential line near the Harang reversal region. VAP-A (magenta star) observed the radially outward electric field and its footprint is located in the equatorward portion of the Harang reversal. The beams of CVW looking westward observed westward flows. C13, T22, and SIT observed positive magnetic perturbations, due to eastward auroral electrojet and westward convection flows. On the other hand, at the poleward portion of the Harang reversal, negative magnetic perturbations were observed by C12, T36, C06, RED, and equatorward flows were observed by beams looking poleward.

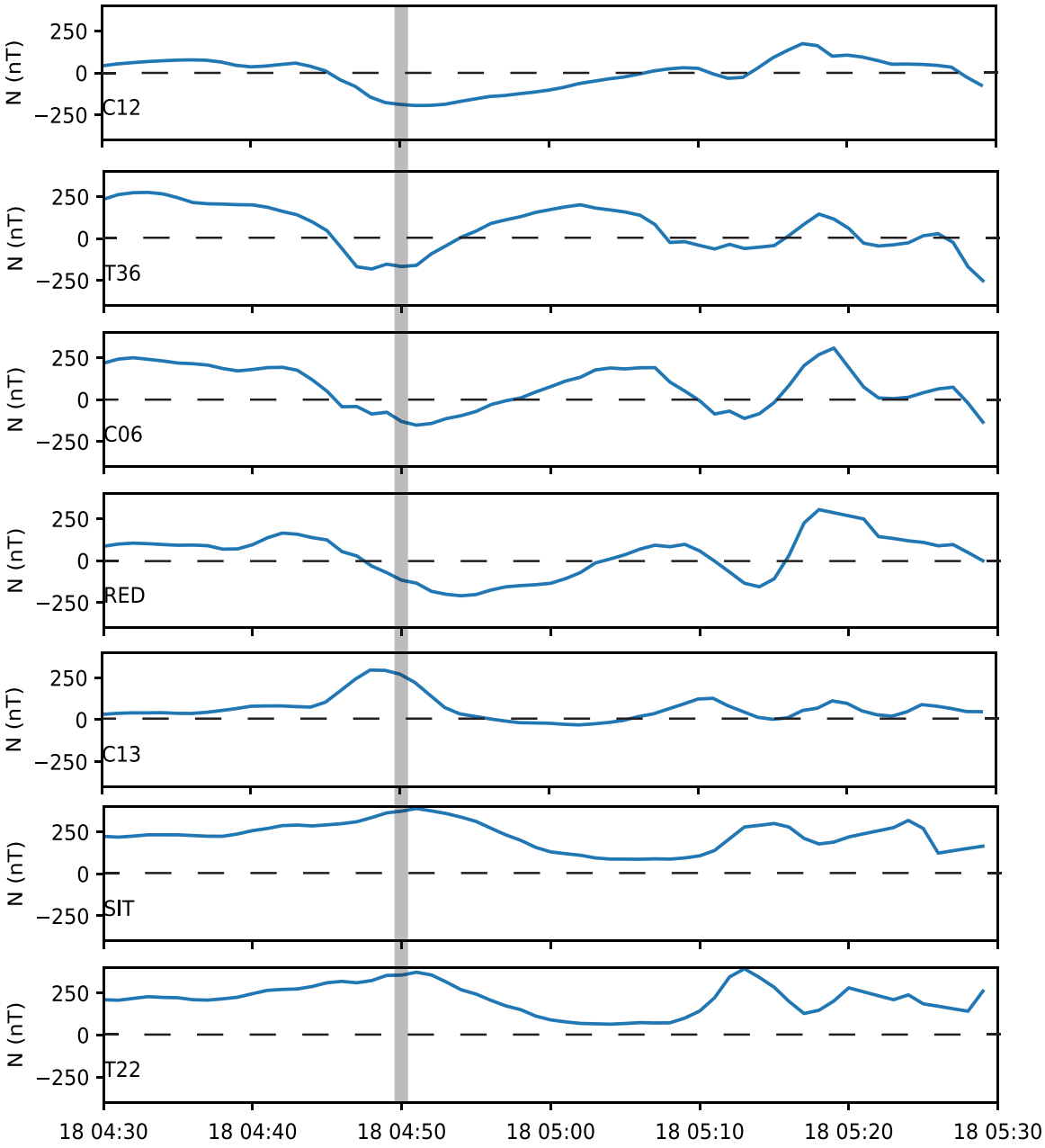

Figure 3.8: Northward components of the terrestrial magnetic field measured by the ground-based magnetometer stations (taken from SuperMAG).

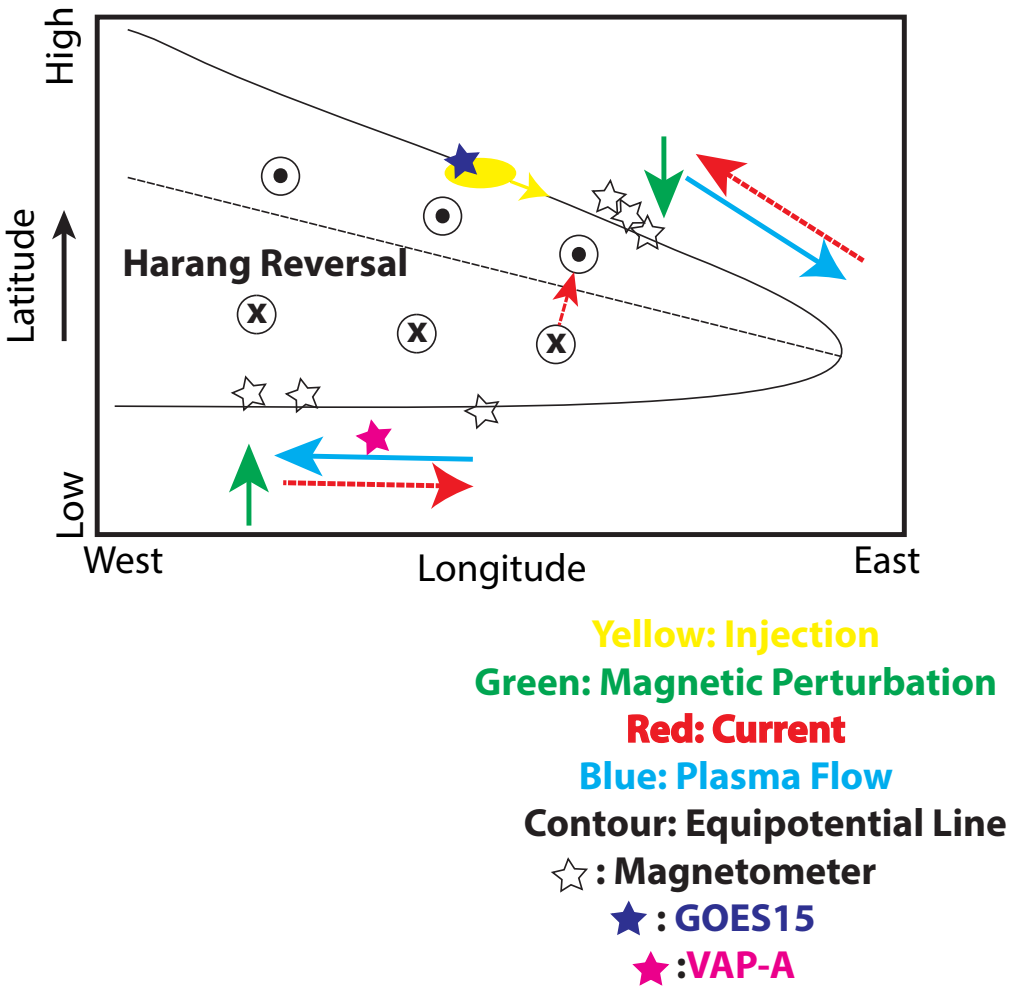

Figure 3.9: A schematic diagram of the convection flows, field-aligned currents and magnetic perturbations near the Harang reversal.

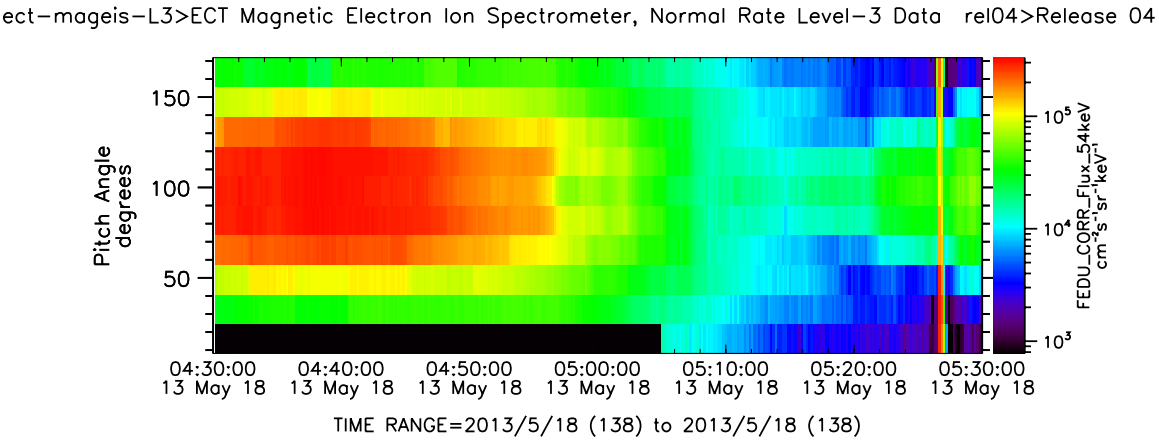

Figure 3.10: (a) Pitch Angle Distribution of electrons at 54 keV observed by MagEIS between 0430 and 0530 UT.

3.4 Discussions

The SAPS electric field and other complementary measurements from VAP-A presented in Figure 3.2 are consistent with the current generator theory. At first, when the injected particles traveled towards the inner magnetosphere, they were adiabatically energized in order to conserve the first adiabatic invariant. At the geosynchronous orbit, they may not have enough energy to depress the magnetic field. As they moved closer to the plasmapause, these particles were energized enough and could depress the magnetic field according to the diamagnetic effect (*Gurgiolo et al.*, 1979; *He et al.*, 2017b; *Xia et al.*, 2017; *Xiong et al.*, 2017). The magnetic dip in the inner magnetosphere is important for both the generation of butterfly pitch angle distributions (PADs) of electrons (*Xiong et al.*, 2017) and electromagnetic ion cyclotron (EMIC) wave (*He et al.*, 2017b; *Remya et al.*, 2018). The magnetic field dip led to the decreasing of the energetic electron flux (Figure 3.2e) due to conservation of the first adiabatic invariant of electrons, consistent with earlier observations (*He et al.*, 2017b). In this case, butterfly pitch angle distributions (PADs) were also observed by VAP-A at the energy of 54 keV (Figure 3.10).

We further tested the diamagnetic properties in the SAPS region. We first used

the TS05 magnetic field magnitude minus 48 nT to fit the general trend of magnetic field ignoring the magnetic dip. Then this magnetic field was compared with the observed magnetic field, which shows that the magnetic pressure decreased by ∼17 nPa at the center of magnetic dip and SAPS peak. The increase of the ion plasma pressure was about 12 nPa with contributions from both HOPE and MagEIS ($\Delta P_{HOPE} + \Delta P_{MagEIS} = 7 + 5$ nPa). This was quantitatively similar to the magnetic pressure decrease. Therefore, the magnetic field dip can be explained by the particle injections and their diamagnetic effects. This also shows that the injected particles can make a large contribution to the storm time ring current, as shown in (*Gkioulidou et al.*, 2014). Another interesting point is that this injection was observed to enter the inner magnetosphere at $\sim$ 20 MLT, and no injection was observed closer to the midnight sector. Therefore, this injection might be related with dynamics near the magnetopause flank, such as Kelvin-Helmholtz instability (*Henderson*, 2013). However, the exact source of the particle injection is out of the scope of this chapter.

When a plasma pressure peak was generated in the inner magnetosphere, together with the gradient of the flux tube volume, a pair of Region-2 sense FACs can be generated near the edges of this dip (Figure 3.11), according to the Vasyliunas equation. In addition, this region was between the inner boundaries of ion and electron plasma sheets, and thus the region where the downward FACs flowed into in the ionosphere was of low conductivity. When the downward FACs closed poleward through the Pederson currents and the upward Region-1 sense FACs, the electric field needed to increase to maintain current continuity. The above scenario explains the large poleward electric field in the ionosphere and radially outward electric field in the magnetosphere.

The results above lead to the schematic diagram of the formation of SAPS given in Figure 3.11. During geomagnetic storm time, a partial ring current develops due to the enhanced convection. The gradient of plasma thermal pressure in partial ring

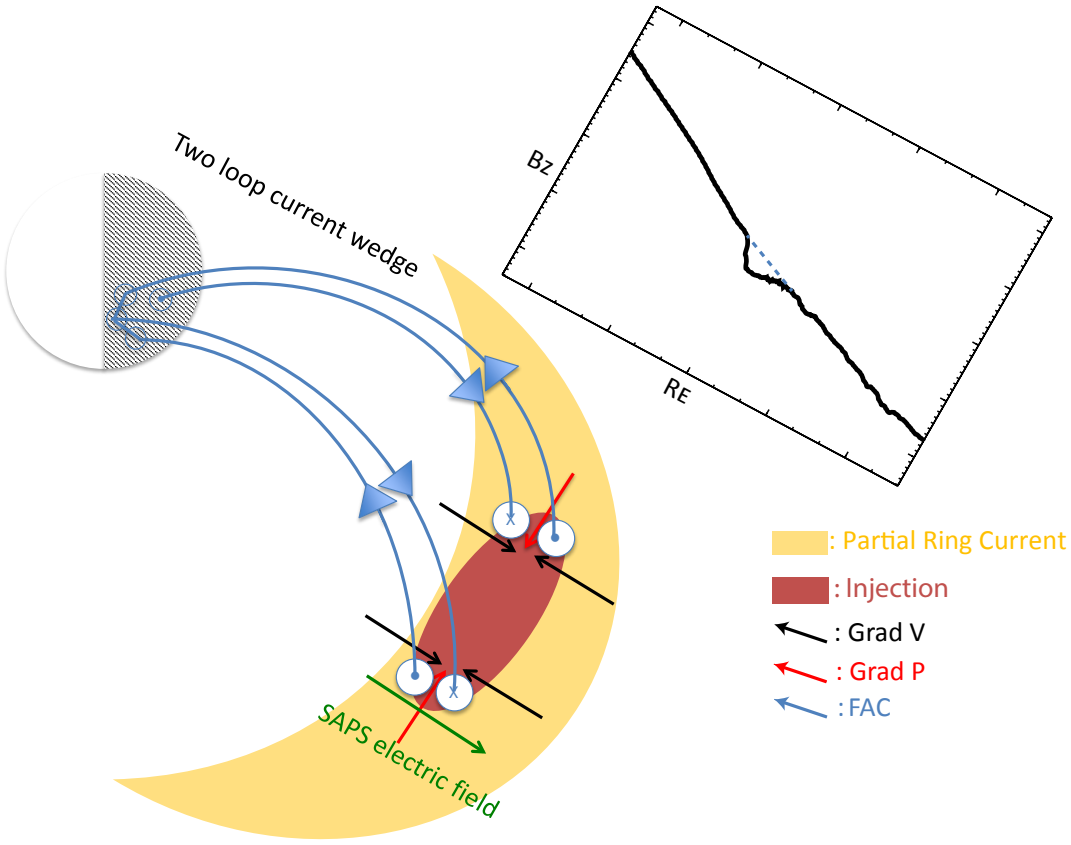

Figure 3.11: A schematic diagram of the formation of 2LCW and SAPS in the inner magnetosphere.

current and the gradient of the flux tube volume can generate the Region-2 FACs and thus SAPS (*Anderson et al.*, 1993; *Southwood and Wolf*, 1978). This LS-SAPS should have a spatial scale comparable with the partial ring current and can extend several hours of MLT. However, when a localized injection entering the inner magnetosphere and merging into the pre-existing partial ring current, a localized pressure peak should form. At the same time, due to the diamagnetic effect, a local magnetic field dip can develop at the same location. The gradient of the flux tube volume points towards the local magnetic minimum. Therefore, the perturbed plasma pressure gradient and the flux tube volume gradient give rise to two pairs of FACs. The duskside pair is the Region-2 sense downward FACs close to the Earth and Region-1 sense upward FACs further away from the Earth. The other pair closer to midnight would have opposite polarity. These two pairs of FACs thus comprise a two-loop current wedge (2LCW). In duskside ionosphere, the Region-2 sense FACs close through poleward Pederson current and then upward Region-1 sense FACs. This Pederson current flows in a low-conductivity region equatorward of the electron precipitation boundary and thus leads to a large poleward electric field, i.e., SAPS electric field. Meanwhile, these FAC pairs superpose on top of the large-scale FAC systems near the equatorward edge of the aurora oval. This 2LCW can also explain the magnetic dip in the MGSE x direction. At the dusk side, the MGSE B_x component can be considered westward. Both the downward FACs earthward of the dip and upward FACs further away from the dip can generate an eastward magnetic disturbance and thus reduce the B_x component in the MGSE coordinates. Note that this 2LCW should be differentiated against the 2L SCW. The latter is formed after substorm onset although the formed FACs have similar polarities. In addition, no local magnetic field dip is invoked in the 2L SCW scenario. This mechanism can also be applied to LS-SAPS: The spatial scale of the SAPS depends on the scale of the particle injection. Injections can have variable scales from less than 1 hour in MLT, e.g. in this event, to three hours in MLT in

substorm injections, to the whole night side during sawtooth-type injections (*Arnoldy and Moore*, 1983; *Clauer et al.*, 2006; *McPherron*, 2015). Thus, the scale-size of the SAPS enhancement should be directly related to the scale-size of injections.

Auroral streamers in the ionosphere have been proposed to be the corresponding signature of flow bursts in the equatorial magnetosphere or injections when flow bursts reach the geosynchronous orbit (*Forsyth et al.*, 2008; *Henderson et al.*, 1998; *Nakamura et al.*, 2001; *Sergeev et al.*, 1999; *Zou et al.*, 2009a,b). *Gallardo-Lacourt et al.* (2017) showed that 98% streamers reaching equatorward boundary of the auroral oval are associated with SAPS and there is a strong correlation between the duration of SAPS and streamers. *Nishimura et al.* (2011) showed that not all streamers can lead to substorm onset. Thus, it is reasonable to infer that substorm onset is not necessary for streamers or particle injections, and thus SAPS. Enhanced auroral activity was indeed observed during the first equatorward flow and SAPS enhancement, but it was not observed during the second case. This is very likely because the flow burst was observed by SuperDARN beams looking west of the ASI, and thus the corresponding aurora activity is out of the FOV of the ASI.

Dispersionless particle injections are often observed during substorms right at or slightly after the substorm onset and have been used as a reliable substorm onset indicator. However, injections and substorms do not have a one-to-one correspondence (e.g. *Angelopoulos et al.*, 1992; *Gkioulidou et al.*, 2014). *Sergeev et al.* (1990) showed that injections can occur during steady convection time in addition to substorm time. This also suggests that substorm onset may not be necessary for injections and thus the formation of SAPS. Instead, SAPS can be generated directly by particle injections.

3.5 Summary and Conclusions

In this chapter, we performed a detailed case study of SAPS during the storm recovery phase on May 18, 2013 using conjugate VAP and SuperDARN as well as other complementary instruments. Energetic ion injections, energetic electron flux decrease, and local magnetic field dip were observed at the same time as the SAPS electric field by VAP-A deep in the inner magnetosphere at 3.5 Re. The formation mechanism of the SAPS is suggested to be due to energetic particle injection together with the magnetic field distortion due to the injected particles' diamagnetic effect, which can generate a localized 2LCW with SAPS on its western side. SAPS is also shown to be part of the equatorward boundary of the Harang reversal, which starts to develop before the substorm onset. Considering the correspondence between substorms and injections is not one-to-one, we suggest that SAPS can be generated directly due to particle injections induced pressure and flux tube volume gradients, no matter whether these injections are directly related with a substorm onset or not.

CHAPTER IV

Hemispheric Asymmetries in the Midlatitude Ionosphere: Multi-Instrument Observations

4.1 Introduction

In this chapter, ionospheric responses were examined during the double-dip storm on Sep 7-8, 2017. During the first recovery phase, hemispheric asymmetries were found in VTEC. The asymmetries are observed simultaneously in the dawn and afternoon sectors and have opposite polarities. In the asymmetric regions, the EDP from four digisondes were selected to provide further details of the electron altitude distributions. The detrended VTEC, plasma drift from digisondes, and the $[O]/[N_2]$ from Global Ultraviolet Imager (GUVI) onboard the Thermosphere Ionosphere Mesosphere Energetics and Dynamics (TIMED) satellite were also utilized to study the possible drivers of the asymmetry. Based on our analysis, we suggest that a combination of the asymmetries in the neutral composition change, vertical drift and TID activity generated the hemispheric asymmetries in VTEC and F-region ionosphere density.

4.2 Data and Analysis Technique

Multi-instrument datasets were analyzed in this study and described below:

4.2.1 Digisonde

Digisonde is a digital ionosonde, which uses high frequency radio waves for the vertical-incidence remote sounding of the ionosphere. In this study, several products from the selected digisondes were utilized, including EDPs, plasma drifts, the peak height (hmF2) and peak density of the F region (NmF2). They are described in detail below.

4.2.1.1 EDP

Digisonde ionogram presents signals reflected from the ionosphere in the frequency vs travel time frame. Radio waves from the ionosonde with frequencies lower than the local ionospheric critical frequency will be reflected below the peak of the F region, while those with frequencies higher than the critical frequency will not be reflected back. Therefore, ionosondes can detect the bottomside EDP but cannot provide the topside EDP. Here, with the assumption that the topside ionosphere follows the Chapman function, we use the typical Chapman extrapolation to complete the EDP (*Huang and Reinisch*, 1996).

4.2.1.2 Plasma Drift

Digisonde measures the plasma drift based on the echoes reflected by undulated density contours and irregularities (*Reinisch et al.*, 1998). *Scali et al.* (1995) showed that there is a good agreement between the drift measured by digisonde and ISR at high latitude region. *Bullett* (1994) showed that the digisonde drift technique works best during moderately disturbed nighttime conditions. Note that the drift measured by digisondes might not be reliable when the production and recombination are rapid, e.g. near the terminators (*Gonzales et al.*, 1982; *Woodman et al.*, 2006). There can be artificial downward/upward drift due to the generation/disappearance of E-layer due to sunrise/sunset. Those artifacts have been carefully avoided in this study.

4.2.2 Tomography

The ionospheric tomography technique is a powerful tool to reconstruct the 3D structure of the ionospheric electron density. It is a typical inversion problem used to estimate the electron density based on the integrated slant TEC (sTEC) along the line-of-sight of GNSS satellites and receivers. In this case, 340 ground-based dual-frequency GNSS receivers, provided by the EUREF Permanent Network (EPN), were used to calculate the GNSS sTEC and 2D regional VTEC maps, while there are not dense enough receivers in other sectors to apply the tomography technique. Based on the GNSS sTEC results over the European sector, the state-of-the-art tomography technique (*Yao et al.*, 2020) is applied to resolve the spatial distribution of the electron density. The inversion region is over 35°N-65°N and 5°W-20°E with the horizontal resolution of 1° in both latitude and longitude. The altitude range of the tomography is from 100 km to 1000 km with varying vertical resolutions, and the resolutions for altitudes below and above 450 km are 10 km and 50 km, respectively. To reconstruct the 3D electron density at time t, the ground-based GNSS sTEC from t-20 minutes to t+20 minutes are used, i.e., 40 minutes GNSS data are used to invert the tomography results at time t. The electron densities from the International Reference Ionosphere (IRI)-2016 model are used as the initial values for the inversion.

4.2.3 $[O]/[N_2]$

The column density ratio $[O]/[N_2]$ is derived based on the ratio of 135.6 nm and LBHS emissions measured by GUVI on board the TIMED satellite (*Strickland et al.*, 1995, 1999, 2004; *Zhang et al.*, 2004). It is a useful parameter to reflect the thermosphere impact on ionospheric density production and loss. Note that GUVI cannot provide a snapshot of the global thermosphere composition distribution at a given time, instead it needs one day to cover all longitudes. The TIMED satellite was orbiting the 10.7 LT and 22.7 LT plane during this storm.

4.3 Observations

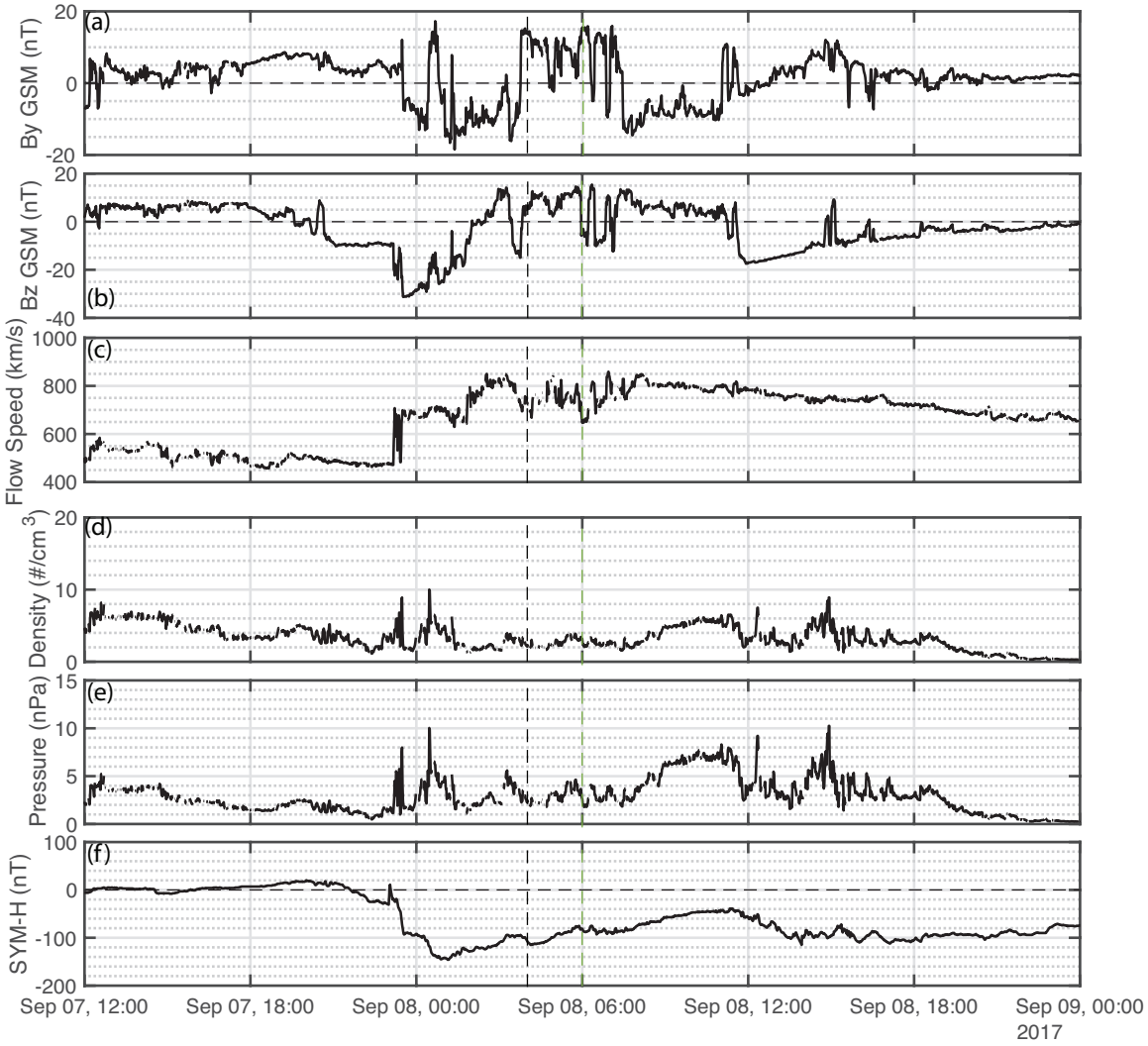

Figure 4.1: Solar wind data and geomagnetic index from 12 UT Sep 7 to 0 UT Sep 9, 2017. (a) IMF B_y in the GSM coordinates, (b) IMF B_z in the GSM coordinates, (c) solar wind speed, (d) proton number density, (e) solar wind dynamic pressure, and (f) the SYM-H index. The black and green vertical lines represent the period that we will focus on latter.

4.3.1 Solar Wind Condition

Figures 4.1a-4.1f show the B_y and B_z components of the IMF in GSM coordinates (IMF B_y and B_z), solar wind speed, proton number density, dynamic pressure, and the SYM-H index during the September 7-8 2017 storm. A general description of this

double-dip geomagnetic storm on September 7-8 2017 has been provided previously. In this chapter, we focus on the first recovery phase (from 0230 UT to 1105 UT). During this period, the IMF B_z reversed its direction several times, but during most of the times, IMF was northward. The first recovery phase ceased due to the arrival of another ICME at $\sim$ 1105 UT, which led to the second main phase. The magnetic cloud signature of the second ICME was clearly indicated by the gradual rotation seen in the IMF B_y and B_z.

4.3.2 VTEC observations

The storm-time alterations of the VTEC (dVTEC) from the quite-time values at 04 and 06 UT on September 8 are shown in Figure 4.2 in the geographic coordinates. The quiet-time VTEC on September 7, 2017, was removed from the storm-time values. The magnetic field lines in the quasi-dipole coordinates at 300 km are plotted on top of the dVTEC map as thin solid lines. The thicker gray line represents the geomagnetic equator. Four digisondes used in this study are also denoted by black stars on the map. At 04 UT, the IMF B_z component turned northward, and the SYM-H was gradually recovering. The large-scale ionosphere response began to transit from the positive phase to the negative phase, but the dVTEC was almost hemispherically symmetric. In the East Asian and Australian sector, there were VTEC increases (over 20 TECU) in both hemispheres, which were caused by the widened equatorial ionization anomaly (EIA). In the European and African sector, only minor VTEC increases ($\sim$ 5 TECU) were observed in both hemispheres.

Between 04 UT and 06 UT, the IMF remained northward, and the SYM-H recovered to $\sim$ -80 nT. During this period, strong hemispheric asymmetries developed in both the European-African (LT$\sim$5-7) and the East Asian-Australian sectors (LT$\sim$12-16). At 06 UT, these asymmetries became very obvious and they are highlighted by black arrows in Figure 4.2. Based on the dVTEC movie, these asymmetries developed

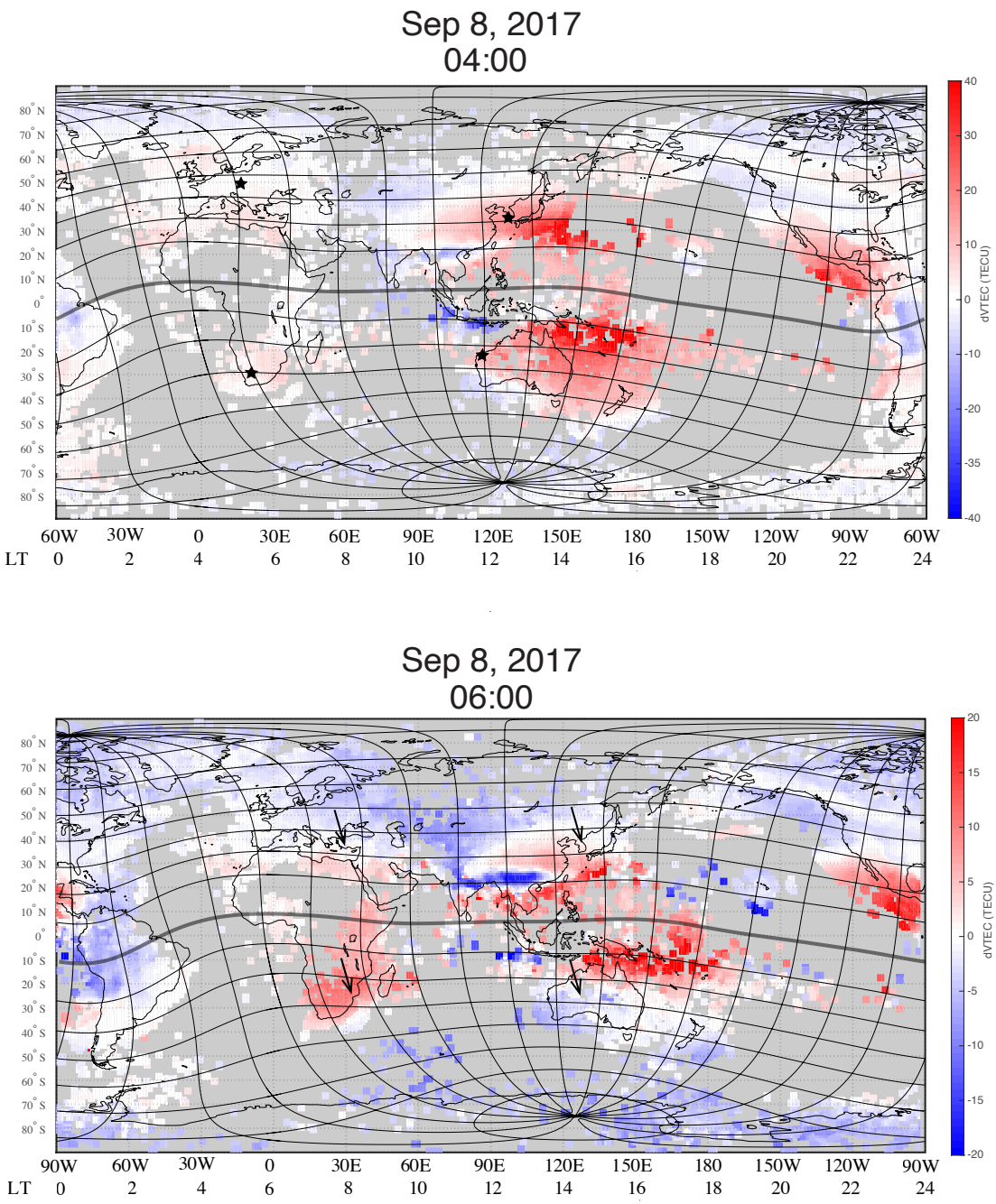

Figure 4.2: VTEC differences between Sep 8, 2017 and Sep 7 2017. The difference is shown in geographic coordinate with a map of Quasi-Dipole coordinates at 300 km altitude. The asymmetry was highlighted by the black arrows. Four digisondes were represented by stars.

when the ionosphere transited from the positive phase to the negative phase. In the European-African sector, in the mid-latitude region ($20° \sim 40°$ MLAT), the VTEC

increased in the southern hemisphere, but decreased in the northern hemisphere. The size of the asymmetry was about 15° in longitude and 10° in latitude. This asymmetry was also studied in (*Habarulema et al.*, 2020). On the contrary, in the East Asian-Australian sector around 120° E longitude, the VTEC increased in the northern mid-latitude region (20° ∼ 30° MLAT), while decreased in the conjugate southern hemisphere. The size of the asymmetry was larger than the European-Africa sector, which was almost 20° in longitude and 20° in latitude.

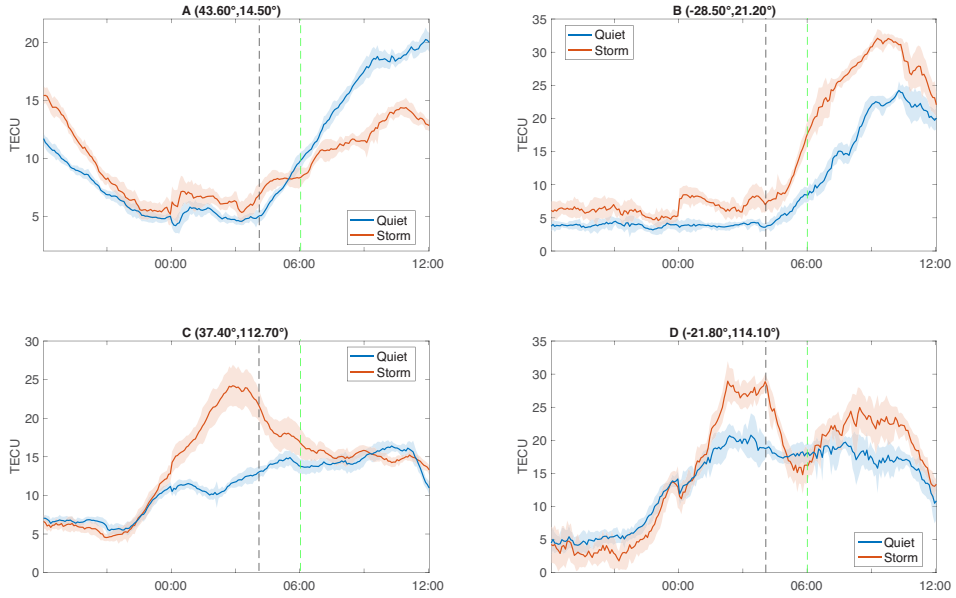

Figure 4.3: Time series of the VTEC from four locations. The black and green lines represent 04 UT and 06 UT on Sep 8, respectively. The blue and red lines represent, respectively, the quiet time and storm time values, while the shaded region represents the standard deviation.

The time series of the VTEC at four selected locations (labeled as A, B, C, and D), where the asymmetries were observed, are shown in Figure 4.3. The locations of these four points in the geographic and geomagnetic coordinates are shown in Table 4.1. The VTEC at each location was the averaged value over a surrounding region of $5°longitude \times 5°latitude$ to better reflect the regional VTEC changes. The standard deviation of the VTEC values in each surrounding region is plotted as the

shaded area together with the averaged values. In the southern hemisphere, Louisvale (B) and Learmonth (D), where digisondes are available, were chosen. Then their geomagnetic conjugate points (A, C) were calculated and selected. Before the shock arrival, the VTECs at the locations A and B were slightly larger than the quiet-time values. During the main phase of the storm, the European-African sector was on the nightside and the ionospheric responses to the initial energy input were small with a couple of TECU increase. A large asymmetry began to develop in this sector after 04 UT (sunrise). The VTEC at the location A gradually increased due to sunrise. However, the increasing rate was lower than the quiet-time value, resulting in a lower VTEC, i.e., entering the negative phase. On the contrary, the VTEC at the location B increased with a larger rate than the quiet-time value, and the dVTEC was always positive with its maximum of 10 TECU at around 10 UT on September 8. Therefore, these two conjugate points in the European-African sector entered the negative and positive phases, respectively, at the same time.

Table 4.1: Geomagnetic conjugate locations and the nearest digisondes

Location	A	B	C	D
Geographic Latitude	43.6°	−28.5°	37.4°	−21.8°
Geographic Longitude	14.5°	21.2°	112.7°	114.1°
Geomagnetic Latitude	38.0°	−38.0°	32.0°	−32.0°
Nearest Digisonde	Pruhonice	Louisvale	I-Cheon	Learmonth
Geographic Latitude	50.0°	−28.5°	37.1°	−21.8°
Geographic Longitude	14.6°	21.2°	127.5°	114.1°
Geomagnetic Latitude	45.0°	−38.0°	31.0°	−32.0°

The VTEC at the location C in the East Asian sector and at the location D in the Australian sector began to increase at around 00 UT on September 8, shortly after the shock and strong southward IMF arrival at the Earth. These increases ceased when the IMF turned northward at around 0230 UT. Later, the VTECs at these two locations started to decrease, but with different speed. The hemispheric asymmetry in VTEC began to develop after 04 UT. The VTEC at the location C gradually decreased and recovered to the quiet-time value at around 08 UT. When the VTEC

asymmetry was observed at 06 UT , the location C was still in the positive phase. On the other hand, the VTEC at the location D decreased rapidly and became lower than the quiet-time value at around 05 UT, i.e., entering the negative storm phase. However, this negative storm phase was a short-lived one. The VTEC started to recover and exceeded the quiet-time value after 07 UT. Therefore, these two conjugate locations in the East Asian-Australian sector were in the positive and negative phases, respectively. However, the polarity of this asymmetry is opposite to the one observed in the European-African sector.

4.3.3 EDP observations

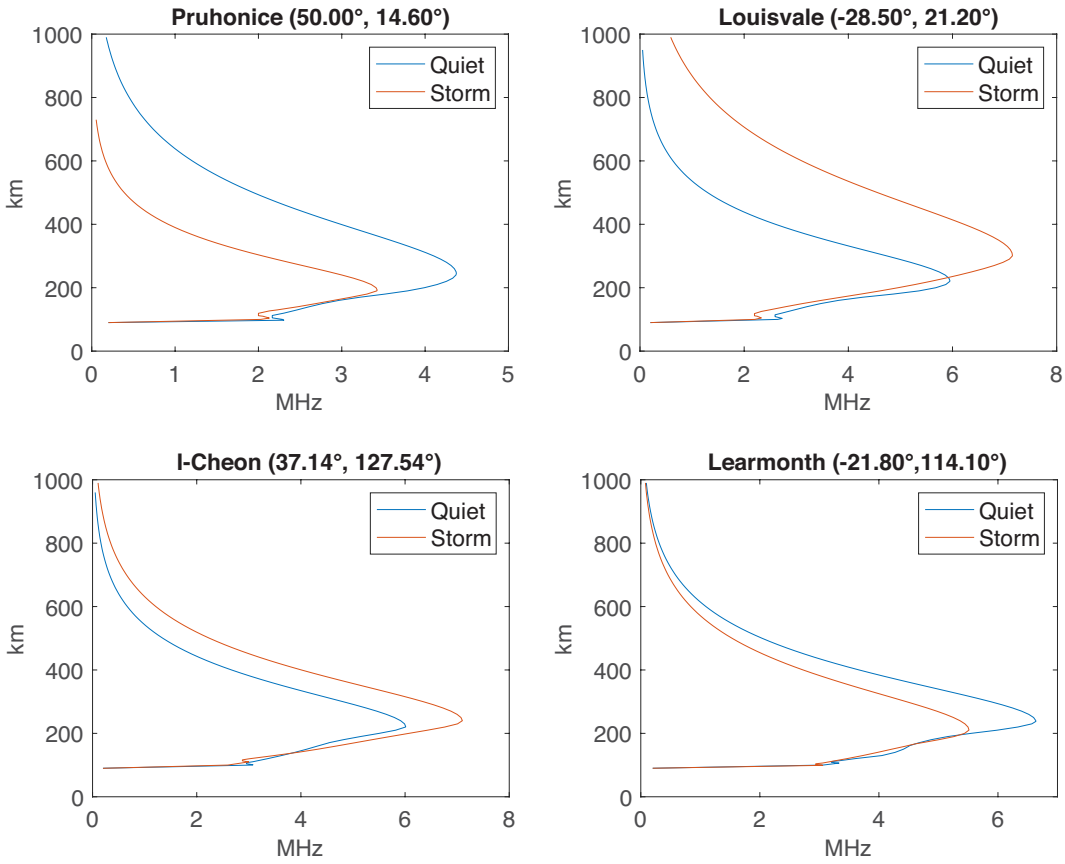

Figure 4.4: EDP from the four selected digisondes in Figure 4.2 at 06 UT Sep 8, 2017. The red curve represents the storm-time (Sep 8) value, while the blue curve represents the the quiet-time (Sep 7) value.

The four digisondes closest to the four points are selected to provide the EDPs (Figure 4.4), which help further confirm the existence of the asymmetries at 06 UT. Their locations are also shown in Table 4.1. Clear asymmetries can be observed in the EDP plots at 06 UT and are consistent with the VTEC observations in Figure 4.2: At Pruhonice (the closest digisonde to A), the electron density decreased significantly in the F region and the topside ionosphere, while at Louisvale (B), the electron density increased significantly above 250 km, in particular at the the F-region peak height. At I-Cheon (the closest digisonde to C), the electron density increased in the whole F region, while at the conjugate Learmonth (D), the electron density decreased in the F region, i.e., opposite to the trend observed in the European-African sector. In the mean time, the hmF2 at Louisvale (B) and I-Cheon (C) increased comparing with that during quiet time, while dereased at Pruhonice (A) and Learmonth (D). Therefore, the VTEC and EDP observations shown in Figures 4.2-4.4 clearly demonstrated that hemispheric asymmetries developed during the first recovery phase and were opposite in the East Asian-Australian (N+S-) and European-African (N-S+) sectors. Here N/S indicates the northern/southern hemisphere and +/- indicates positive/negative phase, respectively.

4.4 Discussions

In the mass continuity equation of the ionospheric plasma, the change of the electron density within a certain magnetic flux tube can be due to the vertical plasma drift and the chemical production/loss (*Kelley*, 2009). The electric field, neutral wind, and ambipolar diffusion along the magnetic field lines can all contribute to the vertical movement of the plasma, and their influences depend on the magnetic field inclination and declination angles (*Schunk and Nagy*, 2009). The vertical drift can transport the plasma to lower or higher altitudes where the neutral density is higher or lower, and thus affect the plasma lifetime by changing the charge exchange and

recombination rates. The upward drift can transport the plasma to higher altitudes, where the charge exchange and recombination rates are lower. Thus, the density at the new F region peak height and topside ionosphere can be larger than that before lifting (*Heelis et al.*, 2009; *Zou et al.*, 2014). If the plasma production is active, the VTEC can increase as well. The thermospheric composition change, on the other hand, can alter the production and loss rates. When the atomic oxygen density ($[O]$) increases in the sunlit region, the production rate will increase, while the increase of the molecular species density (e.g. $[N_2]$) will lead to an enhanced loss rate. Thus, the $[O]/[N_2]$ ratio is a key parameter that can be used to infer the thermosphric composition impact on the TEC (*Kil et al.*, 2011; *Mannucci et al.*, 2009; *Strickland et al.*, 2001; *Yue et al.*, 2016; *Biqiang Zhao et al.*, 2009). In this section, both the plasma drift and the $[O]/[N_2]$ data are used to study the generation mechanisms of the asymmetries in each sector.

4.4.1 European and African Sector

The plasma drift measurements from the digisonde at Pruhonice (A) between 18 UT on September 7 and 12 UT on September 8 are shown in Figure 4.5. The drifts in the magnetic north, magnetic east and vertical directions are shown in Figures 4.5a-4.5c. *Schlesier and Buonsanto* (1999); *Zou et al.* (2013, 2014) separated the contributions to the vertical drift from the electric field, neutral wind, and ambipolar diffusion based on the observations from ISRs. The plasma drift perpendicular to the magnetic field line is due to the electric field, while the drift along the magnetic field line can be attributed to the neutral wind and/or the ambipolar diffusion. A similar method is applied to the digisonde drift measurements in this study. Since the electron and ion temperatures are not available at the locations of these digisondes, the contributions from the neutral wind and the ambipolar diffusion cannot be further separated. In numerical simulations, the contribution from the ambipolar diffusion

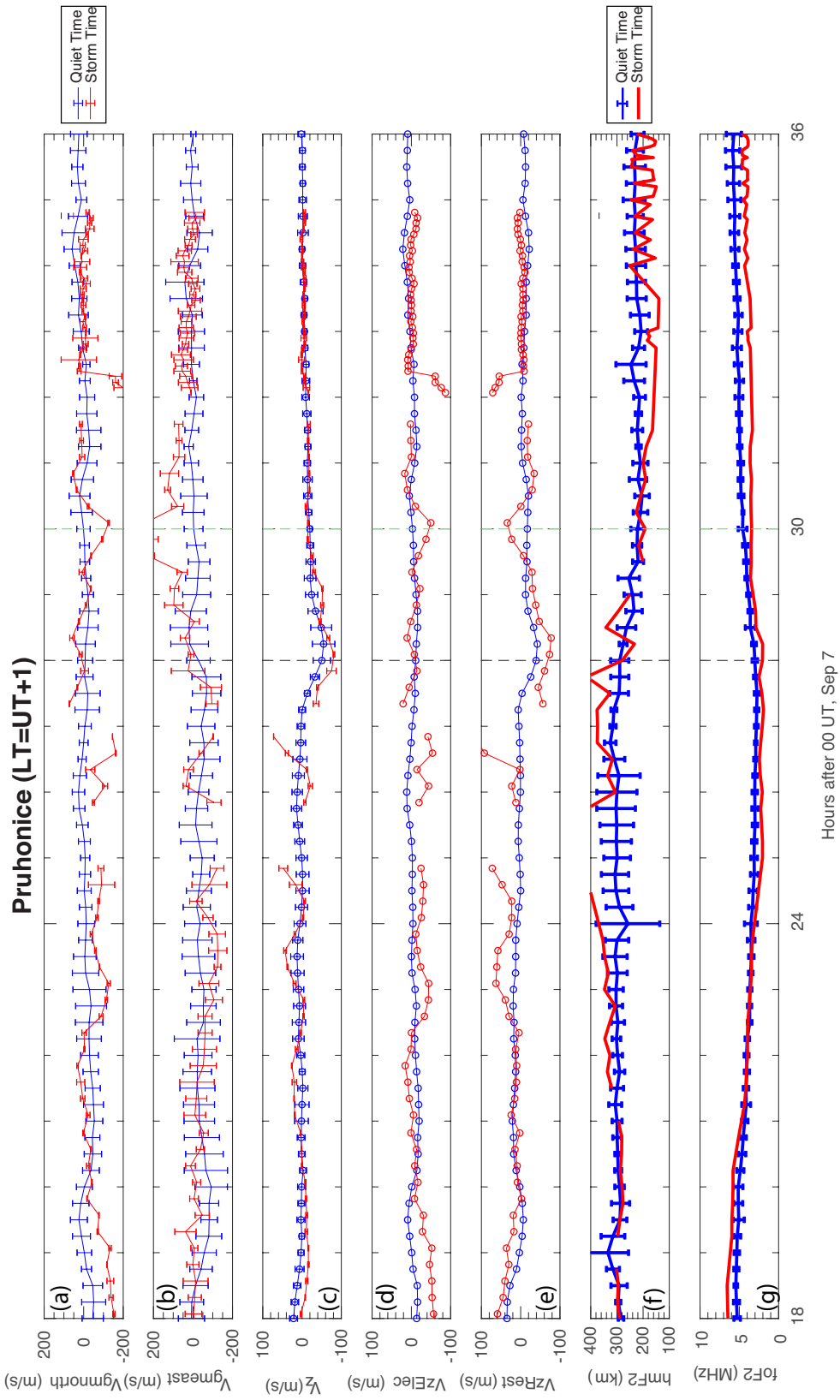

Figure 4.5: Continued on the following page.

Figure 4.5: Drift data from the digisonde at Pruhonice.(a) Drift in the geomagnetic north direction. (b) Drift in the geomagnetic east direction. (c) Drift in the vertical direction. (d) Vertical drift due to the electric field. (e) Vertical drift due to the neutral wind and diffusion along the magnetic field line. (f) hmF2. (g) foF2. The black and green lines represent 04 UT and 06 UT, respectively. The red curve represents the storm time (Sep 7-8) value, while the blue curve represents the the quiet time (the average of the previous week) value. The error bars of the quiet-time values indicate the quiet-time variability, while the error bars of the storm-time values represent the uncertainty of the measurements.

is usually much smaller than that from the neutral wind (*Lu et al.*, 2012; *Zou and Ridley*, 2016; *Liu et al.*, 2016). The vertical drift due to the electric field is shown in Figure 4.5d. The rest of the vertical drift (Figure 4.5e) is due to the combined effect of neutral wind and diffusion along the magnetic field line. Note that this separation is not applicable near the terminator because of the artificial drift of the digisonde observation. Figures 4.5f and 4.5g show the hmF2 and foF2 measured by digisondes. The red curves represent the storm-time values during September 7-8 and the blue curves represent the averaged quiet-time values in the previous week. The error bars of the quiet-time values indicate the quiet-time variability, while the error bars of the storm-time values represent the uncertainty of the measurements. The plasma drifts at the other three locations are shown in Figures 4.6, 4.10, 4.11 in the same format.

The European and African sector was on the nightside during the main phase. Despite sporadic data gaps, the digisonde observations at Pruhonice (A) showed wave-like structures in the vertical drift in Figure 4.5c. The wave-like structure significantly departed from the quiet-time trend and was likely signatures of TIDs. While at Louisvale, the vertical drift oscillated around the quiet-time trend with a much smaller amplitude. To further confirm the possible TID signatures and compare their amplitudes in different hemispheres, the keogram of the detrended VTEC over the European-African sector (10° - 20° E longitude) from 00 to 06 UT is shown in Figure 4.7. The detrended VTEC was calculated by subtracting the moving average of the VTEC from the raw VTEC. The sampling window used in this study is 30 min.

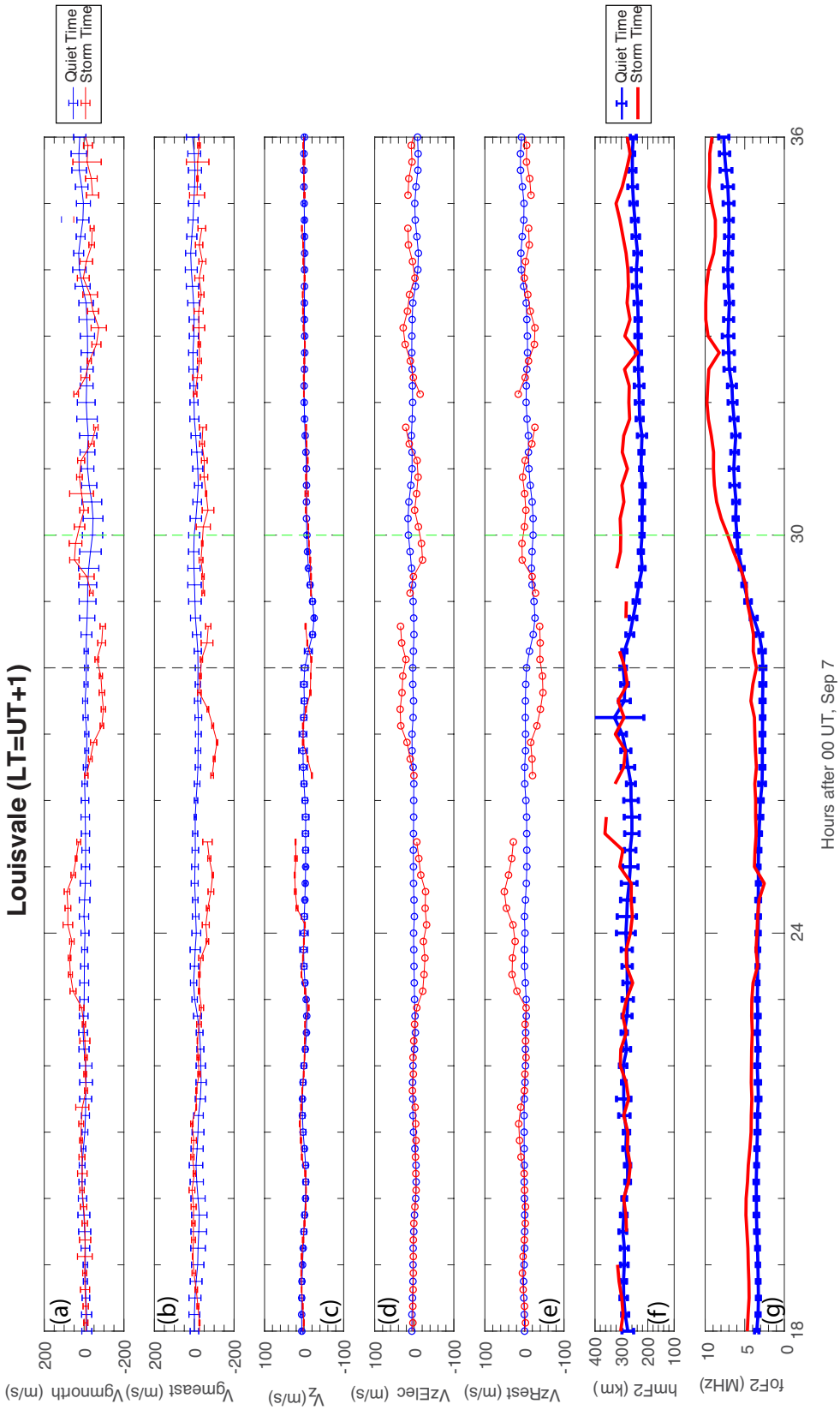

Figure 4.6: Drift data from the digisonde at Louisvale. The format is the same as Figure 4.5.

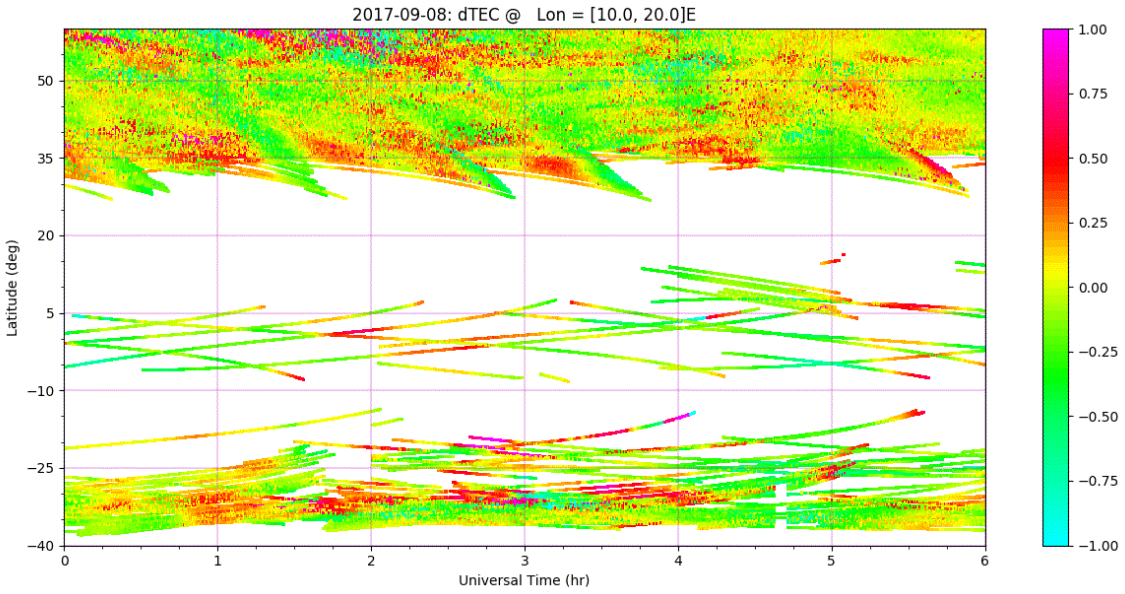

Figure 4.7: Keogram of detrended VTEC for European-African sector.

In the northern hemisphere, there were continuous TIDs propagating from the high-latitude region to the low-latitude region. However, there was limited coverage of the GNSS receivers in the southern hemisphere. Although there were fluctuations in the detrended VTEC in the southern hemisphere, it is hard to compare the amplitude of TIDs in the southern hemisphere with that in the northern hemisphere.

To further evaluate the impact of TIDs in the northern hemisphere, the tomographic inversion results are shown in Figure 4.8. The left panel shows the electron density profile at 20° E as a function of latitude and altitude. The poleward boundary of the remnant of the EIA extended to around 48° N. Two electron density islands were located at 55° N and 62° N, respectively. The peaks of these islands were at around 310 km. These two electron islands are likely signatures of the TIDs propagating from the auroral region to the low-latitude region. The right panel shows the electron density profile at 300 km as a function of longitude and latitude. It shows the impact of TIDs on the electron density from a different view point. Due to the low temporal resolution of the tomographic inversion technique, the propagation of the TID cannot be revealed by this technique. However, the tomographic inversion

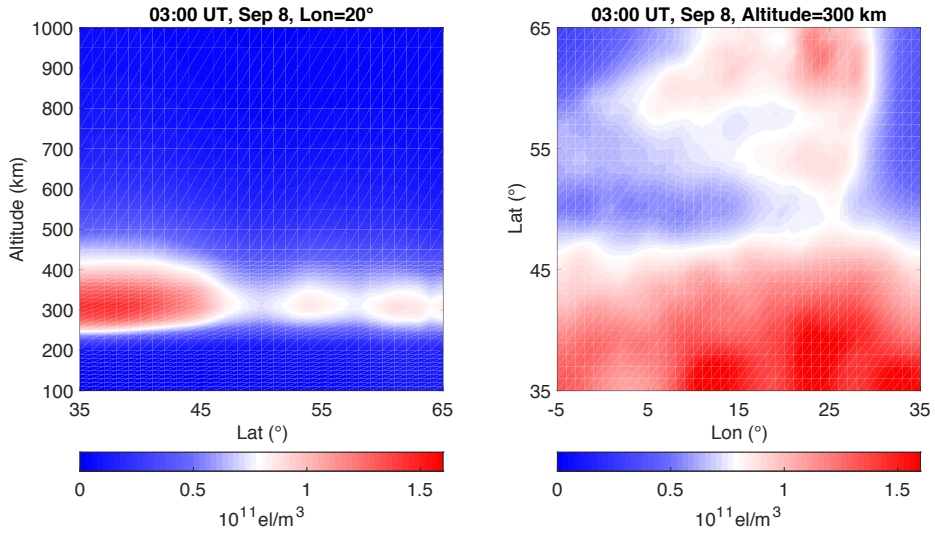

Figure 4.8: 3D tomography results at 0300 UT, September 8. Left panel: Electron profile at 20° E as a function of latitude and altitude. Right panel: Electron profile at 300 km as a function of longitude and latitude.

results, the wave structures observed in the drift data, and the detrended VTEC together strongly suggest the existence of equatorward propagating TIDs in Europe. On the other hand, the TIDs in Africa were less evident due to the limited observations. Based on the drift observation alone, it is likely that the TIDs were weaker in the southern hemisphere in this case. The magnitude of TIDs was larger in the hemisphere where the negative phase occurred later, which suggests there might be a larger energy deposition at the auroral latitudes in the corresponding hemisphere. The hemispheric asymmetry of TIDs observed a couple of hours ahead may signal the development of the asymmetries of VTEC and electron density later during the recovery phase.

As shown in Figures 4.5d-4.5e, during the main phase, the electric field at Pruhonice tended to move the plasma downward after the IMF southward turning, while the combined neutral wind and diffusion tended to move the plasma upward and contributed more to the wave-like fluctuations. The net result was that the plasma moved upward, i.e., the hmF2 slightly increased, and thus the VTEC increased as well (Figure 4.2 and 4.3). At Louisvale, Figure 4.6 presented a similar trend in the drift, but with a much smaller amplitude. The hmF2 at Louisvale was close to the quiet-time value during this period, with an exception of an hour-long hmF2 increase at about 02 UT. The electric field that led to the plasma descending was likely the penetration electric field on the nightside, while the equatorward meridional winds due to the enhanced heating in the auroral region pushed the plasma along the field line.

The recovery phase of this storm initiated at 0230 UT after the IMF northward turning. In the European sector, at Pruhonice (A) and Louisvale (B), the asymmetry in the vertical drift developed during the early recovery phase. At Pruhonice, there was an enhanced downward movement between 03 and 05 UT, while the drift at Louisvale was always close to the quiet-time value during the recovery phase. The

downward drift at Pruhonice would move the plasma to lower altitudes with a higher recombination rate, and thus the electron density and VTEC would decrease. The continuous decrease of the hmF2 confirms the expected impact of the downward movement of the ionosphere at Pruhonice. Therefore, the stronger downward drift observed at Pruhonice than that at Louisvale led to the lower VTEC and negative phase as shown in Fig 4.2, i.e., the asymmetry of the plasma drift contributed to the asymmetry of the VTEC.

After sunrise (LT = UT+1 at Pruhonice and Louisvale), due to the solar production, the foF2 at Pruhonice (Figure 4.5g) started to increase. However, the foF2 was always lower than the quiet-time value and the discrepancy continued to increase, which is consistent with the negative phase shown in the VTEC data in Figure 4.2. On the other hand, the foF2 at Louisvale (Figure 4.6g) increased faster than the quiet-time value after sunrise. Considering it was close to sunrise, chemical production process may also play a role in the formation of the asymmetry. Therefore, the column-integrated $[O]/[N_2]$ ratio data were also studied to evaluate this possibility.

The column-integrated $[O]/[N_2]$ ratio on September 7, September 8 from the TIMED GUVI instrument, and their difference are shown in Figure 4.9 to provide the storm-time thermospheric composition change. The orbits of the satellite are plotted on top of the $[O]/[N_2]$ ratio color contours, and the universal times labeled above the top horizontal axis represent when the satellite passed $60°N$. The TIMED satellite flew over the European-African sector at 0930 UT, and a clear hemispheric asymmetry in the $[O]/[N_2]$ ratio was observed. The southern edge of Africa was in the region of enhanced $[O]/[N_2]$, while the conjugate Europe was in the region of reduced $[O]/[N_2]$. Note that the VTEC asymmetry occurred at around 0600 UT and lasted until the initiation of the second main phase (Figure 4.3). Thus, although the composition asymmetry over the European and African sector was measured by GUVI at 0930 UT, it is likely that this asymmetry had already fully developed at 06 UT. As

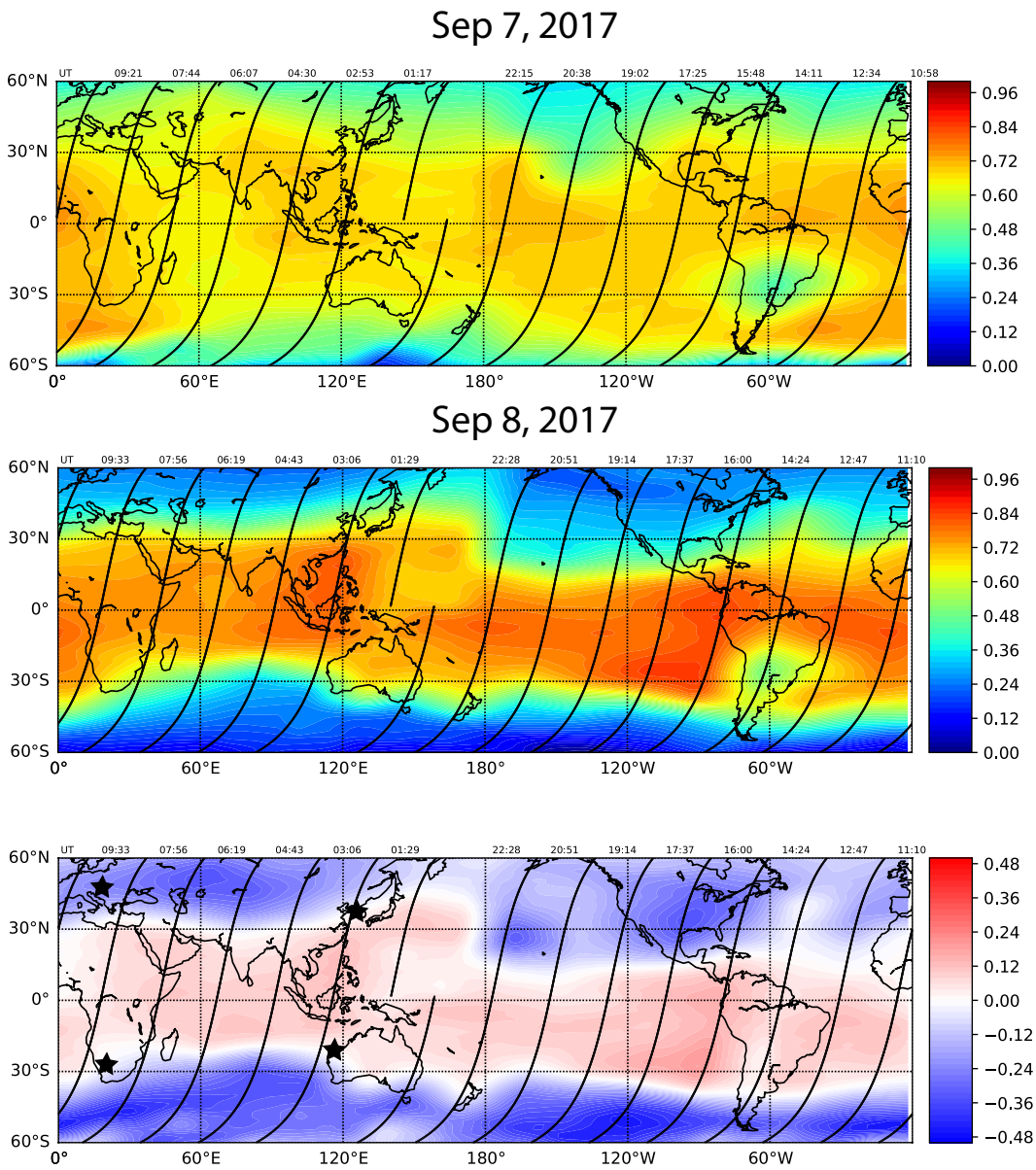

Figure 4.9: $[O]/[N_2]$ from TIMED GUVI on Sep 7, Sep 8 and the difference. The orbits of TIMED are plotted on top of the map. The time represents when the satellite cross $60°N$. The satellite is at 10.7/22.7 LT.

shown in Figure 4.9, on September 7, the $[O]/[N_2]$ ratio was larger in the southern hemisphere due to the seasonal effect. Then, the storm further enhanced the expected seasonal asymmetry, consistent with earlier studies (*Duncan*, 1969; *Mendillo*, 2006).

The effect of the composition change was unmasked by the solar radiation after sunrise. Before sunrise, the molecular species mattered most in the loss process, and no production process existed. However, after sunrise, the production initiated, and the $[O]/[N_2]$ ratio largely determined the electron density and TEC. Besides the TID and vertical drift discussed earlier, we suggest that the difference in the thermospheric chemical composition also contributed to the asymmetry seen both in VTEC and digisonde measurements in the European and African sector.

4.4.2 East Asian and Australian Sector

During the main phase of this storm, I-Cheon (C) and Learmonth (D) were on the dayside. The equatorial plasma fountain effect amplified on the dayside and led to the widened EIA. A VTEC increase (Figure 4.2 and 4.3) was observed in the low-latitude region. I-Cheon and Learmonth were located near the poleward part of the widened EIA. There was no increase of the vertical drift observed at both I-Cheon and Learmonth in Figure 4.10-4.11 when the shock and strong southward IMF arrived, suggesting that the penetration electric field effect was weak at these two locations. Then, the vertical drift at I-Cheon still followed the quiet-time trend except a short drift increase around 1 UT (there were some intermittent data gaps). At the same time, both the foF2 and hmF2 increased and these enhancements were signatures of the widened EIA. At Learmonth, the vertical drift trend was also similar to the quiet-time curve except two local minimums around 01 and 02 UT, respectively. Before 02 UT, the increases of foF2 and hmF2 were also related to the widened EIA. After 02 UT, the hmF2 suddenly began to decrease, which may be related to the northward turning of the IMF.

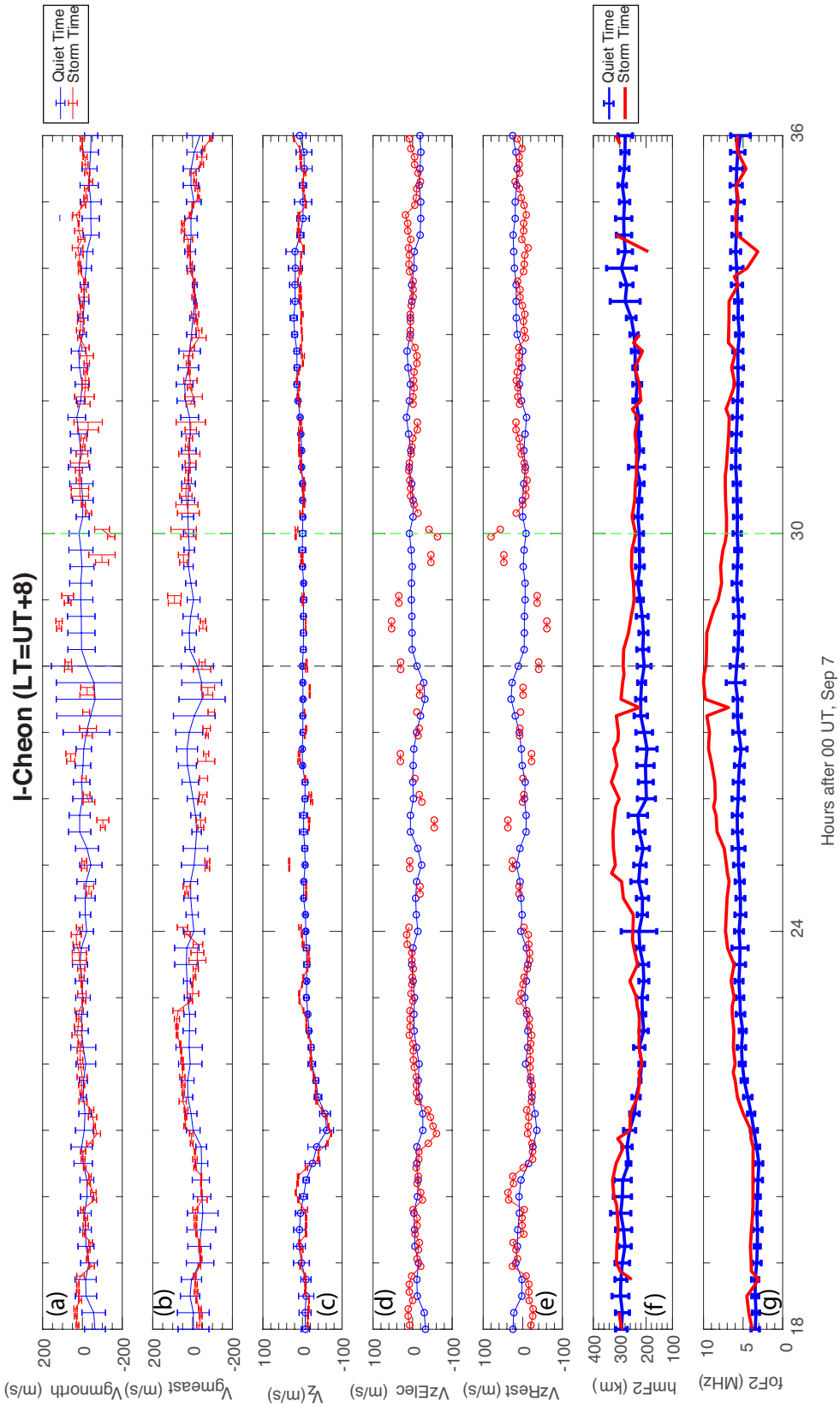

Figure 4.10: Drift data from the digisonde at I-Cheon. The format is the same as Figure 4.5.

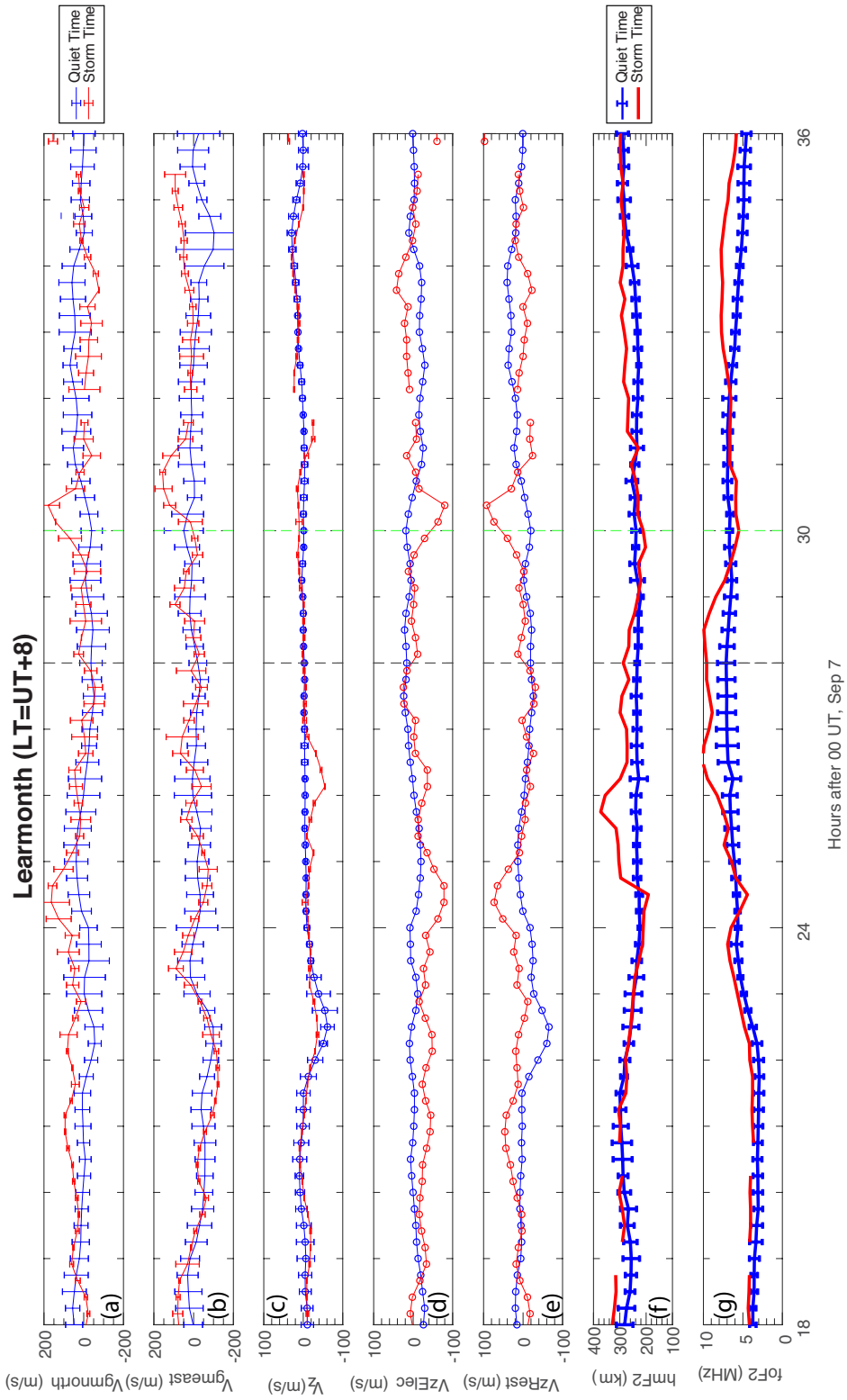

Figure 4.11: Drift data from the digisonde at Learmonth. The format is the same as Figure 4.5.

During 04-06 UT, there were no obvious vertical drifts at I-Cheon and Learmonth. The equatorial electrojet (EEJ) on the same longitude was also close to the quiet-time value at this time (*Rout et al.*, 2019). Meanwhile, the hmF2 and foF2 continuously decreased until the asymmetry fully developed at $\sim$ 06 UT . The faster decreasing rate of the foF2 and hmF2 at Learmonth in the southern hemisphere was likely a result of the downward movement between 02 and 04 UT. This downward movement facilitated an enhanced chemical recombination rate by lowering the plasma to lower altitudes with more molecular neutrals. At 06 UT, both the hmF2 and the foF2 at Learmonth were already lower than the quiet-time values, i.e., ionospheric negative phase, which is consistent with the short-lived negative phase due to the faster VTEC decrease rate in Figure 4.3. The differences in the vertical drift between 02 and 04 UT at I-Cheon and Learmonth gave rise to the hemispheric asymmetry in the East Asian and Australian sector. This hints that the history of the storm can play a role in the development of the asymmetry.

Although the total deviation from the quiet-time value was small in the vertical drift, the separated contributions from the electric field and the combined neutral wind and diffusion (Figure 4.10-4.11) presented nontrivial wave-like structures during both the main and recovery phase. Thus, the existence of TIDs was also examined in the East Asian and Australian sector using the detrended VTEC. The keogram of detrended VTEC for the East Asian-Australian sector (120° - 130° longitude) from 00 to 06 UT is shown in Figure 4.12. In both hemispheres, there were continuous TIDs propagating from the polar region to the low latitude region before 04 UT, and the amplitude of the TIDs was much stronger in the southern hemisphere than that in the conjugate northern hemisphere. The asymmetry of TIDs initiated earlier than the asymmetry of VTEC, which is similar to that seen in the Europe-Africa sector. This suggests the possibility that the energy deposition at auroral latitudes was stronger in the southern hemisphere, as inferred from the magnitude of the TIDs, and led to

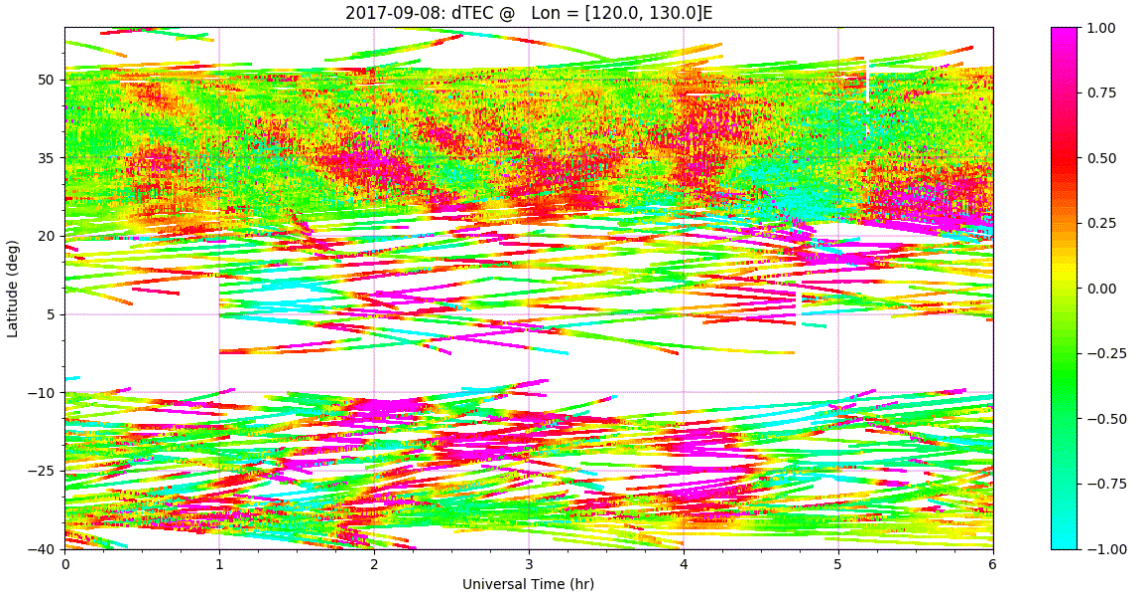

Figure 4.12: Keogram of detrended VTEC for East Asia-Australian sector.

the development of the VTEC asymmetry.

Based on the TID signatures in the drift and dVTEC data, it is found that in both sectors the amplitude of the TIDs was larger in the hemisphere where the negative phase developed later. A further numerical simulation is needed to obtain a more quantitative evaluation.

As shown in Figure 4.9, at around 03 UT on September 8, the TIMED satellite flew over the East Asian-Australian sector. The $[O]/[N_2]$ ratio increase was similar in both hemispheres at 120° E longitude at this time. No asymmetry in VTEC was observed before 04 UT. During the recovery phase, due to a lack of composition data in this region, it is not possible to determine whether or not the composition changes played a key role in the development of the VTEC asymmetry.

4.5 Summary and Conclusions

In this study, the ionospheric responses during the first recovery phase of the geomagnetic storm on September 7-8, 2017, were investigated using the GPS VTEC

observations, the EDP and plasma drift data from digisondes, and the $[O]/[N_2]$ ratio from TIMED GUVI. Hemispheric asymmetries of the ionospheric responses were observed in the mid-latitude regions at two local times simultaneously. Interestingly, the asymmetries at these two local times were opposite to each other: In the European and African sector (early morning), the southern hemisphere was in the positive phase while the northern hemisphere was in the negative phase, i.e., N-S+. In the East Asian and Australian sector (afternoon), the northern hemisphere was in the positive phase and the southern hemisphere was in the negative phase, i.e., N+S-, which was opposite to the asymmetry observed in the European and African sector. Hemispheric asymmetries of the vertical plasma drifts were observed in both sectors. In particular, wave-like TID signatures were observed with different magnitudes in different hemispheres. It is also noticed that the magnitude of the TIDs was larger in the hemisphere where the negative storm phase developed later. These TID signatures were further confirmed in the detrended VTEC keogram. The ionospheric tomographic reconstruction using the dense GPS receiver network in Europe revealed the perturbed ionospheric density as a result of the TIDs. In addition, the thermospheric composition inferred from the TIMED GUVI measurements revealed that the storm-time $[O]/[N_2]$ change was positive in the Africa region, but negative in the conjugate European region, which suggests that the storm-time thermospheric composition change reinforced the seasonal asymmetry and could contribute to the hemispheric asymmetry. Unfortunately, the $[O]/[N_2]$ ratio measurements were not available in the East Asian-Australian sector during the focused period.

In conclusion, the hemispheric asymmetries of the VTEC during this storm recovery phase were generated by a combination of the hemispheric asymmetries of the thermospheric composition change, vertical drift and TID activity. Some asymmetries of these drivers developed before the appearance of the VTEC asymmetries: The downward drift and stronger TID activity in Europe and Australia likely fa-

cilitated the development of the negative phase in the recovery phase. However, it is difficult to quantify the contributions of different drivers based on observations only. A numerical simulation driven by realistic high-latitude drivers is needed for more quantitative evaluations of these various factors that contribute to the observed ionospheric asymmetries.

CHAPTER V

Summary and Conclusions

5.1 Summary of the Results

In this study, several aspects of the ionospheric and thermospheric responses during geomagnetic storms were investigated using both global numerical models and multi-instrument observations. In particular, we emphasized on the formation and evolution of storm-time ionospheric density structures.

In Chapter II, an interesting polar cap patch event during the geomagnetic storm on Sep 7-8, 2017 was presented. During this event, IMF was steady and no signature of transient reconnection was observed on the dayside. Thus, the conventional theories of patch segmentation, which either need fluctuations in the solar wind and IMF or transient reconnections, cannot explain the formation. Thus, a new theory was proposed and the state-of-the-art SWMF simulation method was used to simulate the geospace response and was able to explain the formation of this polar cap patch. This new segmentation mechanism works as follows: Shortly after the southward IMF turning and a partial ring current forms on the nightside equatorial inner magnetosphere. Shielding processes and the associated Region 2 FACs gradually develop and a strong boundary flows between the Region 1 and Region 2 FACs develop. As the partial ring current drifts westward due to the energy dependent drifts of the current carriers, the peak of the boundary flows also move westward. This strong boundary

flow raises the ion temperature through enhanced frictional heating, enhances the chemical recombination reaction rate, and reduces the electron density. When this boundary flow crosses the SED plume, the plume is then segmented into a patch. No external IMF variations or transient reconnections are required in this mechanism.

In Chapter III, we performed a detailed analysis of the temporal evolution of SAPS during a moderate storm based on conjugate observations of SAPS from the VAP and SuperDARN. We proposed the formation mechanism of the meso-scale enhancement of SAPS (MS-SAPS+): A two-loop current wedge is generated following particle injections by the perturbed plasma pressure gradient and the diamagnetic effect of the structured ring current. The closure of thw two-loop current wedge in the ionosphere generates the flow enhancement. Comprehensive observations illustrated the complex electromagnetic perturbations that SAPS can be associated with: In the conjugate ionosphere, MS-SAPS+ develops at the equatorward edge of the Harang reversal. At the poleward edge of the Harang reversal, there is a southeastward convection flow. On the ground, magnetometers also captured the corresponding magnetic perturbations. It is also shown that the substorm onset is not a necessary condition for the development of SAPS. Particle injections are the direct driver of SAPS events.

In Chapter IV, we performed a detailed case analysis of the drivers of the opposite hemispheric asymmetries observed by GPS TEC. TID signatures were identified in the digisonde drift data and the detrended TEC. The amplitude of the TID was asymmetric in the northern and southern hemispheres, and it was larger in the hemisphere with a negative phase later, suggesting that TIDs may provide preconditions for the development of the asymmetries or TIDs are the precursor of the dynamic processes that are responsible for the asymmetry, such as large-scale thermospheric circulation change. Hemispheric differences in the plasma vertical drifts were also observed by digisondes. The vertical movement of the ionosphere may directly and

indirectly contribute to the asymmetry development due to the local imbalance mechanism mentioned previously. In addition, asymmetries of $[O]/[N_2]$ were also observed by the TIMED satellite with increased/decreased $[O]/[N_2]$ collocated with the positive/negative storm. Therefore, the observed hemispheric asymmetries in different local times are suggested to be driven by a combination of the hemispheric asymmetries in the thermospheric composition, plasma vertical drifts, and TID activity.

This dissertation provides several new perspectives on the formation and evolution of ionospheric density structures during storms and the fundamental physical processes behind. It demonstrates the power and necessity of fusioning the multi-instrument measurements and numerical simulations in studying the MIT responses during geomagnetic disturbances.

5.2 Future Work

5.2.1 Can simulations improve the description of structured ionospheric convection flows, such as SAPS?

SAPS is notoriously hard to simulate due to a few reasons. First, it is difficult to provide an accurate description of the conductance in the subauroral region by adequately accounting for the electron and proton precipitations in this sector. Second, a ionosphere-thermosphere code is needed to simulate the effects of enhanced frictional heating and to feedback to the global magnetosphere model. More specifically, the SAPS electric field driven by the magnetospheric drivers increases the plasma flow speed, accelerate neutrals through collisions, and then heats the atmosphere. Subsequently, the heated neutrals increase the recombination rate and lead to the plasma density decrease. This positive feedback is critical for the formation of SAPS. Therefore, we will two-way couple GITM with the BATSRUS-RCM model to capture the positive feedback impact. The block diagram of the coupled model is shown in Fig

5.1. In the two-way coupling between GITM and BATRUS-RCM, GITM gets **FAC!**s and electric potential from BATSRUS-RCM and provides updated conductance back to RIM and then BATSRUS-RCM. We need to compare the results from the two-way coupled model with the results from the one-way coupled model in Chapter II and quantify the influence of the IT coupling on the evolution of SAPS. Later, the comparison between these modeling results and observations should be performed, which can help tell whether the inclusion of the positive feedback can help simulate more realistic SAPS. This work would provide important insight into the importance of the ionosphere-thermosphere processing in the SAPS formation. In addition, an accurate description of the diffuse and soft precipitation is important for the successful simulation of SAPS. We either need to improve the first-principle ring current and radiation belt model to better simulate the precipitation or come up with a better empirical relation between precipitation and particle flux in the magnetosphere.

5.2.2 How does SAPS segment the SED plume?

If SAPS can be successfully simulated with the two-way coupled model, we will test whether SAPS can segment the SED plume into a polar cap patch and how. There are two possible mechanisms: (1) As shown in *Zhang et al.* (2016), SAPS firstly develops in the dusk side and decreases the electron density. Then SAPS travels westward to the dayside, and the low-density plasma carried by it can segment the SED plume. (2) SAPS develops on the duskside, decreases the electron density and segments the plume. The method shown in Chapter II will be used to trace the plasma parcel where the segmentation occurs back in time and terms analysis will be performed to identify the most important contributors.

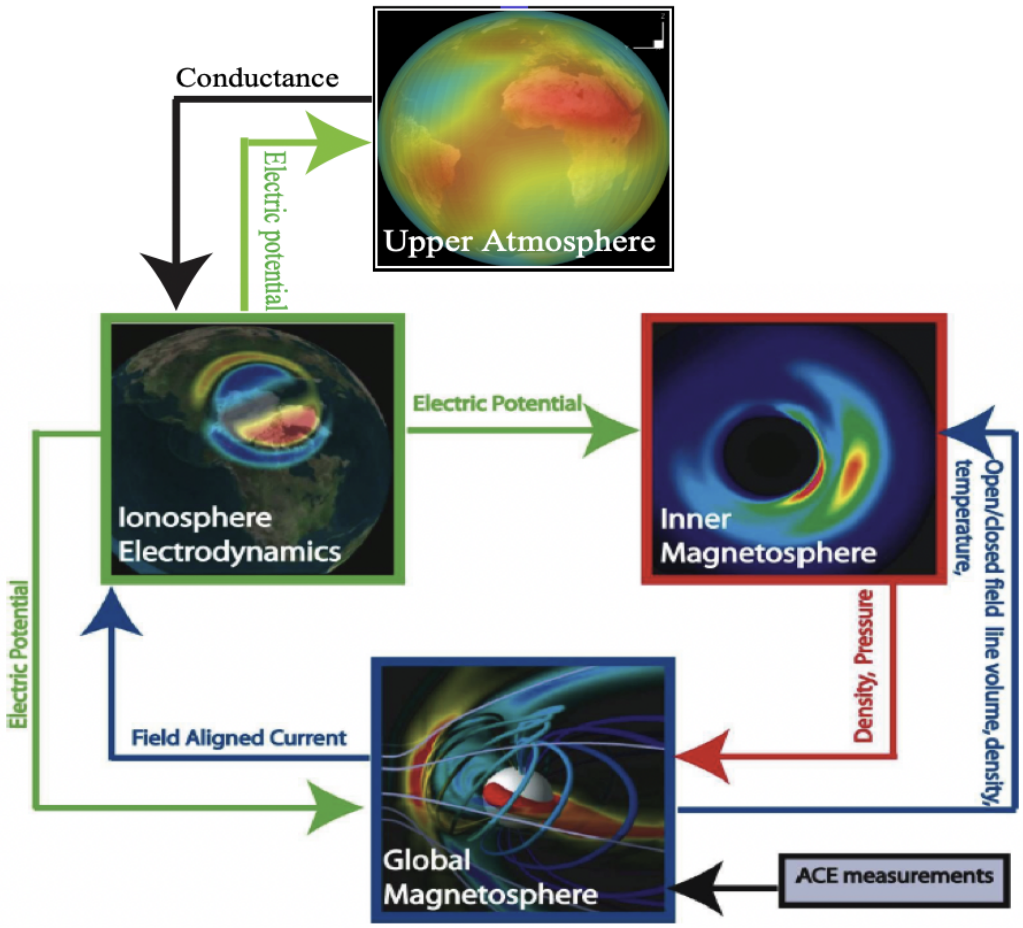

Figure 5.1: Block diagram of the coupled models and with data flow.

5.2.3 Can simulations reproduce the observed hemispheric asymmetries of ionospheric density structures?

In Chapter IV, a qualitative explanation of the hemispheric asymmetries is given. However, based on observations only, it is hard to evaluate which driver is more important. Thus, a numerical simulation is needed for more quantitative evaluations. We will use SWMF to simulate the response of the IT system during the storm. A term analysis will be performed to check the relative role of plasma vertical drift and chemical process. In addition, we will check whether TIDs can be successfully produced in the simulation, and whether they can lead to appreciable changes in the IT system to precondition the positive/negative storms.

BIBLIOGRAPHY

BIBLIOGRAPHY

Aa, E., S. Zou, A. Ridley, S. Zhang, A. J. Coster, P. J. Erickson, S. Liu, and J. Ren (2019), Merging of Storm Time Midlatitude Traveling Ionospheric Disturbances and Equatorial Plasma Bubbles, *Space Weather*, *17*(2), 285–298, doi: 10.1029/2018SW002101.

Aa, E., et al. (2018), Midlatitude Plasma Bubbles Over China and Adjacent Areas During a Magnetic Storm on 8 September 2017, *Space Weather*, *16*(3), 321–331, doi:10.1002/2017SW001776.

Anderson, B., H. Korth, C. Waters, D. Green, V. Merkin, R. Barnes, and L. Dyrud (2014), Development of large-scale birkeland currents determined from the active magnetosphere and planetary electrodynamics response experiment, *Geophysical Research Letters*, *41*(9), 3017–3025.

Anderson, D. N., J. Buchau, and R. A. Heelis (1988), Origin of density enhancements in the winter polar cap ionosphere, *Radio Science*, *23*(4), 513–519, doi:10.1029/RS023i004p00513.

Anderson, P. C. (2004), Subauroral electric fields and magnetospheric convection during the April, 2002 geomagnetic storms, *Geophysical Research Letters*, *31*(11), 2000–2003, doi:10.1029/2004GL019588.

Anderson, P. C., R. A. Heelis, and W. B. Hanson (1991), The ionospheric signatures of rapid subauroral ion drifts, *Journal of Geophysical Research*, *96*(A4), 5785, doi: 10.1029/90JA02651.

Anderson, P. C., W. B. Hanson, R. A. Heelis, J. D. Craven, D. N. Baker, and L. A. Frank (1993), A proposed production model of rapid subauroral ion drifts and their relationship to substorm evolution, *Journal of Geophysical Research*, *98*(92), 6069, doi:10.1029/92JA01975.

Anderson, P. C., D. L. Carpenter, K. Tsuruda, T. Mukai, and F. J. Rich (2001), Multisatellite observations of rapid subauroral ion drifts (SAID), *Journal of Geophysical Research*, *106*(A12), 29,585, doi:10.1029/2001JA000128.

Angelopoulos, V., W. Baumjohann, C. F. Kennel, F. V. Coroniti, M. G. Kivelson, R. Pellat, R. J. Walker, H. Lühr, and G. Paschmann (1992), Bursty bulk flows in the inner central plasma sheet, *Journal of Geophysical Research*, *97*(A4), 4027, doi:10.1029/91JA02701.

Archer, W. E., and D. J. Knudsen (2018), Distinguishing Subauroral Ion Drifts From Birkeland Current Boundary Flows, *Journal of Geophysical Research: Space Physics*, doi:10.1002/2017JA024577.

Archer, W. E., D. J. Knudsen, J. K. Burchill, B. Jackel, E. Donovan, M. Connors, and L. Juusola (2017), Birkeland current boundary flows, *Journal of Geophysical Research: Space Physics*, *122*(4), 4617–4627, doi:https://doi.org/10.1002/2016JA023789.

Arnoldy, R., and T. Moore (1983), Longitudinal structure of substorm injections at synchronous orbit, *Journal of Geophysical Research: Space Physics*, *88*(A8), 6213–6220.

Astafyeva, E., I. Zakharenkova, and E. Doornbos (2015a), Opposite hemispheric asymmetries during the ionospheric storm of 29-31 August 2004, *Journal of Geophysical Research: Space Physics*, *120*(1), 697–714, doi:10.1002/2014JA020710.

Astafyeva, E., I. Zakharenkova, and M. Förster (2015b), Ionospheric response to the 2015 st. patrick's day storm: A global multi-instrumental overview, *Journal of Geophysical Research: Space Physics*, *120*(10), 9023–9037, doi:10.1002/2015JA021629.

Astafyeva, E., M. S. Bagiya, M. Förster, and N. Nishitani (2020), Unprecedented hemispheric asymmetries during a surprise ionospheric storm: a game of drivers, *Journal of Geophysical Research: Space Physics*, pp. 35–39, doi:10.1029/2019JA027261.

Banks, P. M., and F. Yasuhara (1978), Electric fields and conductivity in the nighttime E-regio, *Geophysical Research Letters*, *5*(12), 1047–1050.

Baumjohann, W., and R. A. Treumann (1997), *Basic space plasma physics*, World Scientific.

Biqiang Zhao, Weixing Wan, Libo Liu, and Zhipeng Ren (2009), Characteristics of the ionospheric total electron content of the equatorial ionization anomaly in the Asian-Australian region during 1996-2004, *Annales Geophysicae*, *27*(10), 3861–3873, doi:10.5194/angeo-27-3861-2009.

Birn, J., and M. Hesse (2013), The substorm current wedge in mhd simulations, *Journal of Geophysical Research: Space Physics*, *118*(6), 3364–3376, doi:https://doi.org/10.1002/jgra.50187.

Blake, J. B., et al. (2014), The Magnetic Electron Ion Spectrometer (MagEIS) instruments aboard the Radiation Belt Storm Probes (RBSP) spacecraft, *Space Science Review*, *9781489974*, 383–421, doi:10.1007/978-1-4899-7433-4-12.

Brekke, A., and J. Moen (1993), Observations of high latitude ionospheric conductances, *Journal of atmospheric and terrestrial physics*, *55*(11-12), 1493–1512.

Bullett, T. W. (1994), Mid-latitude ionospheric plasma drift: A comparison of digital ionosonde and incoherent scatter radar measurements at Millstone Hill. Doctoral dissertation. Retrieved from ProQuest Dissertations Theses Global. (304103954). Lowell, MA: University of Massachusetts.

Burke, W. J., F. J. Rich, O. De, L. Beaujardiere, C. Y. Huang, and G. R. Wilson (2000), Ionospheric disturbances observed by DMSP at middle to low latitudes during the magnetic storm of June 4-6, *Journal of Geophysical Research*, *105405*(1), 391–18.

Buzulukova, N., M.-C. Fok, A. Pulkkinen, M. Kuznetsova, T. E. Moore, A. Glocer, P. C. Brandt, G. Toth, and L. Rastaetter (2010), Dynamics of Ring Current and Electric Fields in the Inner Magnetosphere During Disturbed Periods: CRCM-BATS-R-US Coupled Model, *Journal of Geophysical Research : Space Physics*, *115*, 1–19, doi:10.1029/2009JA014621.

Califf, S., X. Li, R. A. Wolf, H. Zhao, A. N. Jaynes, F. D. Wilder, D. M. Malaspina, and R. Redmon (2016), Large-amplitude electric fields in the inner magnetosphere: Van Allen Probes observations of subauroral polarization streams, *Journal of Geophysical Research : Space Physics*, pp. 1–3, doi:10.1002/2016JA023362.

Carlson, H. C., K. Oksavik, J. Moen, and T. Pedersen (2004), Ionospheric patch formation: Direct measurements of the origin of a polar cap patch, *Geophysical Research Letters*, *31*(8), 2–5, doi:10.1029/2003GL018166.

Carlson, H. C., J. Moen, K. Oksavik, C. P. Nielsen, I. W. McCrea, T. R. Pedersen, and P. Gallop (2006), Direct observations of injection events of subauroral plasma into the polar cap, *Geophysical Research Letters*, *33*(5), 5–8, doi:10.1029/2005GL025230.

Chamberlin, P. C., T. N. Woods, and F. G. Eparvier (2007), Flare irradiance spectral model (FISM): Daily component algorithms and results, *Space Weather*, *5*(7), 1–23, doi:10.1029/2007SW000316.

Clauer, C. R., X. Cai, D. Welling, A. DeJong, and M. G. Henderson (2006), Characterizing the 18 april 2002 storm-time sawtooth events using ground magnetic data, *Journal of Geophysical Research: Space Physics*, *111*(A4).

Clausen, L. B., et al. (2012), Large-scale observations of a subauroral polarization stream by midlatitude SuperDARN radars: Instantaneous longitudinal velocity variations, *Journal of Geophysical Research: Space Physics*, *117*(5), 1–11, doi:10.1029/2011JA017232.

Cowley, S., J. Morelli, and M. Lockwood (1991), Dependence of convective flows and particle precipitation in the high-latitude dayside ionosphere on the x and y components of the interplanetary magnetic field, *Journal of Geophysical Research: Space Physics*, *96*(A4), 5557–5564.

De Keyser, J. (1999), Formation and evolution of subauroral ion drifts in the course of a substorm, *Journal of Geophysical Research : Space Physics*, *104*, 339–349.

De Zeeuw, D. L., S. Sazykin, R. A. Wolf, T. I. Gombosi, A. J. Ridley, and G. Tóth (2004), Coupling of a global MHD code and an inner magnetospheric model: Initial results, *Journal of Geophysical Research: Space Physics*, *109*(A12), 1–14, doi:10.1029/2003JA010366.

Duncan, R. (1969), F-region seasonal and magnetic-storm behaviour, *Journal of Atmospheric and Terrestrial Physics*, *31*(1), 59–70.

Dungey, J. W. (1961), Interplanetary magnetic field and the auroral zones, *Physical Review Letters*, *6*(2), 47.

Echer, E., W. D. Gonzalez, and B. T. Tsurutani (2008), Interplanetary conditions leading to superintense geomagnetic storms (dst â€ â250 nt) during solar cycle 23, *Geophysical Research Letters*, *35*(6), doi:https://doi.org/10.1029/2007GL031755.

Erickson, P. J., F. Beroz, and M. Z. Miskin (2011), Statistical characterization of the American sector subauroral polarization stream using incoherent scatter radar, *Journal of Geophysical Research: Space Physics*, *116*(3), 1–8, doi:10.1029/2010JA015738.

Forsyth, C., et al. (2008), Observed tail current systems associated with bursty bulk flows and auroral streamers during a period of multiple substorms, *Annales Geophysicae*, *26*(1), 167–184, doi:10.5194/angeo-26-167-2008.

Foster, J. C. (1984), Ionospheric Signatures of Magnetospheric Convection, *Journal of Geophysical Research*, *89*(2), 855–865.

Foster, J. C., P. J. Erickson, A. J. Coster, J. Goldstein, and F. J. Rich (2002), Ionospheric signatures of plasmaspheric tails, *Geophysical Research Letters*, *29*(13), 1, doi:10.1029/2002GL015067.

Fuller-Rowell, T., and D. Rees (1987), Interactions between neutral thermospheric composition ionosphere using a coupled ionosphere-thermosphere and the polar model, *Journal of Geophysical Research*, *92*, 7744–7748.

Funsten, H. O., et al. (2014), Helium, oxygen, proton, and electron (HOPE) mass spectrometer for the Radiation Belt Storm Probes mission, *Space Science Review*, pp. 423–484, doi:10.1007/978-1-4899-7433-4-13.

Gallardo-Lacourt, B., Y. Nishimura, L. Lyons, S. Zou, V. Angelopoulos, E. Donovan, K. McWilliams, J. Ruohoniemi, and N. Nishitani (2014), Coordinated superdarn themis asi observations of mesoscale flow bursts associated with auroral streamers, *Journal of Geophysical Research: Space Physics*, *119*(1), 142–150.

Gallardo-Lacourt, B., Y. Nishimura, L. R. Lyons, E. V. Mishin, J. M. Ruohoniemi, E. F. Donovan, V. Angelopoulos, and N. Nishitani (2017), Influence of auroral streamers on rapid evolution of ionospheric SAPS flows, *Journal of Geophysical Research: Space Physics*, (1993), 1–15, doi:10.1002/2017JA024198.

Gjerloev, J. W. (2012), The SuperMAG data processing technique, *Journal of Geophysical Research: Space Physics*, *117*(9), 1–19, doi:10.1029/2012JA017683.

Gkioulidou, M., A. Y. Ukhorskiy, D. G. Mitchell, T. Sotirelis, B. H. Mauk, and L. J. Lanzerotti (2014), The role of small-scale ion injections in the buildup of Earth's ring current pressure: Van Allen Probes observations of the 17 March 2013 storm, *Journal of Geophysical Research: Space Physics*, *119*(9), 7327–7342, doi: 10.1002/2014JA020096.

Goncharenko, L. P., J. Foster, A. Coster, C. Huang, N. Aponte, and L. Paxton (2007), Observations of a positive storm phase on september 10, 2005, *Journal of atmospheric and solar-terrestrial physics*, *69*(10-11), 1253–1272.

Gonzales, C. A., R. A. Behnke, and R. F. Woodman (1982), Doppler measurements with a digital ionosonde: Technique and comparison of results with incoherent scatter data, *17*(5), 1327–1333.

Gonzalez, W. D., J. A. Joselyn, Y. Kamide, H. W. Kroehl, G. Rostoker, B. T. Tsurutani, and V. M. Vasyliunas (1994), What is a geomagnetic storm?, *Journal of Geophysical Research: Space Physics*, *99*(A4), 5771–5792, doi:https://doi.org/10.1029/93JA02867.

Goodwin, L. V., et al. (2015), Swarm in situ observations of F region polar cap patches, *Geophysical Research Letters*, pp. 1–8, doi:10.1002/2014GL062610. High-resolution.

Gurgiolo, C., C. S. Lin, B. Mauk, G. K. Parks, and C. Mcilwain (1979), Plasma Injection and Diamagnetism, *Journal of Geophysical Research*, *84*(8).

Habarulema, J. B., et al. (2020), Ionospheric response at conjugate locations during the 7-8 september 2017 geomagnetic storm over the europe-african longitude sector, *Journal of Geophysical Research: Space Physics*, *125*(10), e2020JA028,307, doi: https://doi.org/10.1029/2020JA028307.

Hasegawa, A., and T. Sato (1979), Generation of field aligned current during substorm, in *Dynamics of the Magnetosphere*, pp. 529–542, Springer.

He, F., X. X. Zhang, W. Wang, and W. Wan (2017a), Different Evolution Patterns of Subauroral Polarization Streams (SAPS) During Intense Storms and Quiet Time Substorms, *Geophysical Research Letters*, *44*(21), 10,796–10,804, doi: 10.1002/2017GL075449.

He, F., X.-X. Zhang, W. Wang, L. Liu, Z.-P. Ren, X. Yue, L. Hu, W. Wan, and H. Wang (2018), Large-scale structure of subauroral polarization streams during the main phase of a severe geomagnetic storm, *Journal of Geophysical Research: Space Physics*, *123*(4), 2964–2973.

He, Z., L. Chen, H. Zhu, Z. Xia, G. D. Reeves, Y. Xiong, L. Xie, and Y. Cao (2017b), Multiple-Satellite Observation of Magnetic Dip Event During the Substorm on 10 October 2013, *Geophysical Research Letters*, pp. 1–9, doi:10.1002/2017GL074869.

Heelis, R. A., G. J. Bailey, R. Sellek, R. J. Moffett, and B. Jenkins (1993), Field-aligned drifts in subauroral ion drift events, *Journal of Geophysical Research: Space Physics*, *98*(A12), 21,493–21,499, doi:10.1029/93JA02209.

Heelis, R. A., J. J. Sojka, M. David, and R. W. Schunk (2009), Storm time density enhancements in the middle-latitude dayside ionosphere, *Journal of Geophysical Research: Space Physics*, *114*(3), 1–7, doi:10.1029/2008JA013690.

Henderson, M. G. (2013), Auroral Substorms, Poleward Boundary Activations, Auroral Streamers, Omega Bands, and Onset Precursor Activity, *Auroral Phenomenology and Magnetospheric Processes: Earth and Other Planets*, pp. 39–54, doi:10.1029/2011GM001165.

Henderson, M. G., G. D. Reeves, and J. S. Murphree (1998), Are north-south aligned auroral structures an ionospheric manifestation of bursty bulk flows?, *Geophysical Research Letters*, *25*(19), 3737–3740, doi:10.1029/98GL02692.

Huang, C. S., and J. C. Foster (2007), Correlation of the subauroral polarization streams (SAPS) with the Dst index during severe magnetic storms, *Journal of Geophysical Research: Space Physics*, *112*(11), 1–8, doi:10.1029/2007JA012584.

Huang, X., and B. Reinisch (1996), Vertical electron density profiles from the digisonde network, *Advances in Space Research*, *18*(6), 121–129.

Iijima, T., and T. A. Potemra (1978), Large-scale characteristics of field-aligned currents associated with substorms, *Journal of Geophysical Research: Space Physics*, *83*(A2), 599–615, doi:https://doi.org/10.1029/JA083iA02p00599.

Imtiaz, N., W. Younas, and M. Khan (2020), Response of the low-to mid-latitude ionosphere to the geomagnetic storm of september 2017, *AnGeo*, *38*(2), 359–372.

Jimoh, O., J. Lei, and J. Zhong (2019), Topside Ionospheric Conditions During the 7-8 September 2017 Geomagnetic Storm, *Journal of Geophysical Research : Space Physics*, pp. 9381–9404, doi:10.1029/2019JA026590.

Jin, H., S. Zou, G. Chen, C. Yan, S. Zhang, and G. Yang (2018), Formation and Evolution of Low-Latitude F Region Field-Aligned Irregularities During the 7ÃÂ¢ÃÂÃÂ8 September 2017 Storm: Hainan Coherent Scatter Phased Array Radar and Digisonde Observations, *Space Weather*, *16*(6), 648–659, doi:10.1029/2018SW001865.

Joselyn, J. A., and B. T. Tsurutani (1990), Geomagnetic sudden impulses and storm sudden commencements: A note on terminology, *Eos, Transactions American Geophysical Union*, *71*(47), 1808–1809, doi:https://doi.org/10.1029/90EO00350.

Karlsson, T., G. T. Marklund, L. G. Blomberg, and A. Mälkki (1998), Subauroral electric fields observed by the Freja satellite: A statistical study, *Journal of Geophysical Research*, *103*(1), 4327, doi:10.1029/97JA00333.

Kelley, M. C. (2009), *The Earth's ionosphere: plasma physics and electrodynamics*, Academic press.

Kelley, M. C., J. J. Makela, J. L. Chau, and M. J. Nicolls (2003), Penetration of the solar wind electric field into the magnetosphere/ionosphere system, *Geophysical Research Letters*, *30*(4), doi:https://doi.org/10.1029/2002GL016321.

Kil, H., Y. S. Kwak, L. J. Paxton, R. R. Meier, and Y. Zhang (2011), O and N2 disturbances in the F region during the 20 November 2003 storm seen from TIMED/GUVI, *Journal of Geophysical Research: Space Physics*, *116*(2), 1–9, doi:10.1029/2010JA016227.

Kim, K. H., F. S. Mozer, D. H. Lee, and H. Jin (2010), Large electric field at the nightside plasmapause observed by the Polar spacecraft, *Journal of Geophysical Research: Space Physics*, *115*(7), 2–7, doi:10.1029/2010JA015439.

Kivelson, M. G., M. G. Kivelson, and C. T. Russell (1995), *Introduction to space physics*, Cambridge university press.

Kletzing, C. A., et al. (2014), The Electric and Magnetic Field Instrument suite and Integrated Science (EMFISIS) on RBSP, *Space Science Review*, pp. 127–181, doi:10.1007/978-1-4899-7433-4-5.

Kunduri, B. S., J. B. Baker, J. M. Ruohoniemi, E. G. Thomas, S. G. Shepherd, and K. T. Sterne (2017), Statistical characterization of the large-scale structure of the subauroral polarization stream, *Journal of Geophysical Research: Space Physics*, *122*(6), 6035–6048, doi:10.1002/2017JA024131.

Lei, J., et al. (2018), Was Magnetic Storm the Only Driver of the Long-Duration Enhancements of Daytime Total Electron Content in the Asian-Australian Sector Between 7 and 12 September 2017?, *Journal of Geophysical Research: Space Physics*, *123*(4), 3217–3232, doi:10.1029/2017JA025166.

Lejosne, S., and F. S. Mozer (2017), Sub-Auroral Polarization Stream (SAPS) duration as determined from Van Allen Probe successive electric drift measurements, *Geophysical Research Letters*, doi:10.1002/2017GL074985.

Lin, D., et al. (2019), Saps in the 17 march 2013 storm event: Initial results from the coupled magnetosphere-ionosphere-thermosphere model, *Journal of Geophysical Research: Space Physics*, *124*(7), 6212–6225.

Liu, J., W. Wang, A. Burns, S. C. Solomon, S. Zhang, Y. Zhang, and C. Huang (2016), Relative importance of horizontal and vertical transports to the formation of ionospheric storm-enhanced density and polar tongue of ionization, *Journal of Geophysical Research: Space Physics*, *121*(8), 8121–8133, doi:10.1002/2016JA022882.

Lockwood, M., and H. C. Carlson (1992), Production of Polar Cap Electron Density Patches by Transit Mangetopause Reconnection, *Geophys. Res. Lett.*, *19*(17), 1731–1734.

Lu, G., L. Goncharenko, M. J. Nicolls, A. Maute, A. Coster, and L. J. Paxton (2012), Ionospheric and thermospheric variations associated with prompt penetration electric fields, *Journal of Geophysical Research: Space Physics*, *117*(8), 1–14, doi:10.1029/2012JA017769.

Lühr, H., J. Park, J. W. Gjerloev, J. Rauberg, I. Michaelis, J. M. Merayo, and P. Brauer (2015), Field-aligned currents' scale analysis performed with the swarm constellation, *Geophysical Research Letters*, *42*(1), 1–8.

Makarevich, R. A., A. C. Kellerman, Y. V. Bogdanova, and A. V. Koustov (2009), Time evolution of the subauroral electric fields: A case study during a sequence of two substorms, *Journal of Geophysical Research: Space Physics*, *114*(4), 1–13, doi:10.1029/2008JA013944.

Makarevich, R. A., A. C. Kellerman, J. C. Devlin, H. Ye, L. R. Lyons, and Y. Nishimura (2011), SAPS intensification during substorm recovery: A multi-instrument case study, *Journal of Geophysical Research: Space Physics*, *116*(11), 1–16, doi:10.1029/2011JA016916.

Mannucci, A. J., B. T. Tsurutani, M. C. Kelley, B. A. Iijima, and A. Komjathy (2009), Local time dependence of the prompt ionospheric response for the 7, 9, and 10 November 2004 superstorms, *Journal of Geophysical Research: Space Physics*, *114*(10), 1–12, doi:10.1029/2009JA014043.

Maruyama, N., A. D. Richmond, S. Sazykin, G. H. Millward, M. V. Codrescu, F. R. Toffoletto, T. J. Fuller-Rowell, and R. W. Spiro (2005), Interaction between direct penetration and disturbance dynamo electric fields in the storm-time equatorial ionosphere, *Geophysical Research Letters*, *32*(17), 2–5, doi:10.1029/2005gl023763.

Mauk, B. H., N. J. Fox, S. G. Kanekal, R. L. Kessel, D. G. Sibeck, and A. Ukhorskiy (2014), Science objectives and rationale for the Radiation Belt Storm Probes mission, *Space Science Review*, *9781489974*, 3–27, doi:10.1007/978-1-4899-7433-4-2.

McGranaghan, R. M., A. J. Mannucci, and C. Forsyth (2017), A comprehensive analysis of multiscale field-aligned currents: Characteristics, controlling parameters, and relationships, *Journal of Geophysical Research: Space Physics*, *122*(12).

McPherron, R. L. (2015), Earth's magnetotail, in *Magnetotails in the Solar System*, chap. 4, pp. 61–84, American Geophysical Union, doi:10.1002/9781118842324.ch4.

Mendillo, M. (2006), Storms in the ionosphere: Patterns and processes for total electron content, *Reviews of Geophysics*, *44*(4), 1–47, doi:10.1029/2005RG000193.

Milan, S. E., M. Lester, and T. K. Yeoman (2002), HF radar polar patch formation revisited: Summer and winter variations in dayside plasma structuring, *Annales Geophysicae*, *20*(4), 487–499, doi:10.5194/angeo-20-487-2002.

Mishin, E. V. (2013), Interaction of substorm injections with the subauroral geospace: 1. Multispacecraft observations of SAID, *Journal of Geophysical Research: Space Physics*, *118*(9), 5782–5796, doi:10.1002/jgra.50548.

Mishin, E. V. (2016), SAPS onset timing during substorms and the westward traveling surge, *Geophysical Research Letters*, *43*(13), 6687–6693, doi:10.1002/2016GL069693.

Mishin, E. V., and P. A. Puhl-Quinn (2007), SAID: Plasmaspheric short circuit of substorm injections, *Geophysical Research Letters*, *34*(24), 2–5, doi:10.1029/2007GL031925.

Moen, J., H. C. Carlson, K. Oksavik, C. P. Nielsen, S. E. Pryse, H. R. Middleton, I. W. McCrea, and P. Gallop (2006), EISCAT observations of plasma patches at sub-auroral cusp latitudes, *Annales Geophysicae*, *24*(9), 2363–2374, doi:10.5194/angeo-24-2363-2006.

Moore, T., R. Arnoldy, J. Feynman, and D. Hardy (1981), Propagating substorm injection fronts, *Journal of Geophysical Research: Space Physics*, *86*(A8), 6713–6726.

Mosna, Z., D. Kouba, P. K. Knizova, D. Buresova, J. Chum, T. Sindelarova, J. Urbar, J. Boska, and D. S. Jankovicova (2020), Ionospheric storm of September 2017 observed at ionospheric station Pruhonice, the Czech Republic, *Advances in Space Research*, *65*(1), 115–128, doi:10.1016/j.asr.2019.09.024.

Nakamura, R., W. Baurnjohann, M. Brittnacher, V. A. Sergeev, M. Kubyshkina, T. Mukai, and K. Liou (2001), Flow bursts and auroral activations: Onset timing and foot point location, *Journal of Geophysical Research*, *106*, 777–789.

Nishimura, Y., J. Wygant, T. Ono, M. Iizima, A. Kumamoto, D. Brautigam, and R. Friedel (2008), SAPS measurements around the magnetic equator by CRRES, *Geophysical Research Letters*, *35*(10), 1–5, doi:10.1029/2008GL033970.

Nishimura, Y., L. R. Lyons, V. Angelopoulos, T. Kikuchi, S. Zou, and S. B. Mende (2011), Relations between multiple auroral streamers, pre-onset thin arc formation, and substorm auroral onset, *Journal of Geophysical Research: Space Physics*, *116*(9), 1–10, doi:10.1029/2011JA016768.

Ogawa, T., S. C. Buchert, N. Nishitani, N. Sato, and M. Lester (2001), Plasma density suppression process around the cusp revealed by simultaneous CUTLASS

and EISCAT Svalbard radar observations, *Journal of Geophysical Research: Space Physics*, *106*(A4), 5551–5564, doi:10.1029/2000ja900111.

Ogino, T. (1986), A three-dimensional mhd simulation of the interaction of the solar wind with the earth's magnetosphere: The generation of field-aligned currents, *Journal of Geophysical Research: Space Physics*, *91*(A6), 6791–6806, doi:https://doi.org/10.1029/JA091iA06p06791.

Oksavik, K., R. A. Greenwald, J. M. Ruohoniemi, M. R. Hairston, L. J. Paxton, J. B. H. Baker, J. W. Gjerloev, and R. J. Barnes (2006), First observations of the temporal/spatial variation of the sub-auroral polarization stream from the SuperDARN Wallops HF radar, *Geophysical Research Letters*, *33*(12), 1–5, doi:10.1029/2006GL026256.

Østgaard, N., R. R. Vondrak, J. W. Gjerloev, and G. Germany (2002), A relation between the energy deposition by electron precipitation and geomagnetic indices during substorms, *Journal of Geophysical Research: Space Physics*, *107*(A9), 1–7, doi:10.1029/2001JA002003.

Pinnock, M., A. S. Rodger, J. R. Dudeney, K. B. Baker, P. T. Newell, R. A. Greenwald, and M. E. Greenspan (1993), Observations of an enhanced convection channel in the cusp ionosphere, *Journal of Geophysical Research: Space Physics*, *98*(A3), 3767–3776, doi:10.1029/92ja01382.

Powell, K. G., P. L. Roe, T. J. Linde, T. I. Gombosi, and D. L. De Zeeuw (1999), A Solution-Adaptive Upwind Scheme for Ideal Magnetohydrodynamics, *Journal of Computational Physics*, *154*(2), 284–309, doi:10.1006/jcph.1999.6299.

Prölss, G. (1980), Magnetic storm associated perturbations of the upper atmosphere: Recent results obtained by satellite-borne gas analyzers, *Reviews of Geophysics*, *18*(1), 183–202.

Prölss, G. (1993), On explaining the local time variation of ionospheric storm effects, *Annales Geophysicae*, *11*, 1–9.

Prölss, G. W. (1995), Ionospheric F-region storms, in *Handbook of Atmospheric Electrodynamics (1995): Volume II*, edited by H. Volland, pp. 195–235, Boca Raton, FL: CRC Press.

Puhl-Quinn, P. A., H. Matsui, E. Mishin, C. Mouikis, L. Kistler, Y. Khotyaintsev, P. M. E. Décréau, and E. Lucek (2007), Cluster and DMSP observations of SAID electric fields, *Journal of Geophysical Research: Space Physics*, *112*(5), 1–10, doi:10.1029/2006JA012065.

Reeves, G., M. Henderson, P. McLachlan, R. Belian, R. Friedel, and A. Korth (1996), Radial propagation of substorm injections, in *International conference on substorms*, vol. 389, p. 579.

Reinisch, B. W., L. Scali, and D. M. Haines (1998), Ionospheric drfit measurements with digisondes, *Annali Di Geofisca*, *41*.

Remya, B., D. Sibeck, A. Halford, K. Murphy, G. , H. Singer, J. Wygant, G. Farinas Perez, and S. Thaller (2018), Ion injection triggered emic waves in the earth's magnetosphere, *Journal of Geophysical Research: Space Physics*.

Ren, J., S. Zou, R. G. Gillies, E. Donovan, and R. H. Varney (2018), Statistical Characteristics of Polar Cap Patches Observed by RISR-C, *Journal of Geophysical Research: Space Physics*, *123*(8), 6981–6995, doi:10.1029/2018JA025621.

Rideout, W., and A. Coster (2006), Automated gps processing for global total electron content data, *GPS solutions*, *10*(3), 219–228.

Ridley, A. J., T. I. Gombosi, and D. L. Dezeeuw (2004), Ionospheric control of the magnetosphere : conductance, *Annales Geophysicae*, *22*(2), 567–584.

Ridley, A. J., Y. Deng, and G. Tóth (2006), The global ionosphere-thermosphere model, *Journal of Atmospheric and Solar-Terrestrial Physics*, *68*(8), 839–864, doi:10.1016/j.jastp.2006.01.008.

Rodger, A. S., M. Pinnock, J. R. Dudeney, K. B. Baker, and R. A. Greenwald (1994), A new mechanism for polar patch formation, *Journal of Geophysical Research: Space Physics*, *99*(A4), 6425–6436, doi:10.1029/93JA01501.

Rout, D., K. Pandey, D. Chakrabarty, R. Sekar, and X. Lu (2019), Significant Electric Field Perturbations in Low Latitude Ionosphere due to the Passage of Two Consecutive ICMEs During 6–8 September 2017, *Journal of Geophysical Research: Space Physics*, *124*(11), 9494–9510, doi:10.1029/2019JA027133.

Ruohoniemi, J. M., and R. A. Greenwald (1998), The response of high-latitude convection to a sudden southward imf turning, *Geophysical Research Letters*, *25*(15), 2913–2916, doi:https://doi.org/10.1029/98GL02212.

Russell, C. T., R. L. McPherron, and R. K. Burton (1974), On the cause of geomagnetic storms, *Journal of Geophysical Research (1896-1977)*, *79*(7), 1105–1109, doi:https://doi.org/10.1029/JA079i007p01105.

Scali, J. L., B. W. Reinisch, and C. J. Heinselman (1995), Coordinated digisonde and incoherent scatter radar F region drift measurements at Sondre Stromfjord the mean, *Radio Science*, *30*(5), 1481–1498.

Schlesier, A. C., and M. J. Buonsanto (1999), The Millstone Hill ionospheric model and its application to the May 26-27, 1990, ionospheric storm, *Journal of Geophysical Research: Space Physics*, *104*(A10), 22,453–22,468, doi:10.1029/1999ja900250.

Schunk, R., and A. Nagy (2009), *Ionospheres: physics, plasma physics, and chemistry*, Cambridge, England: Cambridge University Press.

Schunk, R. W., P. M. Banks, and W. J. Raitt (1976), Effects of electric fields and other processes upon the nighttime high-latitude F layer, *Journal of Geophysical Research*, *81*(19), 3271, doi:10.1029/JA081i019p03271.

Sergeev, V. A., O. A. Aulamo, R. J. Pellinen, K. V. M., T. Bosinger, C. A. Cattell, R. C. Elphic, and D. J. Williams (1990), NON-SUBSTORM TRANSIENT INJECTION EVENTS, *Planetary and Space Science*, *38*(2), 231–239.

Sergeev, V. A., K. Liou, C. Meng, P. T. Newell, M. Brittnacher, G. Parks, and G. D. Reeves (1999), Development of auroral streamers in association with localized impulsive injections to the inner magnetotail, *Geophysical Research Letters*, *26*(3), 417, doi:10.1029/1998GL900311.

Shen, C., B. Luo, Y. Chi, M. Xu, and Y. Wang (2018), Why the Shock-ICME Complex Structure Is Important: Learning from the Early 2017 September CMEs, *The Astrophysical Journal*, *861*(1), 28, doi:10.3847/1538-4357/aac204.

Shepherd, S., and J. Ruohoniemi (2000), Electrostatic potential patterns in the high-latitude ionosphere constrained by superdarn measurements, *Journal of Geophysical Research: Space Physics*, *105*(A10), 23,005–23,014.

Sojka, J. J., M. D. Bowline, R. W. Schunk, D. T. Decker, C. E. Valladares, R. Sheehan, D. N. Anderson, and R. A. Heelis (1993), Modeling polar cap F-region patches using time varying convection, *Geophysical Research Letters*, *20*(17), 1783–1786, doi:10.1029/93GL01347.

Southwood, D. J., and R. A. Wolf (1978), An assessment of the role of precipitation in magnetospheric convection, *Journal of Geophysical Research: Space Physics*, *83*(A11), 5227–5232, doi:10.1029/JA083iA11p05227.

St.-Maurice, J. P., and D. G. Torr (1978), Nonthermal rate coefficients in the ionosphere: The reactions of o+ with n2, o2, and no, *Journal of Geophysical Research: Space Physics*, *83*(A3), 969–977, doi:https://doi.org/10.1029/JA083iA03p00969.

Strickland, D., J. Evans, and L. Paxton (1995), Satellite remote sensing of thermospheric o/n2 and solar euv: 1. theory, *Journal of Geophysical Research: Space Physics*, *100*(A7), 12,217–12,226.

Strickland, D., J. Bishop, J. Evans, T. Majeed, P. Shen, R. Cox, R. Link, and R. Huffman (1999), Atmospheric ultraviolet radiance integrated code (auric): Theory, software architecture, inputs, and selected results, *Journal of Quantitative Spectroscopy and Radiative Transfer*, *62*(6), 689–742.

Strickland, D., R. Meier, R. Walterscheid, J. Craven, A. Christensen, L. Paxton, D. Morrison, and G. Crowley (2004), Quiet-time seasonal behavior of the thermosphere seen in the far ultraviolet dayglow, *Journal of Geophysical Research: Space Physics*, *109*(A1).

Strickland, D. J., R. E. Daniell, and J. D. Craven (2001), Negative ionospheric storm coincident with de 1-observed thermospheric disturbance on october 14, 1981, *Journal of Geophysical Research: Space Physics*, *106*(A10), 21,049–21,062, doi: 10.1029/2000JA000209.

Toffoletto, F., S. Sazykin, R. Spiro, and R. Wolf (2003), Inner magnetospheric modeling with the rice convection model, *Space Science Reviews*, *107*(1), 175–196.

Tóth, G., et al. (2005), Space weather modeling framework: A new tool for the space science community, *Journal of Geophysical Research: Space Physics*, *110*(A12), 1–21, doi:10.1029/2005JA011126.

Tóth, G., et al. (2012), Adaptive numerical algorithms in space weather modeling, *Journal of Computational Physics*, *231*(3), 870–903.

Tsyganenko, N. A., and M. I. Sitnov (2005), Modeling the dynamics of the inner magnetosphere during strong geomagnetic storms, *Journal of Geophysical Research: Space Physics*, *110*(A3), 1–16, doi:10.1029/2004JA010798.

Valladares, C. E., S. Basu, J. Buchau, and E. Friis-Christensen (1994), Experimental evidence for the formation and entry of patches into the polar cap, *Radio Science*, *29*(1), 167–194, doi:10.1029/93RS01579.

Valladares, C. E., D. T. Decker, R. Sheehan, and D. N. Anderson (1996), Modeling the formation of polar cap patches using large plasma flows, *Radio Science*, *31*(3), 573–593, doi:10.1029/96RS00481.

Vasyliunas, V. (1970), Mathematical Models of Magnetospheric Convection and its Coupling to the Ionosphere, in *Particles and Fields in the Magnetosphere*, vol. 17, pp. 60–71.

Walker, I. K., J. Moen, L. Kersley, and D. A. Lorentzen (1999), On the possible role of cusp/cleft precipitation in the formation of polar-cap patches, *Annales Geophysicae*, *17*(10), 1298–1305, doi:10.1007/s00585-999-1298-4.

Wang, H., and H. Lühr (2011), The efficiency of mechanisms driving Subauroral Polarization Streams (SAPS), *Annales Geophysicae*, *29*(7), 1277–1286, doi: 10.5194/angeo-29-1277-2011.

Wang, H., A. J. Ridley, H. Lühr, M. W. Liemohn, and S. Y. Ma (2008), Statistical study of the subauroral polarization stream: Its dependence on the cross-polar cap potential and subauroral conductance, *Journal of Geophysical Research: Space Physics*, *113*(12), 1–11, doi:10.1029/2008JA013529.

Wang, Z., S. Zou, T. Coppeans, J. Ren, A. Ridley, and T. Gombosi (2019a), Segmentation of SED by Boundary Flows Associated With Westward Drifting Partial Ring current, *Geophysical Research Letters*, *46*(14), 7920–7928, doi: 10.1029/2019GL084041.

Wang, Z., S. Zou, S. G. Shepherd, J. Liang, J. W. Gjerloev, J. M. Ruohoniemi, B. Kunduri, and J. R. Wygant (2019b), Multi-instrument observations of mesoscale enhancement of subauroral polarization stream associated with an injection, *Journal of Geophysical Research: Space Physics*, *124*(3), 1770–1784, doi:https://doi.org/10.1029/2019JA026535.

Wang, Z., S. Zou, L. Liu, J. Ren, and E. Aa (2021), Hemispheric asymmetries in the mid-latitude ionosphere during the september 7-8 2017 storm: Multi-instrument observations, *Journal of Geophysical Research: Space Physics*, p. e2020JA028829, doi:https://doi.org/10.1029/2020JA028829.

Wanliss, J. A., and K. M. Showalter (2006), High-resolution global storm index: Dst versus sym-h, *Journal of Geophysical Research: Space Physics*, *111*(A2), doi:https://doi.org/10.1029/2005JA011034.

Wei, D., Y. Yu, and F. He (2019), The magnetospheric driving source of double-peak subauroral ion drifts: Double ring current pressure peaks, *Geophysical Research Letters*, *46*(13), 7079–7087, doi:https://doi.org/10.1029/2019GL083186.

Weimer, D. R. (2005), Improved ionospheric electrodynamic models and application to calculating Joule heating rates, *Journal of Geophysical Research: Space Physics*, *110*(A5), 1–21, doi:10.1029/2004JA010884.

Wernik, A., J. Secan, and E. Fremouw (2003), Ionospheric irregularities and scintillation, *Advances in Space Research*, *31*(4), 971–981.

Wolf, R. A., R. W. Spiro, S. Sazykin, and F. R. Toffoletto (2007), How the Earth's inner magnetosphere works: An evolving picture, *Journal of Atmospheric and Solar-Terrestrial Physics*, *69*(3), 288–302, doi:10.1016/j.jastp.2006.07.026.

Woodman, R. F., J. L. Chau, and R. R. Ilma (2006), Comparison of ionosonde and incoherent scatter drift measurements at the magnetic equator, *Geophysical Research Letters*, *33*(1), 1–4, doi:10.1029/2005GL023692.

Woods, T. N., F. G. Eparvier, S. M. Bailey, P. C. Chamberlin, J. Lean, G. J. Rottman, S. C. Solomon, W. K. Tobiska, and D. L. Woodraska (2005), Solar EUV Experiment (SEE): Mission overview and first results, *Journal of Geophysical Research: Space Physics*, *110*(A1), 1–24, doi:10.1029/2004JA010765.

Wygant, J. R., et al. (2014), The Electric Field and Waves Instruments on the Radiation Belt Storm Probes mission, pp. 183–220, doi:10.1007/978-1-4899-7433-4-6.

Xia, Z., L. Chen, L. Zheng, and A. A. Chan (2017), Eigenmode analysis of compressional poloidal modes in a self-consistent magnetic field, *Journal of Geophysical Research: Space Physics*, *122*(10), 10,369–10,381, doi:10.1002/2017JA024376.

Xiong, C., H. Lühr, and Y. Yamazaki (2019), An Opposite Response of the Low-Latitude Ionosphere at Asian and American Sectors During Storm Recovery Phases:

Drivers From Below or Above, *Journal of Geophysical Research: Space Physics*, *124*(7), 6266–6280, doi:10.1029/2019JA026917.

Xiong, Y., L. Chen, L. Xie, S. Fu, Z. Xia, and Z. Pu (2017), Relativistic electron's butterfly pitch angle distribution modulated by localized background magnetic field perturbation driven by hot ring current ions, *Geophysical Research Letters*, *44*(10), 4393–4400, doi:10.1002/2017GL072558.

Yao, Y., C. Zhai, J. Kong, C. Zhao, Y. Luo, and L. Liu (2020), An improved constrained simultaneous iterative reconstruction technique for ionospheric tomography, *GPS Solutions*, *24*, 1–19.

Yokoyama, N., and Y. Kamide (1997), Statistical nature of geomagnetic storms, *Journal of Geophysical Research: Space Physics*, *102*(A7), 14,215–14,222, doi: https://doi.org/10.1029/97JA00903.

Yu, Y., V. Jordanova, S. Zou, R. Heelis, M. Ruohoniemi, and J. Wygant (2015), Modeling subauroral polarization streams during the 17 March 2013 storm, *Journal of Geophysical Research A: Space Physics*, *120*(3), 1738–1750, doi:10.1002/2014JA020371.

Yue, X., et al. (2016), Long-lasting negative ionospheric storm effects in low and middle latitudes during the recovery phase of the 17 March 2013 geomagnetic storm, *Journal of Geophysical Research: Space Physics*, *121*(9), 9234–9249, doi:10.1002/2016JA022984.

Zhang, Q. H., et al. (2016), Polar cap patch transportation beyond the classic scenario, *Journal of Geophysical Research : Space Physics*, *121*(9), 9063–9074.

Zhang, S.-R., J. C. Foster, A. J. Coster, and P. J. Erickson (2011), East-west coast differences in total electron content over the continental us, *Geophysical Research Letters*, *38*(19), doi:10.1029/2011GL049116.

Zhang, S.-R., P. J. Erickson, A. J. Coster, W. Rideout, J. Vierinen, O. Jonah, and L. P. Goncharenko (2019), Subauroral and polar traveling ionospheric disturbances during the 7-9 september 2017 storms, *Space Weather*, *17*(12), 1748–1764, doi:10.1029/2019SW002325.

Zhang, Y., L. J. Paxton, D. Morrison, B. Wolven, H. Kil, C. I. Meng, S. B. Mende, and T. J. Immel (2004), O/N2 changes during 1-4 October 2002 storms: IMAGE SI-13 and TIMED/GUVI observations, *Journal of Geophysical Research: Space Physics*, *109*(A10), doi:10.1029/2004JA010441.

Zhao, H., et al. (2015), The evolution of ring current ion energy density and energy content during geomagnetic storms based on Van Allen Probes measurements, *Journal of Geophysical Research A: Space Physics*, *120*(9), 7493–7511, doi:10.1002/2015JA021533.

Zhou, Y.-L., H. Luhr, C. Xiong, and R. F. Pfaff (2016), Ionospheric storm effects and equatorial plasma irregularities during the 17-18 march 2015 event, *Journal of Geophysical Research: Space Physics*, *121*(9), 9146–9163, doi:10.1002/2016JA023122.

Zou, S., and A. J. Ridley (2016), Modeling of the Evolution of Storm-Enhanced Density Plume during the 24 to 25 October 2011 Geomagnetic Storm, in *Magnetosphere-Ionosphere Coupling in the Solar System*, pp. 205–213, doi:10.1002/9781119066880.ch16.

Zou, S., L. R. Lyons, M. J. Nicolls, C. J. Heinselman, and S. B. Mende (2009a), Nightside ionospheric electrodynamics associated with substorms: PFISR and THEMIS ASI observations, *Journal of Geophysical Research: Space Physics*, *114*, 1–24, doi:10.1029/2009JA014259.

Zou, S., L. R. Lyons, C. P. Wang, A. Boudouridis, J. M. Ruohoniemi, P. C. Anderson, P. L. Dyson, and J. C. Devlin (2009b), On the coupling between the Harang reversal evolution and substorm dynamics: A synthesis of SuperDARN, DMSP, and IMAGE observations, *Journal of Geophysical Research: Space Physics*, *114*(1), doi:10.1029/2008JA013449.

Zou, S., L. R. Lyons, and Y. Nishimura (2012), Mutual evolution of aurora and ionospheric electrodynamic features near the Harang reversal during substorms, in *Auroral Phenomenology and Magnetospheric Processes: Earth And Other Planets*, vol. 197, pp. 159–169, doi:10.1029/2011GM001163.

Zou, S., A. J. Ridley, M. B. Moldwin, M. J. Nicolls, A. J. Coster, E. G. Thomas, and J. M. Ruohoniemi (2013), Multi-instrument observations of SED during 24-25 October 2011 storm: Implications for SED formation processes, *Journal of Geophysical Research: Space Physics*, *118*(12), 7798–7809, doi:10.1002/2013JA018860.

Zou, S., M. B. Moldwin, A. J. Ridley, M. J. Nicolls, A. J. Coster, E. G. Thomas, and J. M. Ruohoniemi (2014), On the generation/decay of the storm-enhanced density plumes: Role of the convection flow and field-aligned ion flow, *Journal of Geophysical Research : Space Physics*, *119*(September 2005), 8543–8559, doi:10.1002/2014JA019887.